Organ-on-Chip Platform with Transient Membrane for Vascularisation of Brain Organoids

MSc. Biomedical Engineering

Friso Kahler

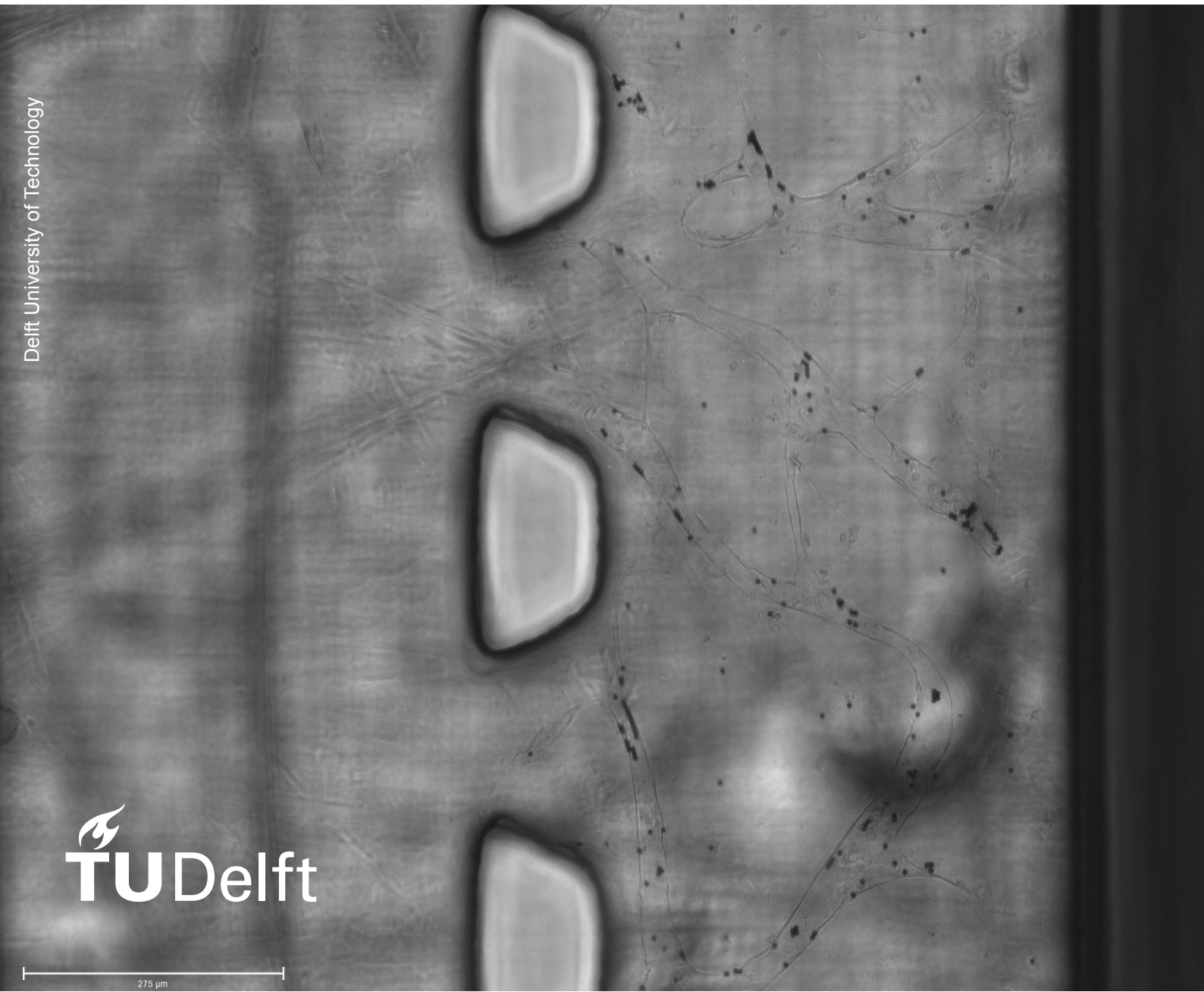

Delft University of Technology

TU Delft

Organ-on-Chip Platform with Transient Membrane for Vascularisation of Brain Organoids

by

Friso Kahler

in partial fulfilment of the requirements for the degree of

Master of Science
in Biomedical Engineering
Specialisation: Medical Devices and Biodegradable Technologies at Delft University of Technology,

to be defended publicly on Tuesday, February 13th, 2024 at 03:30 PM.

Supervisor:	Dr. Clementine Boutry
Thesis committee:	Prof. Dr. Lina M. Sarro
	Dr. Achilleas Savva
	Dr. Angelo Accardo

TU Delft

Acknowledgement

The report you are about the read reflects on the one-year journey that has been my master graduation thesis. This journey has been a transformative experience, shaping me into a budding Biomedical Engineer. From its inception to the final moments of meticulous editing, this endeavor has tested and strengthened me in multiple ways, blending moments of success, failure, and joy.

Foremost, I extend my deepest gratitude to Dr. Clementine Boutry, whose unwavering guidance allowed me to navigate this project with autonomy yet always offered invaluable direction. I also express sincere appreciation to my thesis committee members — Prof. Dr. Sarro, Dr. Savva, Dr. Accardo — for their invested time and insights.

Central to the project's success was its interdisciplinary nature, facilitated by collaborations with Dr. Femke de Vrij, Dr. Valeria Orlova, Mark van der Kroeg, and Dr. Marc Vila Cuenca. Their input and camaraderie enriched our work across three institutions.

Equally indispensable were the contributions of Prof. Ekkes Brück, Prof. Kristina Djanashvili, and Prof. Leon Abelmann, whose provision of lab equipment and wisdom were instrumental. The daily support from the EKL-team and Filip Simjanoski, ensured a conducive working environment.

Gratitude extends to the Organ-on-Chip group, led by Dr. Massimo Mastrangeli, and the Biodegradable Technologies group, whose feedback and collaboration were highly appreciate. Special mention goes to Elena for joining me on this project, to Feyza for helping me set up the simulation model as part of this thesis, and to Tim for spending countless hours with me in the lab.

This report does not only conclude my master studies but offers a moment to reflect on the last two years. And what stands out the most is the amazing group of friends I have found here. My dear Jumbo people, I am so cheerful that we have met. Thank you all for making these last two years so immaculate and enjoyable, that a part of me wishes that we all would never graduate. I am grateful that I found roots not in one, but in two cities in a used-to-be-strange country. The community I built in Den Haag gave me nothing but support and strength, which was pivotal to keep on writing this journey.

I am profoundly thankful to my parents for the opportunity, trust, and motivation to study abroad. Lastly, to Paulina, your everlasting support has been my anchor throughout this journey — I could not have done it without you.

Friso Kahler
Delft, February 2024

Abstract

Organ-on-Chip (OoC) is a technology that aims to increase the efficiency of drug development processes and organ models by engineering well-defined cell culture environments. Physiological relevant mechanical, chemical, or electrical cues provide in vivo-like microenvironments for realistic cell maturation. Biodegradable technologies have gained attention for the development of novel OoCs by integrating transient features to the culture platforms imitating the ever-changing environment inside the human body. Current efforts to replicate durable brain tissue models from organoids are limited by the lack of sufficient vascularisation introducing cell necrosis inside the 3D cell culture.
This report presents the design and fabrication of a 3D-printed OoC-platform that combines two independent cell protocols for a Vessel-on-Chip and a cortical brain organoid. The microfluidic chip is embedded with a biodegradable membrane, that separates the two cell cultures for a strictly defined time period. The membrane, composed of bayberry wax, lanolin, and carbonyl iron particles, enables the controlled opening via alternating magnetic field exposure. The thermal behaviour of the membrane is analysed with DSC and the magnetic particles with a SQUID magnetometer. Inductive heating experiments determine the optimal composite composition and exposure profile to facilitate membrane opening and subsequent communication between neural and vascular cells. The integrated membrane proved to be successful during the injection and evacuation phase. This positive result paves the way for co-culturing two inherently different cell protocols on a single chip. This master project lays the foundation for collaborative efforts towards vascularised brain organoids-on-chip and showcases the potential of additive manufacturing and biodegradable materials in OoC technology.

Contents

List of Figures

List of Tables

1 Introduction

Organ-on-Chip (OoC) is a technology that aims to increase the efficiency of drug development processes and disease modeling. OoCs are cell culture platforms that mimic the mechanical, chemical and/or electrical microenvironments of an organ promoting in vivo-like cell maturation in a strictly engineered space. Through on-chip culturing of specific cells in a three-dimensional configuration, OoCs yield a high relevance for human physiology while maintaining reproducibility due to the microfabrication process. Combining these features, they extend common in vitro cell culture settings and in vivo animal models for the purpose of drug development and disease modeling [1, 2, 3].

One of the most complex organs in the human body is the brain. Studying disease pathologies, brain evolution, and neurodevelopment is the focus of many research groups. Realistic in vitro models exist in the form of organoids. These are 3D cell culture models closely recreating the architecture, cell composition, and functionality of the target organ [4]. However, a lack of vascularisation limits the significance of organoid models. With the absence of an intact perfusion network, insufficient mass transfer of oxygen and nutrients causes the build-up of a necrotic core inside the organoid. To illustrate, the survival rate of cells drops drastically when the next vessel is more than 200 µm away [5].

There is a high need for the development of new OoCs that allow co-culturing of organoids with vascular networks. Adding vessels to the organoid allows for the penetration of nutrients and oxygen to the core of the cell cluster. Thereby, this approach extends the longevity and also increases the tissue complexity. However, the main challenge lies within the inherently different handling of vascular cells in distinction to brain organoids. The vascular network in the human body is permanently subjected to the pulsating blood flow. Each heartbeat carries the blood stream further through the vessels. This generates a shear stress on the cell wall that is an integral part for inducing cell growth. In contrast, brain organoids are fragile constructs that are cultured in a steady and static environment. A realistic OoC-model would need to satisfy both: shear stress for the vascular network, and stability for the fragile structure of brain cells.

Biodegradable technologies have gained attention for the development of novel OoCs due their ability to provide a changing profile of properties and functionality during the culture period. Biodegradability adds a new dimension to cell culture systems like OoCs: transient behaviour of the environment. In the human body, no state is constant. With the integration of biodegradable materials, OoC-platforms themselves can provide changing environments to satisfy cells' varying requirements on their environment during their maturation progress. This approach can be exploited to create a timely separation of the two cell cultures to allow the cross talk only when the distinct features of the protocols are sufficiently matured.

Acknowledging the different efforts to mimic cell environments, I use the strength and weaknesses of previous efforts on OoC technology, vascularisation of brain organoids and biodegradable materials to

answer the following research question:

> *How to develop an Organ-on-Chip platform for multi-cell culture with transient separation of a brain organoid and vascular network?*

The deduced objective of this thesis is to develop an Organ-on-Chip platform that is suitable to provide two different culture environments at the same time to effectively co-culture a vascular network with brain organoids. The microfluidic chip will be embedded with a biodegradable membrane, that separates the two cell cultures for a precisely defined time.

This report acts as documentation of the experiments conducted towards answering that research question. In the following chapter 2, the state of the art of the Organ-on-Chip technology in terms of material choices and fabrication is presented. Recent advances of the vascularisation of brain organoids are presented leading to the introduction of two specific cell protocols for a Vessel-on-Chip and a brain organoid model, respectively. Wax-based composites are discussed as selected class of biodegradable materials to build the embedded membrane. In Chap. 3, the conducted experiments and selected materials are presented followed by the demonstration of the results in Chap. 4. The results are discussed with reference to other works and future recommendations in Chap. 5 before the report is concluded in Chap. 6.

2

State of the Art

2.1. Organ-on-Chip: Materials and Fabrication

Organ-on-Chip (OoC) technology is a specific cell culturing approach that is employed to achieve more realistic organ models for drug research and disease modelling. OoCs focus on eliminating the need for animal models while providing high-throughput devices for research with live cells. It encompasses microfluidic platforms that mimic the environment of one or more human organs [6]. The geometrical, mechanical, and physicochemical properties are imitated which creates an engineered functional unit of the target organ [2]. The OoC technology incorporates the expertise from cell biology, medicine and engineering which makes it a highly interdisciplinary field. Through on-chip culturing of specific cells in a three-dimensional configuration, OoCs yield a high relevance for human physiology while maintaining reproducibility due to the microfabrication process. Hence, they extend common in vitro cell culture settings and in vivo animal models for the purpose of drug development and disease modeling [3]. In research, OoCs exist for several organs. Amongst the organs replicated are the liver [7], lung [8] and heart [9], as well as intestines, kidney, brain, and multi-organ chips [10].

The OoC technology is a promising lead towards animal free research and accessible organ models are set to expedite the drug developing process. The dimensional scale in the micron range demands high accuracy during the fabrication process. This poses strict requirements to the materials and fabrication methods employed. This section gives an overview over the state of the art for the relevant advancements to draw informed conclusions on the material and fabrication methods for this master project.

2.1.1. Materials for Organ-on-Chip

In order to select a suitable material for OoC-platforms, the required properties of the materials are considered. These can be deducted from the intended use of the microfluidic platforms, leading to three main properties [11]. Firstly, the material must be biocompatible in order to host cells and promote their growth. In the research of drugs and organ models, this is essential to generate realistic models. Secondly, the materials for OoCs must be transparent. The predominant analytic method for cell cultures is optical microscopy. This demands for the visible spectrum for light microscopy, but also ultraviolet (UV) light must transverse the material to enable advanced imaging such as immunofluoresence. Thirdly, the material must be processable in a cost efficient and rapid manner. One advantage of OoC is the efficient fabrication of the chips generating high-throughput culture devices. The material therefore must support the requirements of these methods to be eligible for OoC. These three main requirements define the decision framework for the available materials and are depicted in Fig. 2.1.

In previous studies, a wide range of material classes has been considered for the fabrication of OoC devices. Amongst the most common choices are polymers (elastomers and thermoplastics), inorganic materials, and natural materials. Beyond the three main requirements mentioned above, the mechan-

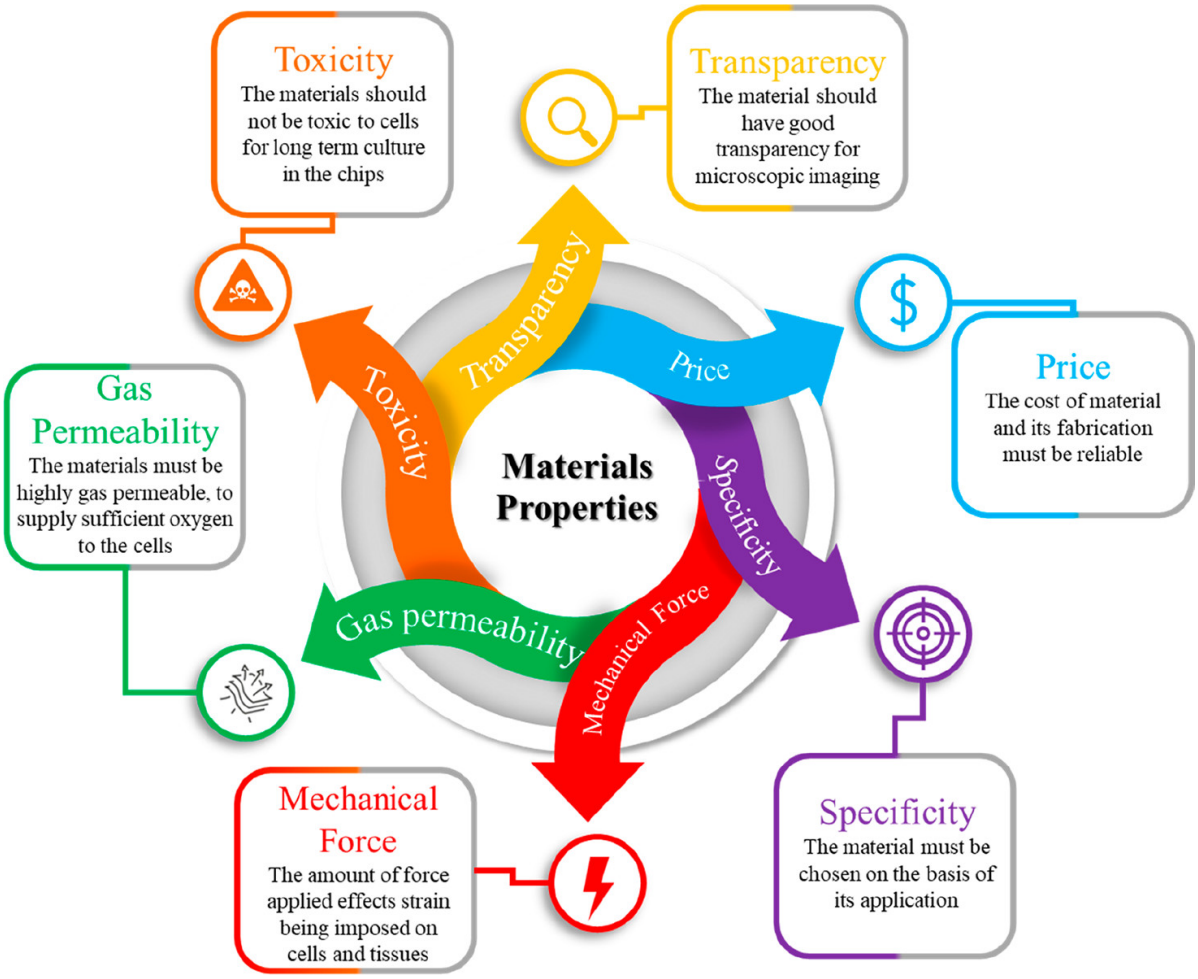

Figure 2.1: Key material properties and required characteristics for OoC device fabrication. Reproduced from [12].

ical performance, chemical behaviour in contact with cells and/or media, gas permeability and the smallest possible feature size are parameters that influence the device performance [12]. Therefore, the material selection process allows to tune the functionality of the device by actively focusing on relevant material parameters.

Elastomers

Since the origin of the technology, the majority of OoC-devices are fabricated with Polydimethylsiloxane (PDMS) [13]. PDMS is an elastomeric polymer with Si-O bonds. The main advantages of this polymer lay in the mechanical properties and the optical transparency. The elasticity of PDMS is close to native tissue properties and hence replicates realistic microenvironments on the chip. Next to the optical transparency, chips fabricated from PDMS exhibit a good gas permeability. This is beneficial for cells as they are passively supplied with oxygen even in closed microfluidic cavities. However, drawbacks set a limit to the application of PDMS. Untreated, the hydrophobic surface of PDMS tends to absorb hydrophobic molecules. This aggravates the handling of biological fluids and can lead to false interpretation of drug efficiency due to the loss of test compounds from the media to the substrate [14].

Alternative elastomers for OoC-fabrication are poly-(lactic-co-glycolic acid) (PLGA) and Poly (octamethylene maleate (anhydride) citrate) (POMaC) [15]. In addition to depicting similar material properties as PDMS, both PLGA and POMaC are biodegradable. Hence, they advance the possibilities for device design. PLGA has successfully been used as chip substrate and cell scaffold on a Lung-on-Chip device by [16]. POMaC is used as a substrate material and favourable due to its double crosslinking mechanism, which allows to mimic the mechanical properties of a wide variety of tissues [17].

Thermoplastics

Thermoplastics are polymers that can be reversibly melted and solidified. Advantages for microfluidic devices are their excellent transparency, low-cost and high-throughput mass fabrication, and vis-a-vis PDMS, high resistance towards leaching and absorption of small molecules [13]. Multiple thermoplastics have been utilised to fabricate OoCs. For example, Poly(methyl methacrylate) (PMMA) is suitable as a replacement for PDMS [18]. The main distinction is the ability to be recycled due to its thermoplasticity. The key properties were found to be stable after several cycles of reusing the material [19]. Other thermoplastics employed for OoC are Cyclic olefin polymers and copolymers (COPs/COCs), Polysterene (PS), and Polycarbonate (PC) [20, 21, 22]. Based on these studies, drawbacks of thermoplastics for the fabrication of OoCs are their high rigidity, limitations in device design complexity, and low gas permeability [6].

Inorganic materials

Next to polymeric materials, inorganic materials can be advantageous in the design and fabrication of OoCs. To mention the most relevant examples, paper, silicon, and glass are options for microfluidic devices [13]. Paper-based microfluidics combine low-cost production with a vast material availability easing the fabrication of inexpensive OoCs [23]. Glass features high optical transparency and biocompatibility [12]. Compared to PDMS, glass substrates exhibit a lower drug absorbance which is beneficial to the assessment of drug models [24]. In [25], an OoC fully made of glass is reported. However, the non-permeability of glass for oxygen inspired a variety of multi-material platforms. A commercialised example is the OrganoPlate from MIMETAS which features a glass substrate, polymer structures and cell-laden hydrogel [26]. Silicon-based devices show similar properties as glass-based OoCs, yet their main drawback is the optical intransparency [12]. Therefore, elements of the device must be fabricated from a different material for the imaging of the cell cultures. An advantage of using silicon as substrate is the integration of sensing and stimulation units on the chip. The electrical properties of the semiconductor can be exploited to create smart cell culture platforms. To illustrate, a smart temperature sensor based on CMOS-technology has been integrated on the same silicon wafer as a custom OoC-platform [27], which allows real-time monitoring of the experimental conditions of the cell culture.

3D-printing resins

Another class of materials this report sheds light on are 3D-printing resins. In most cases, resins consist of monomers of a specific molecule but factually are hybrid materials since functional chemicals must be added [28]. These function as stabilisers and most importantly, as photo initiators that absorb UV light in order to trigger the cross linking of the liquid resin. Meeting the requirements presented in Fig. 2.1 is equally important for resins as for PDMS or PS, but certain material and fabrication properties aggravate the fulfilment. The monomers in the resin, most often acrylate or methacrylate, exhibit a high toxicity [29]. Therefore, the (post-)processing of resins must be closely monitored to eliminate all uncured resin. Another hurdle is the transparency of resin-based devices. On the one hand, the resin must absorb the UV light in the range of 380-410 nm to initiate the cross linking during the fabrication. The cured device, however, must be transparent in this range for imaging with light and fluorescence microscopy [28]. On the other hand, the surface roughness which influences the scattering of light, is highly dependent on the spatial curing resolution as well as the roughness of the print head. Dedicated measures must be implemented into the workflow to produce highly transparent OoCs [30]. Nevertheless, the perspective of overcoming these issues bears several advantages which make resins a promising candidate for OoCs [6]. They feature low fabrication costs and enable quick processing with additive manufacturing (AM). Additionally, AM allows for a high design freedom as the processing is independent of global device structures but proceeds layer by layer. In [28], the authors compared the mechanical properties of three different resins to PDMS and PS, showing an elastic modulus between the two standard OoC materials. Furthermore, the absorbance of hydrophobic molecules was in the order of three to four magnitudes lower in devices from resins compared to PDMS (see Fig. 2.2) [28].

Bringing the findings of the different classes of materials for OoC devices together, demonstrates a high variability of available options. Exceeding the sheer fulfilment of the three main requirements elaborated above - namely, biocompatibility, optical transparency and cost-efficiency -, distinct material properties can advance the functionality of the chip. To explain, the right choice of materials is not only circumventing limitations but provides the user with the ability to create higher specificity for the

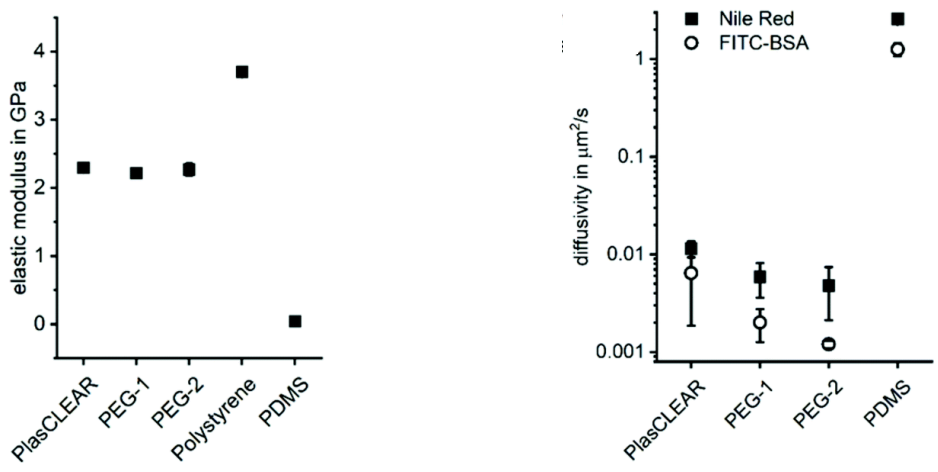

Figure 2.2: Comparison of three different 3D-printing resins for OoC fabrication to PS and PDMS. Characterisation for their elastic modulus by nanoindentation (left) and the diffusivity of hydrophobic molecules into the substrate (right). Reproduced from [28].

intended application, i. e. more realistic microenvironments for cell cultures. However, the material selection stands in mutual dependence of the selected fabrication method. Therefore, the following section focuses on available fabrication methods for OoC devices.

2.1.2. Fabrication Methods for Organ-on-Chip

Despite the recency of the OoC technology, a multitude of fabrication methods have been established. In general, OoCs are fabricated using microfabrication to realise typical feature sizes in the micron range. In microfabrication, material is either added or removed and substrates are patterned to transfer the desired geometry or to modify the surface. In this subsection, the most common techniques are briefly described. In the following, 3D-printing is compared to conventional means of fabrication to highlight it as preferred and thereby selected fabrication process for the OoC-platform designed in this report.

Soft lithography

An often-employed technique is soft lithography. It has its origin in the established cleanroom method of photolithography and subsequently follows a similar approach. While photolithography can reach smaller feature sizes and higher accuracy, soft lithography is applicable to a wider range of materials [31]. Especially the integration of soft materials, like elastomers, makes soft lithography suitable for OoCs. The term soft lithography summarises several techniques to transfer a pattern to mechanically soft materials. The general procedure includes four steps: design of the pattern, fabrication of the mask and the master, fabrication of the PDMS stamp and fabrication of structures by printing, molding, and embossing [31].

A typical workflow of soft lithography is presented in Fig. 2.3 [32]. A photoresist is spin coated on the surface of a wafer and subsequently patterned through a photo mask with UV light. In case a negative photo resist is used as in Fig. 2.3, only the illuminated areas of the photoresist will cross link and become robust towards the developer (step **C)** in Fig. 2.3). The patterned photoresist on the wafer after development is the master for the device fabrication. Pouring PDMS over the structures yields the microfluidic device after bonding the microfluidic structure to a substrate from glass or PDMS. In case of replica molding, the pattern in the PDMS is transferred to a replica of the original master. This

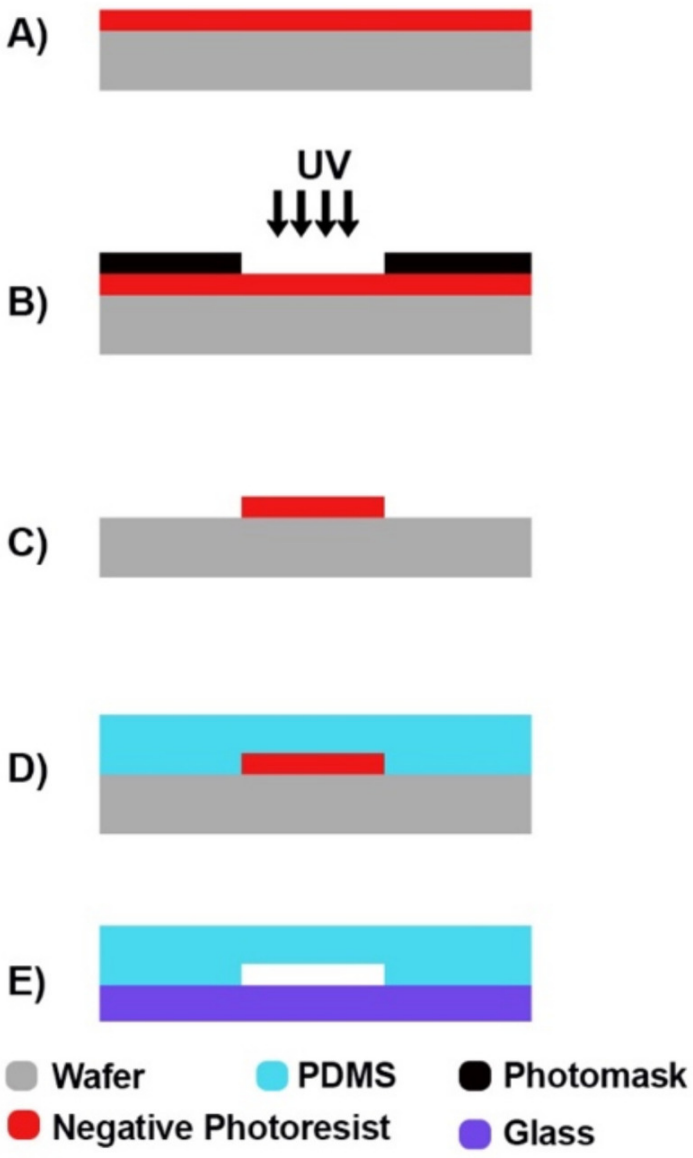

Figure 2.3: Overview of the soft lithography process for OoC fabrication. A master is created with patterning a photoresist on a wafer substrate. The PDMS is poured over the structure to create the bulk of the OoC device. After bonding the PDMS structure to a substrate, the device is readily usable. Reproduced from [32].

can be achieved by solidifying a liquid pre-polymer against the PDMS [33]. Replica molding increases the throughput since many replicas can be built in one processing step.

Examples of OoCs fabricated with soft lithography are available from different research groups. For example, [34] illustrates a Brain-on-Chip model for the study of neurodevelopment and neurotoxicity. The device consists of three layers to mimic the blood brain barrier (BBB) of neuronal tissue. Another application is a gut-liver-system which is reported in [35]. Two layers of microfluidic channels are fabricated, as depicted in Fig. 2.3, to build chambers for two different cell types. The compartments are separated by a porous membrane to enable crosstalk between the different cell types.

While the fabrication steps requiring cleanroom facilities (producing master) can be avoided by employing replica molding, the photolithography step to create the master mold remains an intensive part of the device fabrication. Efforts have been made to fully eliminate this step. A promising possibility is the use of 3D-printed molds. To illustrate, [36] established a simple post-processing protocol for 3D-printed molds. This improves the compatibility of resins with PDMS and subsequently eases the

whole fabrication process.

Injection molding

Injection molding is a technique applicable for thermoplastic polymers. It requires the fabrication of two-parted molds containing the negative microstructures of the OoC-platform. The molds are pressed together to form a sealed cavity. The melted material is injected into the cavity and allowed to cool down before the device is released from the mold [37]. [38] presents a protocol for the fabrication of microfluidic devices from COP. The process is solvent-free and compatible with mass fabrication. The researchers used patterned metal blocks as master molds for the injection of the melted COP. The injection molding process is depicted in Fig. 2.4. Injection molding is suitable for large scale fabrication but requires precise pressure and temperature control as well as high machine costs to satisfy accuracy requirements [32]. Additionally, the design complexity is limited by the set-up of the process which impedes undercuts.

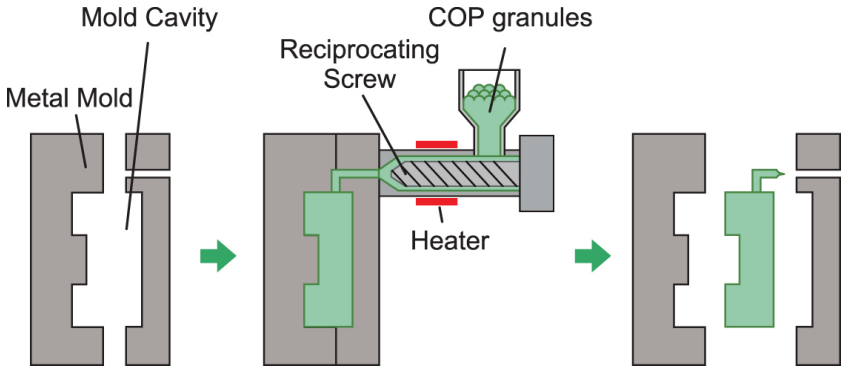

Figure 2.4: Overview of the injection molding process for OoC fabrication. A master is created from metal blocks. The molds are pressed together to form a cavity which is filled by the melted material. Reproduced from [38].

3D-printing

3D-printing, or more broadly additive manufacturing (AM), recently advanced into the field of OoC. AM fabricates three-dimensional physical objects from a computer aided design (CAD) model in a single processing step [30]. In contrast to conventional manufacturing or microfabrication, AM methods add material only at exact positions intended by the CAD model. This reduces material loss and accelerates the fabrication process. The printing of the object proceeds layer-by-layer, i. e., material is added in increments from the bottom to the top of the part. For this, the CAD object is converted to the STL file format which sections the surfaces into triangulated shapes. The file is then digitally sliced in 2D layers with a layer thickness defined by the user. The individual layers are sequentially fabricated by the machine [30]. As a consequence, the processing is independent of the overall part geometry, since the process virtually becomes two-dimensional. This enables excellent design freedom and complex 3D structures.

Elaborating the deployment of 3D-printing for OoC requires to distinguish between the fields of application. 3D-printing is implemented in two ways: fabrication of the whole platform, and bioprinting [37]. Bioprinting processes biomaterials, such as hydrogels. Optionally, living cells can be laden in the ink. To illustrate, Homan et al. created a perfusable chip with bioprinting [39]. Here, fugitive ink is deposited in the shape of the aspired perfusion network onto the substrate and subsequently covered with engineered extracellular matrix (ECM). The removal of the fugitive ink at low temperatures leaves a hollow structure inside the ECM that accommodates cells in a three-dimensional structure.

Available AM techniques for the fabrication of whole OoCs are inkjet printing (i3DP), two-photon-polymerisation (2PP), fused deposition modelling (FDM) and digital light processing (DLP) as example of stereolithography (SLA) [30, 40]. The factors to consider for the process of choice are resolution, speed, material and build size [40]. In the following, the different techniques are discussed. The advantages and drawbacks are summarised in Tab. 2.1 at the end of this subsection.

Inkjet printing (i3DP) manufactures powdered or liquid phase materials on a substrate. A fixed volume of the material is ejected through a nozzle as a droplet according to the CAD model. Mechanical

pulses on the material reservoir in the nozzle trigger the formation and ejection of the droplets [41]. In recent machines, these pulses are generated thermally or with piezoelectric volume changes [30]. The technique combines a high accuracy with a fast building speed while reaching a high reproducibility. However, the necessity for support structures to build cavities and the lack of process- and biocompatible, transparent materials limit the application of i3DP for OoCs [40].

Two-photon-polymerisation (2PP) utilises a near-infrared laser to selectively crosslink photosensitive material. Compared to other curing techniques, the principle of two photon absorption (TPA) is applied. In TPA, the energy level of a molecule is elevated by the simultaneous absorption of two photons. The combined energy exceeds the polymerisation threshold of the photo initiator in the material at the focal point of the laser causing a photochemical reaction between the monomers and photo initiator. Therefore, a single pulse solidifies material in a well-defined unit volume (voxel) [30]. TPA is a non-linear mechanism. To illustrate, the absorbed energy decays exponentially with increasing distance from the focus point of the laser. This leads to highly localised crosslinking of the material enabling a high resolution in 2PP-parts. Additionally, the materials used are usually transparent to NIR-light, enabling the direct fabrication of 3D-structures compared to the layer-by-layer approach of other AM processes [42].

Fused deposition modelling (FDM) processes thermoplastic polymers. The raw material is supplied as filament and deposited through a heated nozzle. After deposition, the material solidifies almost immediately while cold welding to the previous layer [43]. FDM is particularly interesting for the fabrication of prototypes for OoCs. Due to the wide range of thermoplastics employed for these devices, the general accessibility to FDM printers holds potential for efficient proof of concept models. In [44], the development of a microfluidic device for preparation of nanoparticles and electrochemical sensing is reported using a consumer-grade FDM printer.

Stereolithography (SLA) is a laser-based manufacturing process similar to 2PP. A focused laser light source causes the polymerisation of a photosensitive polymer resin in a vat [45]. Conventionally, a single UV laser scans and traces a substrate to spatially polymerise the liquid resin. After curing the 2D cross section, the substrate is lowered such that the part is built bottom-up. In a different configuration, the object is fabricated hanging upside-down from the suspended print head. In this case, the light source is located beneath the resin reservoir which features a transparent, non-sticky bottom. To print one layer, the print head is suspended at the distance of the layer height. The trapped resin is exposed to the light source to cure in the desired areas [30].

Alternatively, to a single laser as light source in SLA printers, digital light processing (DLP) operates with a digital mirror device (DMD). This element consists of multiple controlled micromirrors. By rotation, they control the path of the laser beam and project an optical pattern on the resin corresponding to the areas to be cross linked. Hence, in DLP all points of one layer are printed simultaneously as opposed to the serial approach described for i3DP (drop-by-drop), 2PP (voxel-by-voxel), FDM (line-by-line) and SLA (dot-by-dot) [46]. Accordingly, the resolution of the parts in the layer plane depends on the pixel density (spacing) of the DMD which typically reaches 15-100 µm [47]. A typical set-up for DLP is schematically shown in Fig. 2.5.

DLP is an up-and-coming method to fabricate OoCs due to advancements in material science and increased printing resolution. To replace common techniques such as soft lithography, the parts must meet the same requirements. Especially the transparency is a challenge to overcome with DLP-printed parts. In order to fabricate transparent devices, the material must not absorb visible light. However, the polymerisation of the part is in fact initiated by the absorption of light. The absorbance of the resin A is given with

$$A = \ln \frac{I_0}{I} = \epsilon(\lambda) c L \tag{2.1}$$

where I_0 and I are the intensity of incident and transmitted light, respectively, ϵ is the molar extinction coefficient at wavelength λ, c is the concentration of the photo initiator in the resin and L is the penetration depth. The molar extinction coefficient measures how strongly the light of a distinct wavelength

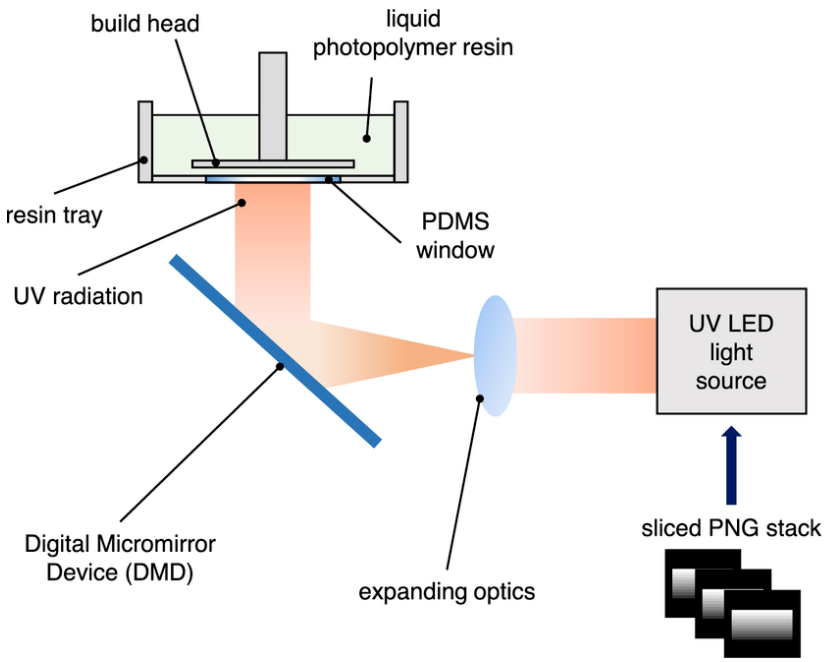

Figure 2.5: Schematic overview of the set-up for DLP. The specified 3D coordinates are transmitted as sliced information to the UV-source which illuminates the photosensitive polymer in the vat. The part is built from the slices layer-by-layer hanging upside-down from the build head. Reproduced from [48].

is absorbed by the material [49].

Therefore, the absorption spectrum ($\epsilon(\lambda)$) of the photo initiator and the operating wavelength of the machine must be carefully matched. This issue becomes evident with printing cavities such as microfluidic channels. When the ceiling of the channel is printed, liquid resin is trapped inside the channel. If the ceiling layer is easily penetrated by the light used to cure the resin, the resin in the channel will cross link leading to clogged channels. In addition, smooth surfaces and defect-free bulks are necessary to realise transparency since irregularities diffract the light. Efforts to increase the transparency of prints have been described in [28] and [49] as depicted in Fig. 2.6. Both groups used a glass surface for the vat bottom and attached a polished steel plate and glass plate to the build platform, respectively.

Advantages of 3D-printing for OoC-platforms

As shown above, the use of 3D-printing technologies holds great promises to advance the innovation of OoC-platforms. Compared to the conventional fabrication methods, soft lithography and injection molding, clear technique-specific advantages for 3D-printing arise. Yet, clearly defined needs for improvement remain. Due to the promising features DLP offers for the application in this master project, the benefits and drawbacks of using DLP are briefly commented on.

The widespread application of 3D-printing is mainly limited by two factors. The transparency of devices and the toxicity of the employed materials. As described in the previous section, the transparency is influenced by both the machine and the material properties. Early efforts show that with modulation of the printer truly transparent devices can be fabricated. The toxicity of the materials stems from the monomers contained in the resin which are often acrylates, methacrylates or urethanes [28]. Ideally, all monomers are cross linked in the printing process, but oxygen inhibition on the surface as well as trapped resin in microfluidic cavities increase the emergence of toxic monomers. In brief, oxygen binds free radicals that originate from the excited photo initiator. The free radicals are supposed to initiate the polymerisation of the monomers, which cannot happen if they are inhibited by oxygen [50]. Therefore, DLP-printed parts require an extensive post-processing including cleaning, UV-, and heat treatment [29].

While soft lithography employing PDMS or injection molding of COP or PMMA is free from toxicity constrains, DLP shows significant advantages in other process parameters. In general, DLP is an

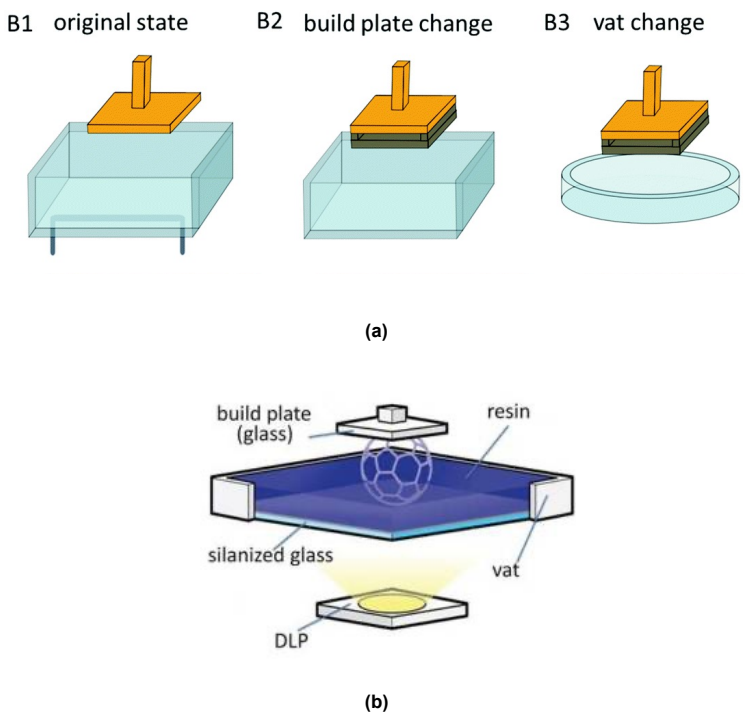

Figure 2.6: Alterations of the printing head and vat of DLP machines to improve transparency of devices. **(a)**: Modified DLP system with a highly polished and hardened steel build plate (B2) and glass petri dish as vat (B3). Reproduced from [28]. **(b)**: Modified DLP system with glass slide as build plate and salinised glass plat as vat bottom. Reproduced from [49].

easy-to-use approach due to the fact that it is a single step fabrication from CAD model to device. Additionally, the layer-by-layer manufacturing releases the design process from any geometrical constrains as arbitrary 3D structures are feasible [51]. This is especially beneficial for OoC fabrication since the microenvironment on the chip can be closely adapted to the requirements of different cell types. The single-step fabrication further allows for completely leakage-free channels, since the substrate, microstructures and ceiling are bonded during the build [52].

Table 2.1: Advantages, drawbacks and typical materials for 3D-printing technologies used for OoC devices [30, 40, 46].

Method	Energy source	Advantages	Drawbacks	Materials
i3DP	UV	• fast build time • multi-material printing • low cost	• requires post processing • support structures for cavities	• photocurable resins/polymers
2PP	Femtosecond laser	• very high resolution • small feature size	• slow build time	• photocurable resins/polymers
FDM	Thermal	• cheap materials • processing of thermoplastics	• slow build time • low accuracy • non-transparent materials	• thermoplastics (PC, ABS...) • elastomers
SLA	Laser/UV	• high resolution • good surface finish • low cost	• requires post-processing • removal of support structures	• photocurable resins/polymers
DLP	UV	• good resolution • fast build time	• limited building volume • requires post-processing	• photocurable resins/polymers

2.2. Vascularisation of Brain Organoids

In the previous section, some examples of OoC applications have been adduced to illustrate typical materials and fabrication methods. Here, recent advancement of vascularisation of brain organoids are presented. Organoids are 3D stem-cell derived cultures mimicking an intact compartment of a specific organ in terms of architecture, cell-composition, and functionality [4]. The environment of the culture is crucial to reach organ-like development and is highly dependent on the organ [53]. One way to create specific conditions for various types is to employ OoCs. There have been investigations to combine OoC and organoid technology [54, 55, 56, 57, 58]. While organoids offer more realistic in vitro organ models, the lack of vascularisation undermines the significance and comparability to live organs [58]. Without vascularisation, current organoids are reliant on the free diffusion length of oxygen and nutrients, which is around 200 µm in organoid tissue [59]. In addition, the amount of oxygen and nutrients that is provided by diffusion remains insufficient to back the organoid formation.

The form and function of the vasculature are important factors to consider [5]. The most important task of the vasculature is to deliver oxygen and nutrients to promote cell survival, but it can also be crucial for cell signalling and tissue specific maturation [60]. This becomes especially evident in the brain, where 15-20 % of the cardiac output is received by the vasculature in brain tissue due to its high metabolic action [61]. It is important to mention that the vascular network not only delivers oxygen and nutrients, but conversely evacuates carbon-dioxide and metabolic waste products. All these functions together benefit the realistic maturation of organoids and reduce the risk of cell necrosis in its centre.

There are three distinct approaches to vascularise organoids in the literature: biological self-organisation, implantation of organoids in a living host, and microfluidic engineering [5]. The focus hereafter is on

the third approach as it is the focus application of this thesis. In short, the first approach of biological self-organisation exploits the cellular and molecular signalling between different cell types. The cells are added together in close proximity leading to the spontaneous formation of the intended structures [62, 63]. As a second approach, in vitro cultured organoids are transplanted into animal hosts. The vessels of the host penetrate the organoid to form a vascular network in the organoid. Animal models used for this approach so far are mice [64] and chicken [62].

As the third approach, the fusion of OoC technology and cortical organoids for vascularisation is a relative recent approach to improve the quality of in vitro brain models. A decisive advantage of microfluidic platforms for the formation of vasculature is the incorporation of fluid forces to the vasculature [5]. The form of the vascular network greatly depends on the amount of shear stress the cells experience during the culture period. Vessels like arteries in the human body consist of several layers that are concentrically aligned to form tube-like structures transporting the blood. Layers of smooth muscle cells define the shape and strength of the tissue, however the innermost layer is constituted from endothelial cells (EC) [65]. The ECs feature mechanotransduction, i. e. mechanical stimuli influence their gene expression and behaviour [66]. Hemodynamic forces resulting from the blood flow through the vessels as well as cyclic strain from intravascular pressure cause the load [67]. Hence, the integration of these stimuli to the culture model are pivotal for realistic 3D network formation.

The state of the art to create vascular networks for organoid perfusion sees three different approaches when using OoC technology. Firstly, the successive generation of a vascular bed on-chip and implantation of a matured organoid on that structure. In [68], the authors engineered a 3D vascular network from human vascular ECs (HUVEC) on a PDMS microfluidic chip. The network spanned over the area of an open top chamber which allowed the introduction of a lung cancer spheroid used for co-culturing with the network in the same hydrogel. While the vascular bed can be connected to the outside to actively perfuse the system, the maturation process proceeds without introduction of shear stress. The lack of hemodynamic forces in this system leaves room for improvement accounting for the complexity of the vascular network. Additionally, spheroids show less complexity than organoids in terms of architectural and histological compliance with the real organ [69]. As a consequence, co-culturing in the same hydrogel is more likely to be successful.

The second approach is to place a matured organoid in an avascular hydrogel which is then penetrated by progressing sprouts of a vascular network. Salmon et al. 3D-printed a OoC co-culturing platform for a vascular network and an organoid [58]. The protocol foresees to seed the different cell cultures with an exact time separation to reach fusion at the optimal maturation point of both cell cultures. The chip is SLA-printed from the material Dental SG. The design features an open well chamber for organoid seeding which is flanked by microfluidic channels that host the microvascular network. The cell compartments are almost completely separated by a wall that leaves a 50 µm gap on the channel bottom for diffusion and cell spreading. The design of the chip and intended progress of vascularisation is presented in Fig. 2.7.

The chip was confirmed to be biocompatible with both cell cultures. The vascular differentiation and organoid culturing were initiated off chip. The size of the organoid as well as the sprout length was not influenced by the co-culture. While vessel sprouts reached the organoid chamber repeatably, the core of the organoids were penetrated less frequently. Whereas no alternative explanation could be validated, the confined spatial access of vessels to the organoid and lacking on-chip shear stress for the vascular network could be reasons for this result.

A third method to vascularise organoids on-chip is to spawn artificial network structures. For this, the organoid is encapsulated together with a sacrificial scaffold in a hydrogel. Upon evacuation of the sacrificial element, the resulting cavities can either be used to perfuse media or to seed ECs in the luminal structures. Simple approaches to create the voids are inserting needles or strings prior to the gelation of the hydrogel. A more sophisticated approach is bioprinting of the 3D network with fugitive inks. Compared to the generation of vascular networks in microfluidic channels as described in the two methods above, the sprouting and complexity of the network is less pronounced with engineered cavities [5].

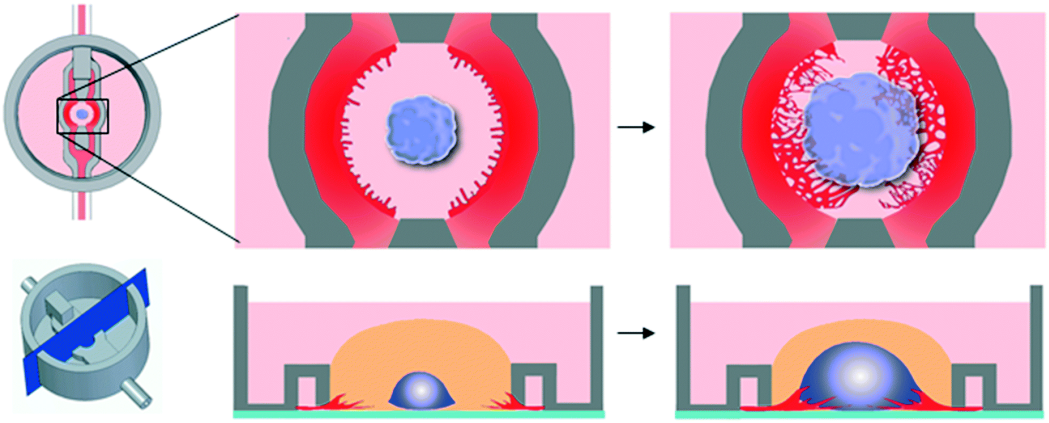

Figure 2.7: Schematic overview of the design of OoC-platform and intended vascularisation of cerebral organoid as reported in [58]. Sprouts of the vascular network spread towards the organoid in a central well through a 50 µm gap at the bottom of the channel. Reproduced from [58].

The state of the art of organoid vascularisation on-chip points to the need for a system that combines a realistic environment for the ECs to form strong networks (hemodynamic forces) with a convenient culture well for the organoid. To date, there is no on-chip approach available that offers the opportunity to repeatably create vascularised cortical organoids. Deduced from the presented cases above, it seems favourable to use two independent cell protocols and tailor the platform to their needs rather than cutting back on either of the two at the expense of the other. The advances described in [58] about 3D-printing the platform are a promising lead to create an accessible OoC-platform. However, the vessels mainly populated the surface of the organoid, which might be linked to the spatial constraints. Additionally, these efforts rely on a precisely timed co-seeding of the cells with off-chip initialisation of the maturation. Hereafter, two distinct cell protocols are presented for a 3D vascular network on-chip and a cortical organoid, respectively. They are intended to be co-cultured on the same chip with a transient separation which eliminates the need for relocating fragile cell cultures and which enables a flexible start of cross talking.

2.3. Cell Protocols for Vessel-on-Chip and Brain Organoid

This section contains the relevant information of the cell cultures that are employed in the scope of this master project. In order to design a OoC-platform that conveniently combines the spatial, mechanical, and accessibility requirements of the two protocols, a thorough understanding of the individual procedures is pivotal. Therefore, the details of the Vessel-on-Chip (VoC) and the cortical brain organoid (CO) are elaborated before a comparison between the main differences is drawn.

Before elaborating on the specific cell protocols, induced pluripotent stem cells (iPSC) are briefly introduced. iPSCs are stem cells which have been reprogrammed to a pluripotent, embryonic stem cell-like state. In an appropriate environment, developed somatic cells are genetically reprogrammed to a pluripotent level by forcing specific gene expression [70]. Pluripotent stem cells can be differentiated to different tissue types depending on the added growth media in the direct environment. By ”de-differentiating” somatic cells, researchers do not rely on embryos to generate in vitro cell cultures anymore; this has previously been a controversial approach [71]. At the same time, the tissue genesis can be tightly monitored and controlled, while obtaining tissue models of high compliance with the cell donors’ tissue. The protocols presented in the following both include the use of iPSCs to generate a vascular and brain model, respectively.

2.3.1. Vessel-on-Chip Protocol

The protocol for the engineered 3D Vessel-on-Chip is described in detail in [72]. The VoC consists of human induced pluripotent stem cells (hiPSC). These cell lines are generated from healthy individuals and patients reflecting the genetic background of the donor [73]. While being generally accessible for research, this allows for application in personalised medicine exploiting a high throughput of OoC

technology. Cuenca et al. combine ECs with vascular smooth muscle cells (VSMC) [72]. The addition of hiVSMC improved the self-organisation of the endothelial cells and supported the vessel stability. The result is a 3D vascular network exhibiting luminised and perfusable vessels based on hiPSCs on a microfluidic chip (Fig. 2.8).

The chip used in this protocol is the commercially available AIM Biotech idenTx chip. It features three adjacent channels, each with a separate inlet and outlet. The central channel is filled with a fibrin hydrogel laden with the cells. The flanking channels are used to supply medium and shear stress to the cells. The shear stress is generated by a gravity-driven flow as a result from adding 100 mL of medium to the inlet and 50 mL to the outlet of each medium channel [72]. The medium contains specific growth factors to promote network formation and is refreshed daily including recalibration of the inlet/outlet difference. After a culture period of approximately 7 days, a stable vessel network is formed.

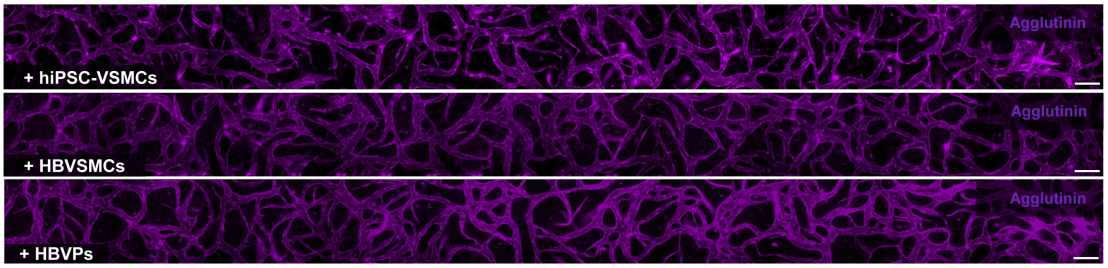

Figure 2.8: Representative immunofluorescence images of microvascular network showing hiPSC-EC (magenta; agglutinin) vessels spanning the complete length of the microfluidic channel. The image shows hiPSC-ECs cultured with hiPSC-VSMCs, HBVSMCs, or HBVPs, respectively. Scale bars are 200 µm [72].

2.3.2. Brain Organoid Protocol

The protocol established in [74] for the culturing of a cortical brain organoid is based on hiPSC. In the neural development as well as in adult brains, the interaction of neurons and astrocytes is critical [74]. Astrocytes promote the synaptic transmission between neurons and generally enhance the functional maturation of the brain. Therefore, a realistic model of the brain should include both cell types. One method to reach this in vitro, is to co-culture two different cell lines. While this approach allows for a higher experimental control of the ratio of the two components, it introduces variability by adding two strange cell lines together.

Another approach, as pursued in [74], is the differentiation of neurons and astrocytes from a common progenitor. This mimics closer the development of neural networks in vivo. The neuronal progenitor cells (NPC) are transferred to a coated 384-wells plate for cultivation at 37°C. The differentiation medium is exchanged every two to three days. In this process, a very gentle handling of the culture system is required. When verging on the cells too harshly, the risk of organoid damage increases. The mature organoid can reach a diameter of 2-3 mm and a height of approximately 200 µm. The culture period comprises approximately 35 days.

2.3.3. Comparison of Vessel-on-Chip and Brain Organoid Protocols

Table 2.2: Comparison of Vessel-on-Chip and cortical organoid protocols. The two cell protocols are the intended use case for the technology developed in this thesis and based on [72] and [74].

Parameter	Vessel-on-Chip	Cortical Brain Organoid
culture platform	commercial microfluidic chip	384 multi-wells plate
culture period	7 days	35 days
media refreshment	daily	every 2-3 days
environment	dynamic, requires shear stress	static, fragile during maturation

As mentioned above, both protocols use hiPSCs to build the respective tissue model. The environment in which the cells are cultured and the requirements they pose to their environment strongly differ. The

VoC is cultured on a three-channel microfluidic device. The flanking channels are filled with media while the central chamber provides the space to generate the vessel. The shear stress generated by the equilibration of the media through the medium channels makes it a dynamic culture environment.

By contrast, the brain organoid protocol makes arrangements to specifically avoid any (mechanical) disturbance of the cells during the maturation. The organoid is rather fragile and the disturbance, by, e. g. flow induced shear stress, potentially impedes the differentiation into a robust tissue model. To create the static culture environment, the organoid is placed in a well which offers sufficient volume for the medium. The resulting differences of the two protocols are summarised in Tab. 2.2.

Conclusively, the protocols do not have a natural overlap during the differentiation of the cells or the maturation of the tissue structures. However, as elaborated in the Sec. 2.2, the scientific relevance of organoid models is significantly reduced by the lack of vascularisation. Due to the high risk of necrosis in the core of the organoid, the longevity of the organoids is limited. Therefore, the design of a OoC-platform that can accommodate multiple, inherently different cell cultures as they are in the present case, is an ambitious goal with high potential.

2.4. Wax-based Composites

In the scope of this master project, a transient membrane is developed that temporally separates two chambers to create fundamentally different culture environments. The objective is to design a material, that functions as a barrier for the necessary maturation time but can be activated from off-chip to open the membrane. This section investigates biodegradable, hydrophobic composites made of wax enriched with functional particles. To inspect possible materials and methods to fabricate and activate this membrane, a systematic literature review was conducted focusing on wax-based composites with electrically conductive particles. Activation of the membrane means here the addressing of the filler particles in the intended way, e.g. electric field to trigger electrically conductive particles. A wax binder as matrix creates hydrophobic composites [75]. The thermal behaviour of wax conforms with phase change materials (PCM). PCM are latent heat storage materials which absorb and release a large amount of heat when changing their phase [76]. To illustrate, when transitioning from a solid to liquid phase, thermal energy is stored in the material, and released when re-solidifying, making them viable for energy storage applications [77]. Conversely, PCM exhibit isothermal phase change behaviour, i. e. they fulfil the transition at a constant temperature [78]. Selected results are presented hereafter. Additionally, the focus is shed on magnetic particles as active infill material for wax-based composites. As the elaborations below will show, magnetic particles are favourable in terms of activation due to the contact-less inductive heating and the cells' transparency to the magnetic fields.

2.4.1. Electrically Conductive Particles for Wax-based Composites

Electrically conductive composites were considered due to the vast availability of biodegradable conducting metals. The activation of these composites was expected to be possible in a straightforward set-up. Upon application of an electric field, it is hypothesised that the composite heats up due to Ohmic heating. The metallic particles form a conductive path through the composite, working as electrical resistor. Thus, part of the electrical energy is converted into thermal energy. The excessive heat results in a temperature rise in the surrounding of the particles heating up the matrix. Under sufficient applied voltage, the matrix carries out a phase change and can be flushed away from the location of the barrier. Hence, the membrane opens for cross-chamber exchange of vascular network and brain organoid.

In the literature, different waxes are combined with different conductive agents to create electrically conductive pastes, as listed in Tab. 2.3. Applications of these pastes are summarised in Fig. 2.9. Usually, they are used to build degradable circuit elements like antennas [79] and resistors [80]. Alternatively, a printed line can function as an interconnect in transient electronics [81]. Wax is used as binding matrix in conductive pastes hosting conductive particles. For this purpose, candelilla wax [81, 80, 82] and beeswax [79, 83] are the dominant waxes in the literature. Due to its hydrophobic nature, (natural) wax is a noticeable material for transient electronics, especially inside the human body.

Natural waxes are biocompatible and biodegradable organic compounds. As hydrophobic matrix, they host micro- or nanoparticles of conductive materials and provide thermoplastic properties to active

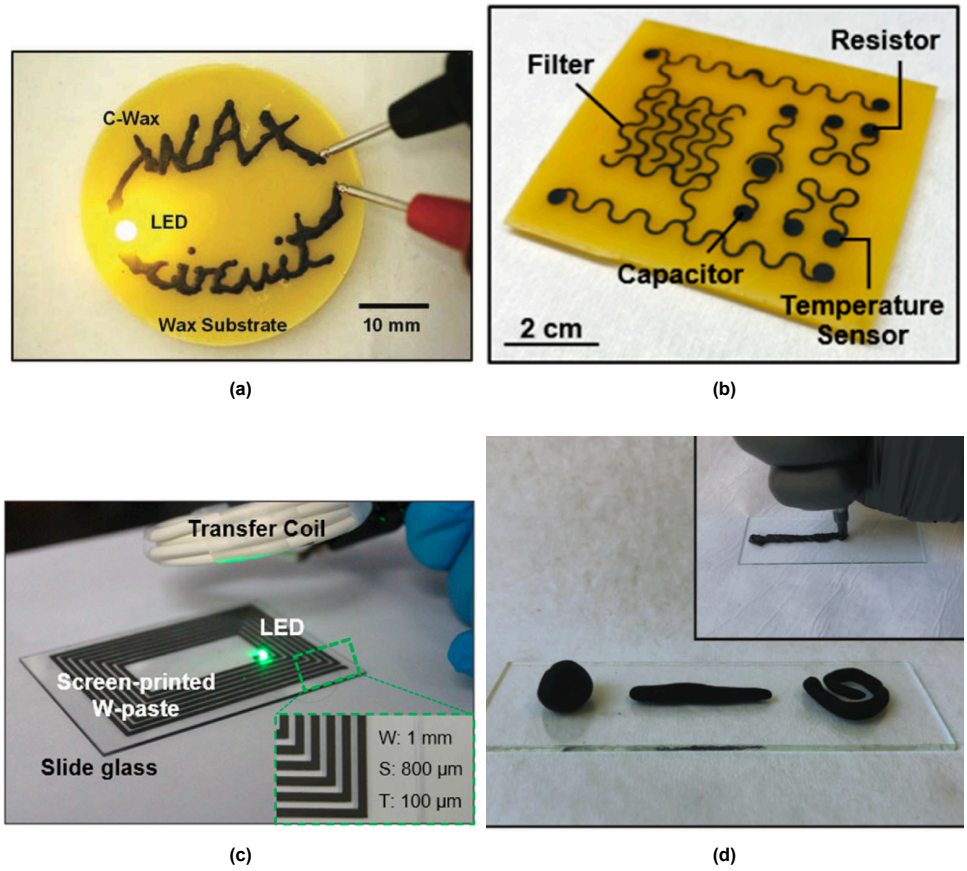

Figure 2.9: Application of conductive wax pastes. (**a**): Candelilla wax/Tungsten paste as interconnect to illuminate LED. Reproduced from [81]. (**b**): Candelilla wax/Molybdenum paste circuit with filter, capacitor, resistor and temperature sensor. Reproduced from [80]. (**c**): Beeswax/Tungsten paste as screen-printed antenna coil for power delivery. Reproduced from [79]. (**d**): Oleogel (Beeswax + vegetable oil)/Activated carbon paste printed on glass slide. Reproduced from [84].

and passive transient electronics. Thermoplasticity is a key factor for the intended target to compose an electrically triggered membrane. The works presented focus on applications as interconnects or circuit elements made of the composites (see Fig. 2.9). As such, the composites are tuned to reach maximal conductivity while remaining stable at and above physiological temperature. Key tuning points to increase conductivity are (1) the volume fraction of particles [81, 80, 82, 79] and (2) the particle size [79, 85].

To apply electrical activation to open the membrane, a high temperature build-up is required to trigger phase change of the composite. Since the composites exhibit a positive temperature coefficient when employed as resistor, low conductivity values are of interest. These can be reached with larger particles and a lower volume fraction, respecting the percolation threshold as discussed in Eq. 2.2.

$$\sigma = \sigma_0(\Phi - \Phi_c)^t, \tag{2.2}$$

where σ, σ_0, Φ and Φ_c are the conductivity, scaling factor, volume fraction of the particle, and threshold volume fraction (percolation threshold), and t is an index related to the conductivity above the percolation threshold (material dependent).

The mixing of the composites is a straightforward process. In the analysed works the matrix is heated to a liquid stage and the particles are mechanically stirred under. With exception of [84], the general process is solvent-free. Groups working with small particles utilised ultrasonic dispersion to enhance homogeneity of particles [80, 79]. Mechanical and electrical properties can be influenced with the addition of surfactants and lubricants [79, 82]. In terms of simplicity, these steps are considered optional

Table 2.3: Summary of electrically conductive wax pastes.

Components		Preparation	Conductivity in $S\,m^{-1}$
Matrix	Conductive Agent (size)		
Candelilla wax [81]	Tungsten (4-6 µm)	Mechanical mixing at 100°C	3500
Candelilla wax [80]	Molybdenum ($<$ 5 µm)	Mechanical mixing at 100°C, ultrasonic dispersion, PBS bath	14000
Candelilla wax [82]	Molybdenum (25 µm)	Mechanical mixing at 130°C	130
Beeswax [79]	Tungsten (500 nm)	Mechanical mixing at 100°C, ultrasonic dispersion of surfactant	6400
Beeswax + vegetable oil [83]	Activated Carbon (10-100 µm)	Mechanical mixing at 100°C	1
Beeswax [84]	Graphene powder (7-11 µm)	n-Hexane solvent, mechanical mixing, Vortex dispersion	60*

* Electronic transfer resistance in Ω.

and depend on the application. In small volume applications, more components reduce the fraction of conductive particles and could counteract their purpose.

Whereas the purpose of the investigated composites is to be biodegradable, the integrity of the composite for a defined period equally matters. While [81] investigated the water uptake rate of three different waxes, the comparison of the presented studies does not allow an unambiguous conclusion which binding matrix is favourable in terms of stability and longevity. [79] suggests that the addition of glycofurol increases the lifetime of the investigated composite. However, since there is no standard testing method, the results are not comparable. In addition, a potential mixture of different matrix components to tune certain parameters, e.g., the melting point, is not investigated. [83] reports an approach in which the addition of vegetable oil alters the rheological properties of the composite. Considering the application in a microfluidic device with a very small volume, this can be a promising tuning point.

2.4.2. Magnetic Particles for Wax-based Composites

A viable alternative to the electrical activation discussed above is the application of a magnetic field. Inductive heating, i. e., exposing magnetic particles to an alternating magnetic field (AMF), to generate heat is applied in the medical sector in the form of hyperthermia treatment. In magnetic hyperthermia, magnetic particles are injected into the human body and targeted with an AMF causing emission of heat to their surrounding [86]. The generated heat depends on the field properties field strength and frequency, but also on the size and concentration of the particles [87]. In hyperthermia treatment, usually nanoparticles are employed to interact with cellular and sub-cellular structures [88]. However, the risk of cytotoxicological effects limits the feasible particle concentration [89]. To avoid adverse interactions of the membrane with the cells on the OoC-platform of this master thesis, the focus is shifted to particles in the micron range.

Micro-sized particles are multi-domain particles. Those particles comprise several distinct areas which show locally saturated magnetisation [90]. In the presence of a magnetic field, the magnetic moments of these domains align with the direction of the magnetic field. When the magnetic field alternates its direction (AMF) at a high frequency, the magnetic moments of each domain lag with changing their direction. Therefore, the domain boundaries reconfigure by changing the intrinsic energy of the domain's crystalline structure. This oscillation causes an energy loss of the particles, which is the area of the so-called hysteresis curve (see Fig. 2.10 for different types of magnetic particles) [90]. The hysteresis curve depicts the magnetisation of a sample over a changing input magnetic field and is characterised

by three material depended parameters: the saturation magnetisation M_s, the remnant magnetisation M_r, and the coercivity H_c (Fig. 2.10) [91].

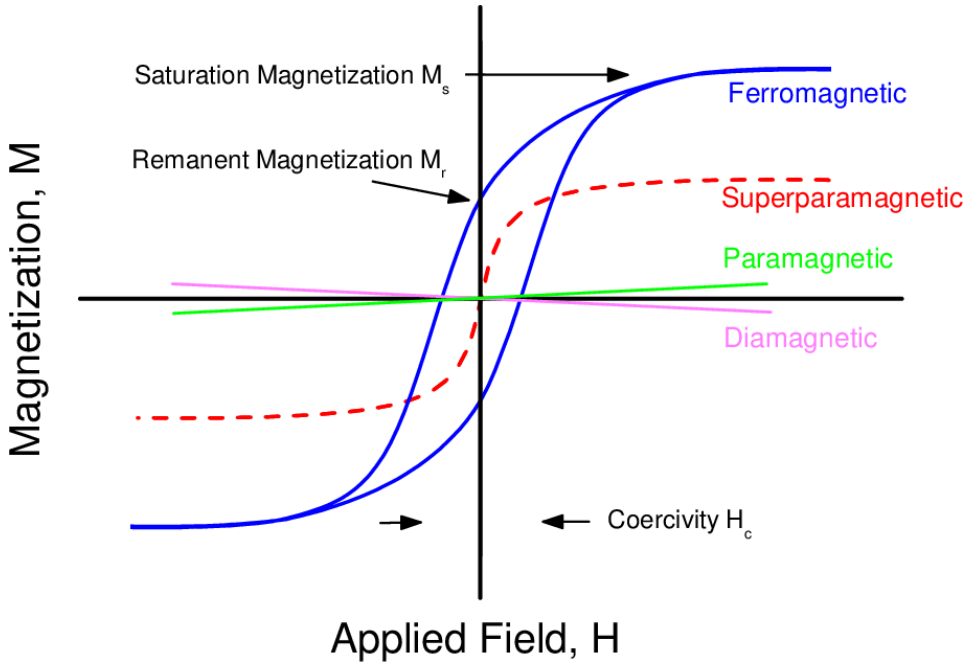

Figure 2.10: Hysteresis loops of different types of magnetic particles defined by the material properties the saturation magnetisation M_s, the remnant magnetisation M_r, and the coercivity H_c. Reproduced from [92].

With the objective to fabricate a wax-based composite activated by inductive heating, these parameters provide guidelines for the material selection. The heat generation mainly results from the hysteresis loss [90]. Therefore, a material exhibiting a large hysteresis loop is favourable. The dispersion capability of particles in a matrix is influenced by their remnant magnetisation. The higher M_r, the stronger the mutual attraction of the particles. This leads to particle agglomeration aggravating the mixing process [92]. Therefore, particles with low remnant magnetisation are preferred. The minimum applied field in order to initiate particle heat loss is determined by the coercivity [91].

To bring the findings together, it can be deduced that the inductive heating activation of magnetic particle/wax composites is preferred over the electrical activation discussed above for two reasons. First, the activation is possible in a contact-less manner. With the use of a coil, an AMF can be directed towards the region of interest circumventing the need for a physical connection. Second, the cells in the human body are transparent to magnetic fields with frequencies below 300 MHz [93]. As cells feature electrosensitive channels, the application of an electric field could disturb the maturation of cells cultured in the vicinity of the membrane. Due to the transparency to the magnetic field, the melting of the membrane can be initiated without interfering with the cells.

2.5. Concluding Remarks on Literature Study

The herein presented summary of the state of the art of OoC technology, vascularisation of brain organoids as well as the literature study on electrically conductive wax composites build the theoretical basis for the experiments of this master project. To summarise, Organ-on-Chip is a technology that aims to accelerate the drug development process by replacing animal models. Human induced pluripotent stem cells have emerged as alternative to create patient specific organ models in vitro in a reproducible and realistic manner.

Several examples exist for a multitude of cell types varying in fabrication method, material choice and overall design to construct realistic microenvironments. Amongst the replicated organs is the brain which is used for different lines of research, including study of neuronal pathologies and the development of novel drug systems. One approach to replicate brain tissue is in the form of organoids, which

represent a complex replication of the target organ in terms of structure and development. However, the lack of vascularisation for organoids risks necrosis. Several efforts to integrate a vascular network to organoids of different organs have been made, including the vascularisation of brain organoids. However, to date there is no information available about a single chip solution which allows this multi-cell cultivation. The presented protocols for a Vessel-on-Chip on the one hand and for cortical organoids on the other hand, independently exemplify robust methods. The fusion of these two approaches is considered a promising outlook to create truly vascularised organoids.

Wax composites are hybrid materials with suitable properties to act as temporary, non-porous membrane to create on-chip separation of different cell cultures. Owing to its hydrophobicity and biodegradability, those materials are expected to repel the cell culture media while avoiding the introduction of toxic elements to the cells. Infill particles allow to functionalise the wax composites. As discussed above, metallic particles like tungsten or molybdenum lead to conductive composites. The use of magnetic particles would yield a composite which is sensitive to an external magnetic field to enable opening the membrane in a contact-less manner.

2.6. Research Question and Objectives

Combining the previous research, this report documents the research and experiments undertaken to produce an Organ-on-Chip platform which cultivates two different cell types. Accordingly, this master thesis aims to answer the following research question:

> *How to develop an Organ-on-Chip platform for multi-cell culture with transient separation of a brain organoid and vascular network?*

From this research question, the following objectives arise:

1. Design of OoC-platform that accommodates and supports the maturation of two different cell cultures at the same time.
2. Establishment of a fabrication procedure to repeatably provide the platform for collaborating researchers.
3. Design of a membrane to separate the cell cultures for a defined time frame.
4. Integration and removal of the membrane to enable fusion of two different cell cultures.

The objective of this master project is to design, fabricate, and test a OoC-platform that accommodates a three-dimensional vascular network and a cortical brain organoid. Along the development of this platform, the progress of the project and the reasoning for certain experiments is carefully documented. The project includes the characterisation of the components in order to make an informed evaluation of the results possible.

3

Materials and Methods

This chapter describes the approach to answer the research question of this master project. For both the OoC-platform as well as the transient membrane the utilised materials and methods for fabrication and characterisation are described. The chapter details the conducted experiments and formulates the targeted investigations of the master project. First, the developed design of the OoC-platform is described with a focus on the distinct features accounting for the incorporation of two inherently different cell culture environments. Subsequently, the fabrication process as well as the material are presented. The second pillar of this master project is the design and fabrication of a biodegradable membrane. The selected materials and methods for fabrication are explained before describing the conducted experiments for injection and evacuation of the membrane.

3.1. OoC-platform for Co-culturing of Brain Organoid and Vascular Network

In this section, the design and fabrication process of the OoC-platform is presented. The selected material is discussed and subsequently, the methods for characterisation of the platform are described.

3.1.1. Design

The design of the chip was driven by the aim to create an OoC-platform that combines the structural requirements the Vessel-on-Chip and brain organoid cultures impose on their microenvironment. The herein developed chip enables the independent application of the cell protocols described in Sec. 2.3, while incorporating cross talk between cell cultures in a controllable manner. The design was based on the properties of the cell cultures and the culture platforms in the protocols as summarised in Tab. 2.2. The design features an open-well chamber in the centre for culturing of the organoid (Fig. 3.1). The chamber splits a central gel channel which is flanked by one medium channel on each side intended for the vascular network formation (Fig. 3.2). A membrane channel was introduced accommodating space for the integration of a transient membrane between the central chamber and the gel channel (Fig. 3.4). The specifics of the chip are described in this section. Overall, the design is presented in three levels: (1) the top level defining the outer dimensions, (2) the channel level defining the microstructures and cell compartments of the OoC-platform, and (3) the membrane level. All elements were designed using the CAD software Fusion 360.

Top level design: Outer dimensions

The 3D-model of the chip is depicted in Fig. 3.1 with the outer dimensions of the device. The dimensions on this level were determined by the integration into the imaging workflow and the required media volumes. For imaging purposes, the length of the chip was set to 25 mm to comply with the size of a standard microscopic glass slide. By choosing the same value, the chip was equipped for imaging without changing the standard workflow. The bottom thickness of the chip was set to 0.17 mm to reduce the distance light has to travel through the bulk during imaging. This reduces light absorption by

Table 3.1: Critical features and their dimensions in the top level of the design with V for volume, h for height, w for width, l for length and d for diameter of the structure.

Feature	Defining Dimensions
Bottom Plate	w = 16 mm, l = 25 mm, h = 0.17 mm
Organoid Chamber	V = 139.4 µL, h = 11.5 mm
Media Inlet	V = 54.3 µL, d = 4 mm
Gel Inlet	V = 14.2 µm, d = 3 mm

molecules in the substrate and the risk of scattering of the light beams. Thus, the focusing and imaging of the cells is facilitated. The hereafter specified height values are assumed from the top surface of the bottom plate. The width was optimised to be as small as possible to increase the fabrication efficiency while containing sufficient space for the chambers and inlet structures.

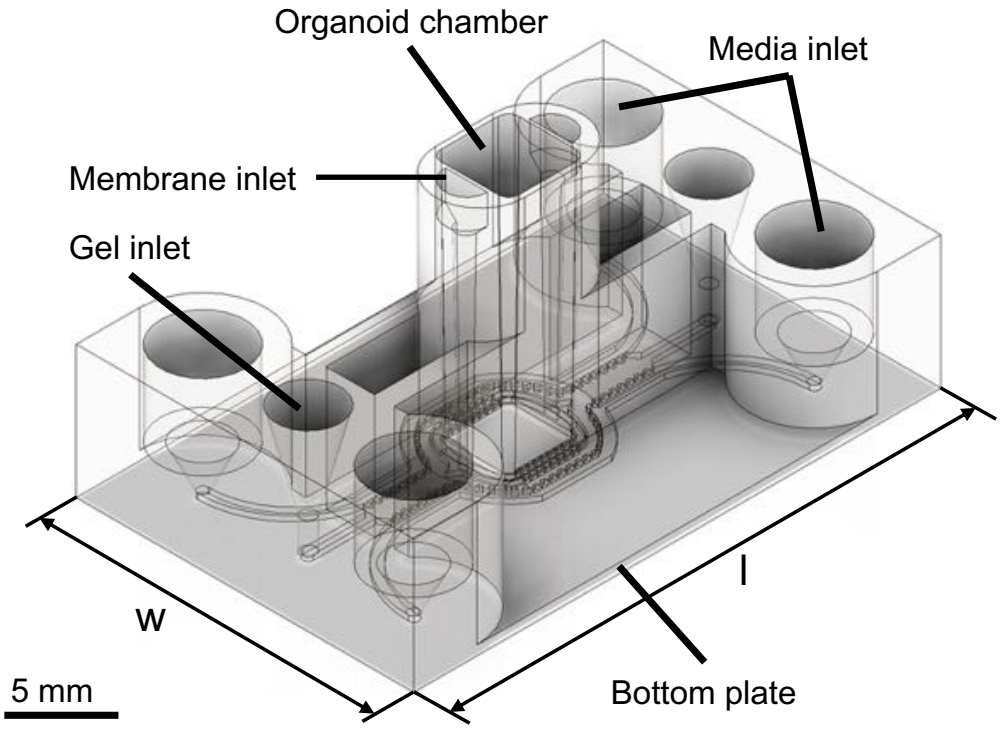

Figure 3.1: 3D model of the OoC-platform for the vascularisation of brain organoids.

The dimensions of the organoid chamber were matched to fit sufficient media volume, as described in the organoid protocol. With a height of 11.5 mm, the chamber comprised a volume of 139.4 µL. The inlet/outlet structure was fitted to the required volume for injection of medium and gel for the VoC protocol, respectively. The inlet volume of the media channel was set to 54.3 µL with a maximum diameter of 4 mm and a height of 6 mm. The same parameters for the gel inlet were set to 14.2 µL, 3 mm and 6 mm, respectively. The dimensions were optimised in close correspondence with the collaborator seeding the VoC to optimise the handling of the cell culture. The most important dimensions on this chip-level are summarised in Tab. 3.1.

Channel level design: Direct cell environment

The design of the channels is crucial since they made up the direct environment of the cell cultures. The design of the channels is depicted in Fig. 3.2 with definition of the dimensions. Channel widths and pillar size are reported in Tab. 3.2. The separation of the two channels with the pillar array has two reasons. First, the pillars confine the gel in the gel channel after injection due to the surface tension of the fluid bridging the gap. In this way, the cells are trapped inside the gel channel in which the network

formation occurs.

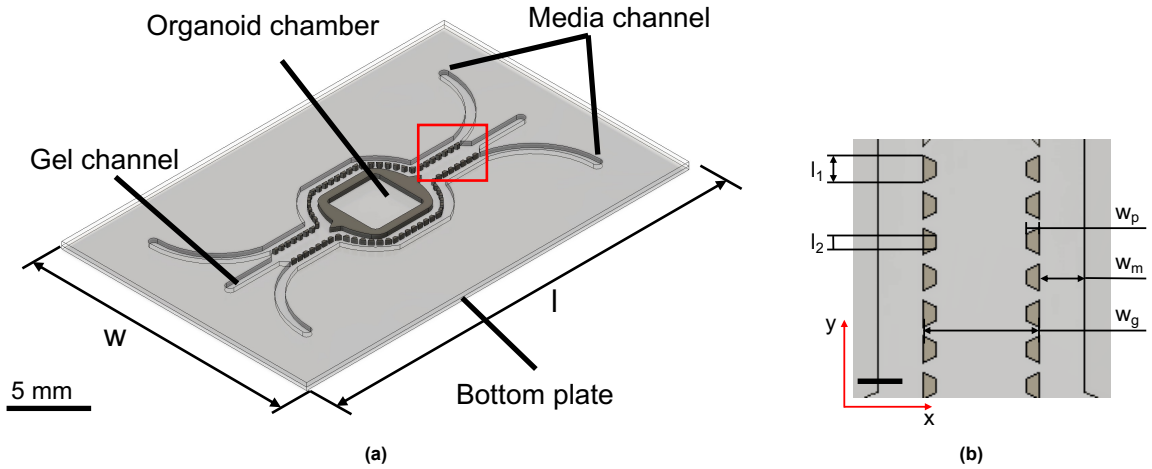

Figure 3.2: Channel level design of herein developed OoC-platform. The channel level makes up the direct cell culture environment. (**a**): Media channel, gel channel and organoid chamber as direct cell environment. Red area magnified in 3.2b. (**b**): Pillar array separating gel channel w_g from adjacent media channel w_m. Scale bar is 0.5 mm.

Second, the pillar structure is exploited to transmit the shear stress to the cells in the gel channel. As depicted in Fig. 3.3, the induced shear stress in the central channel from applied flow in the flanking channels was increased in the presence of micropillars [94]. A similar three-channel configuration was designed for the channel on this chip to efficiently generate shear stress on the endothelial cells. In this cell protocol, the shear stress was generated from the flow of the medium in the media channels. The shear force originates from a relative motion of a fluid alongside a stationary phase [94]. The stationary phase is in this case the pinned liquid-liquid interface between the media and the gel. The flow in the media channel results from gravitational forces. With a difference in the height of media level in inlet and outlet, the liquid tends to equilibrate this difference by transporting media to the side of a lower fluid level. By this equilibration process, a flow is generated that exposes the cells in the gel channel to a shear stress. Since the flow is driven by the height difference of the fluid level in the media inlet and outlet, the velocity is not constant, but slows down with progressing equilibration. The generated flow refers back to the top level design of the media inlet volume.

The gel channel was split by the organoid chamber to culture the organoid on the same height as the vascular network. The distinct features of the channel level design and their critical dimensions are reported in Tab. 3.2.

Table 3.2: Critical features and their dimensions in the channel level of the design with h for height, w for width, l for length and r_c for radius of rounded corners of the structure.

Feature	**Defining Dimensions**
Media Channel	w_m = 0.5 mm, h = 0.25 mm
Gel Channel	w_g = 1.3 mm, h = 0.25 mm
Pillar Array	tapered geometry w_p = 0.15 mm, l_1 = 0.3 mm l_2 = 0.15 mm, h= 0.25 mm
Organoid Chamber	square with rounded corners w_o = 3.3 mm, r_c = 0.3 mm, h = 0.25 mm

Membrane Level Design: Transient cell culture separation

The design of the wall of the organoid chamber on channel level as presented in Fig. 3.2 introduced a permanent barrier between the compartments for the different cell cultures. This configuration, referred to as ”single-culture” was used to investigate the biocompatibility of the chip and its workflow integration with the cell protocols. Before fusing the cell cultures on the chip, the compatibility with the individual protocols was established. To enable the cross talk between the cell cultures on the chip, a membrane

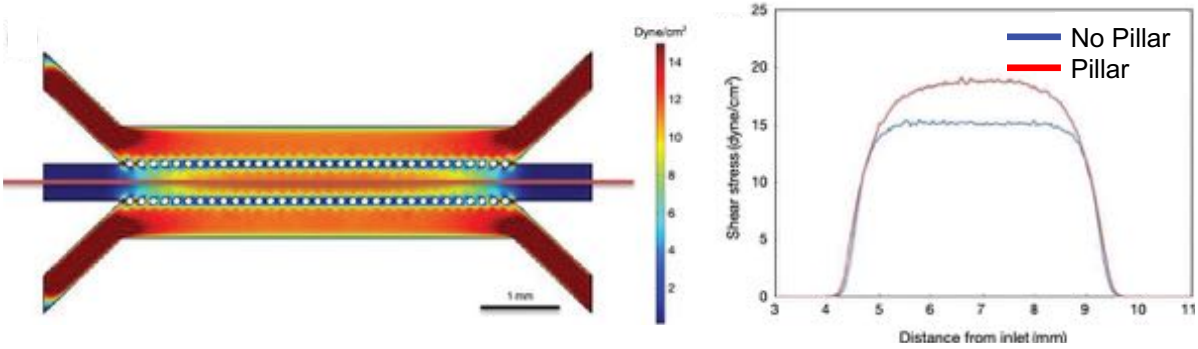

Figure 3.3: Influence of micropillars on distribution of shear stress in a three-channel microfluidic system. Colour map of simulation of shear stress and simulation results with and without micropillars alongside the red line. Reproduced from [94].

channel was introduced to the organoid chamber wall, yielding the ”two-culture” configuration. The implemented membrane channel is shown in Fig. 3.4. Without injection of the membrane material, this would be an open space for cell-cell exchange. To confine the membrane in the designated area while creating a void for the sprouts to penetrate after opening the membrane, the channel was bordered with two arrays of pillars. With the implementation of pillars rather than a horizontal gap, the whole channel height of the vascular network can be used for migration towards the organoid. The pillar geometry and gap width was optimised in experiments which are described in Sec. 3.3.1. The width of one membrane channel were set to w_m = 0.3 mm and the length of the pillar array to l_m = 2.5 mm. The total capacity of one membrane channel on channel level is approximately 0.5 µL.

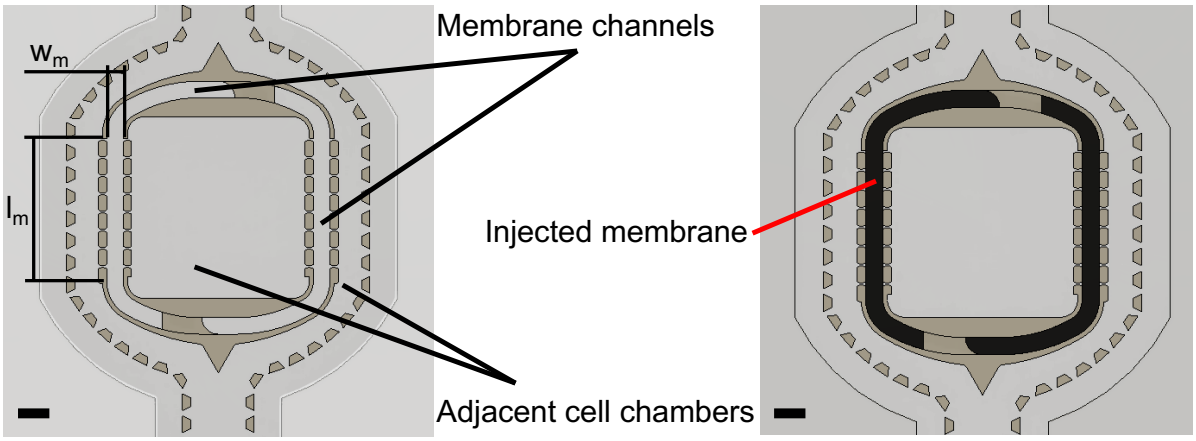

Figure 3.4: Design of the membrane channel between the two adjacent cell culture chambers in the ”two-culture” configuration. On the right image, the injected membrane to separate the vascular network and the brain organoid is visualised in black. Scale bar is 0.5 mm.

The membrane inlet was integrated to the wall of the top level organoid chamber (see Fig. 3.1). In this manner, the channel could be reached via a vertical path, rendering the inlet suitable for gravity-induced injection of the membrane. Additionally, the inlet featured a cavity with the exact volume of the channel capacity to facilitate the injection of the correct amount of the membrane material. The membrane channel is shown in Fig. 3.4 with and without the depiction of the injected membrane.

Selected Fabrication Method

The fabrication method selection was based on the design and the results of the literature study (Sec. 2.1.2). The design features multiple channels that require leakage free separation. The pillar arrays as separators of different channels are difficult to fabricate with soft lithography since this requires bonding of the channel structure to a bottom plate. The multitude of small contact areas aggravate the exact alignment of the structures. In addition, the chip shows critical dimensions in a several heights of the design. The dimensions of the inlets are essential for the generation of a shear stress on the vascular cells and the inlet of the membrane channel defines the quantity of injected material. The design

freedom and 2.5D-fabrication progression of the DLP process combined with the good accuracy of the technology motivated the decision to choose this method. The classification as 2.5D-fabrication refers to the fact the process progress indeed handles 2D information of the layer, but the layer thickness adds a distinct expansion of that plane in Z-direction.

3.1.2. Fabrication

The OoC-platform (hereafter also ”part”, ”chip”) was fabricated with the DLP printer Asiga MAX X27 manufactured by Asiga. The machine employs an UV laser at 385 nm for resin curing. The DMD has a resolution of 27 µm in the X-Y-plane setting the upper planar resolution limit. The resolution in Z-direction is dependent on the layer thickness which is determined by the user and can be varied over the height of the part. The lower the layer thickness, the higher the resolution and the smoother the vertical surfaces. The post-processing of the part used isopropyl alcohol (IPA) and deionized (DI-) water to clean the part. The clean device was post-cured with UV light using the Otoflash G171 UV-flash-device. This tool generates UV-flashes with a frequency of 10 Hz. It features a spectrum from 280 nm to 700 nm. A dedicated post-processing protocol was established which is elaborated in Sec. 4.1.1.

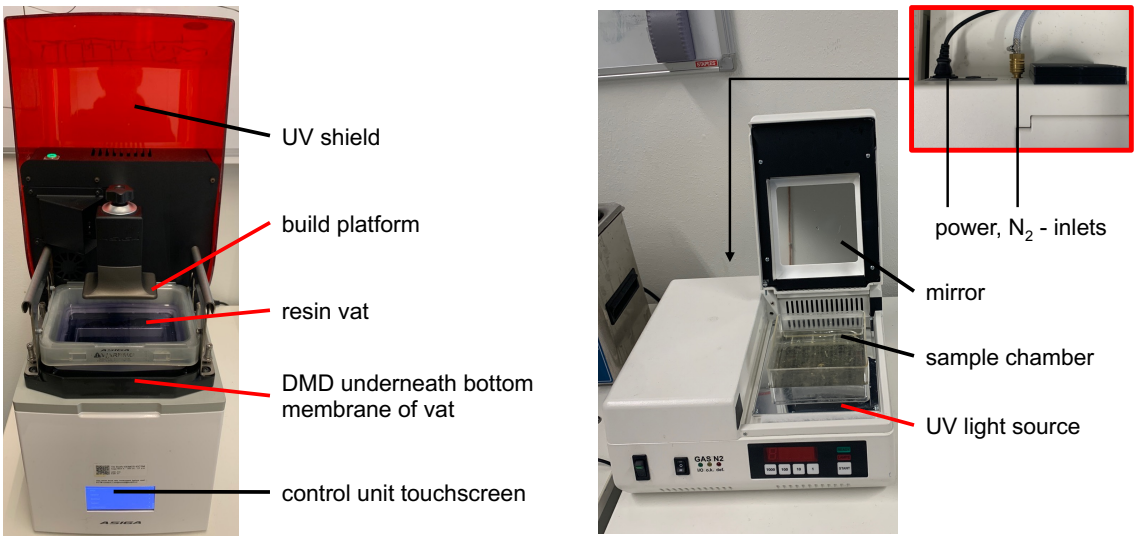

Figure 3.5: 3D-printer and UV-curing device for OoC fabrication. (**a**): DLP printer used for the fabrication of the chips and all other 3D-printed samples/parts. The part is built hanging upside down from the building plate by successively submersing it in the resin tray. For each dip one layer of the part is printed by illumination with 385 nm DMD. (**b**): UV-flash-device for sample curing in post-processing. The sample is positioned in the sample chamber. The mirror reflects the UV-flashes in the whole chamber. Optionally, the chamber can be filled with N_2-gas during the curing process.

The part was designed with the CAD software Fusion 360. The CAD model was exported as STL object and transferred to the control unit (desktop PC) of the 3D-printer. One fabrication process combined three times the same part to create one chip with three multi-cell culture devices. For this, the STL object was imported three times to the composer software of the printer and the spacing between the parts was set to 0 mm. This configuration used the maximum build space of the printer.

3.1.3. Material Selection

Photoinduced curing was the basis of fabricating the part with DLP. This refers to the polymerisation of monomers or resin to a solid state initiated by UV light [50]. In DLP-resins, a photo initiator (PI) is added to the monomer. The absorption of UV light by the PI leads to the creation of free radicals which initiate the polymerisation of the monomers. This leads to the cross linking of the polymer chains, hence a durable solid [95]. As deduced from the literature review in Sec. 2.1.1, the material must support high spatial resolution and high transparency for imaging. The selected material to fit these requirements was the commercially available resin MOIIN TECH clear. It is a photocurable resin composed of methacrylate monomers mixed with photo initiators. As described in Sec. 2.1.2, materials for DLP are

cross linked upon irradiation with a distinct wavelength. The selected material has an absorption peak at 385 nm at 30°C matching the specifications of the available machine exactly. The material properties determine which wavelengths either can pass through the material without significant scattering or are absorbed. The resin to print the chip is transparent in the necessary range for bright-field as well as fluorescence microscopy [96].

The material choice is a high-quality resin available in the lab during the master thesis and is suitable for the Asiga MAX X27 DLP printer. The high transparency and spatial accuracy to print microstructures and cavities were the main motivation to select this material. Correspondence with the manufacturer confirmed that use cases demonstrated biocompatibility of the material. Therefore, the material choice was made in accordance with the elaborated material property requirements in Sec. 3.1.3.

3.1.4. Characterisation Methods

Three parameters were selected to access the quality of the produced chip based on the literature study (Sec. 2). These are the dimension accuracy, transparency of the channels, and the biocompatibility of the fully processed chip. In the following, the methods to evaluate the chip following the three parameters are elaborated.

Dimensional Accuracy

Meeting the dimensions of the chip is important to maintain the sufficient volume and spacing for the cell cultures. The footprint of the chip was measured with a calliper. The pillar size in X- and Y-direction as well as the inlet diameter were captured with a microscope and analysed with the DinoXcope software. The optically investigated elements are shown in Fig. 3.6.

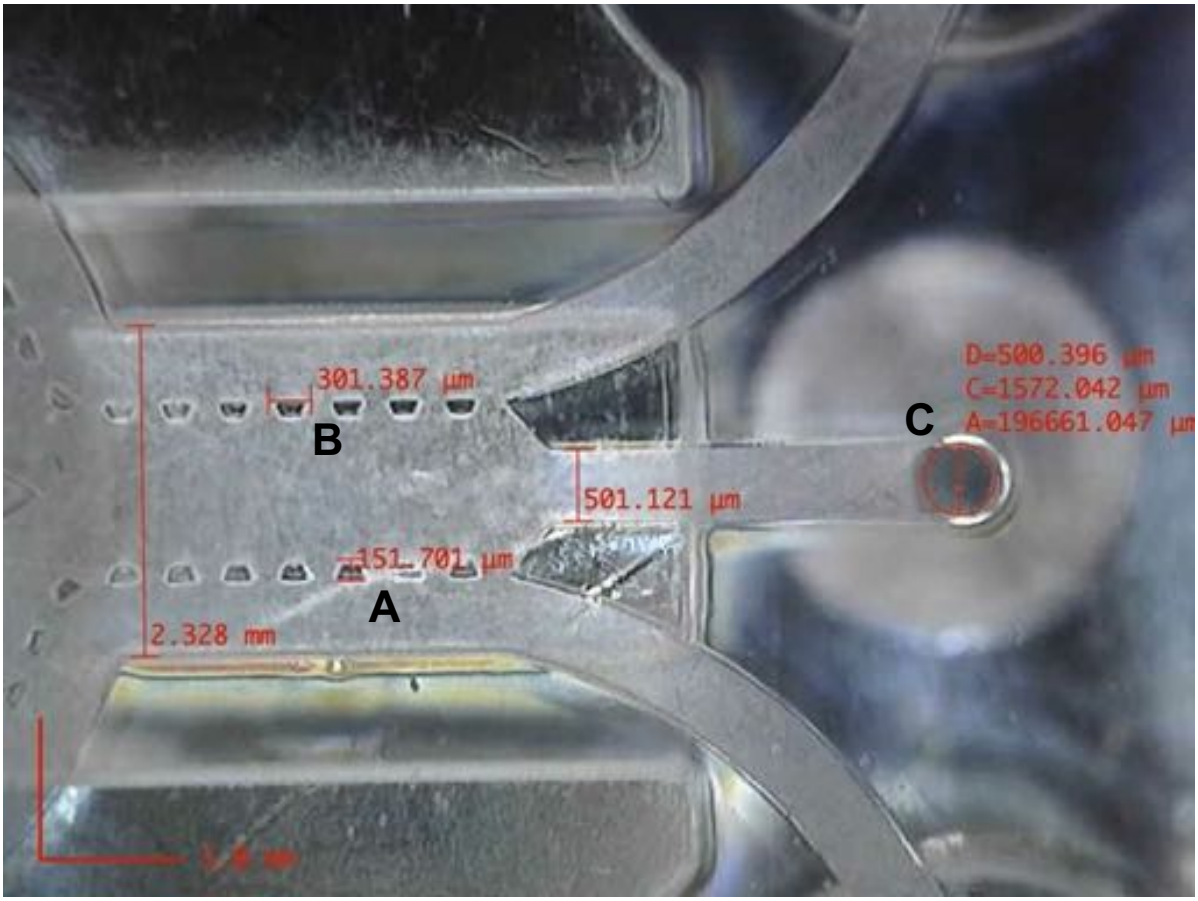

Figure 3.6: Microstructures investigated for dimensional accuracy with DinoXcope microscope. **A**: channel width (X-direction), **B**: channel width (Y-direction), **C**: inlet diameter. Scale bar is 1 mm in the bottom left corner.

Transparency of Bottom

The transparency of the platform is a crucial element as explained in Sec. 2.1.1. A main issue with 3D-printed parts is the surface roughness of the bottom layer which matches the surface roughness of the build platform. A rough surface scatters incoming light and reduces the transparency of otherwise transparent bulk materials. In order to improve this parameter, the post-processing of the fabrication was extended by an extra step as depicted in Fig. 3.7. The chip was mounted on a glass slide with a thin layer of uncured resin as ”glue”. The thickness of the layer was controlled with consumer grade tape. Two stripes were taped to the glass slide with a distance of 46 mm such that the chip just sat on the tape. The nominal height of the tape was 60 µm creating a gap between chip and glass slide. The gap was filled with 1-2 drops of uncured resin. To fully cover the bottom face of the chip with resin, a second glass slide was mounted to the top of the chip and taped to the bottom slide. The uniform pressure expelled air bubbles from the resin and spread it evenly. The construct was cured with 500 UV flashes to bond the liquid resin to the bottom of the chip. Subsequently, the glass slide was detached from the chip to reveal the treated surface.

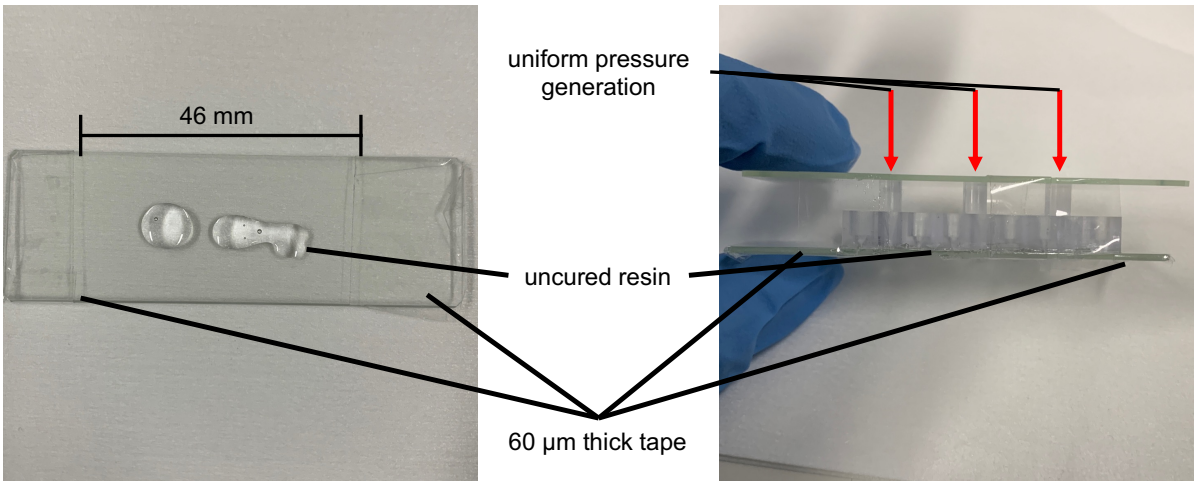

Figure 3.7: Methodology to create a smoother bottom face to increase the transparency of the chip.

The transparency was qualitatively tested with the dinoXscope microscope by comparing the visibility of microfluidic structures before and after the addition of a new bottom layer. Additionally, the feedback from the biologists was included in this step by reducing the total bottom plate thickness.

Biocompatibility

The material’s biocompatibility is a key prerequisite in order to successfully build a multi-cell OoC-platform. The manufacturer did not label the material officially biocompatible. Therefore, early prototypes in the ”single-culture” configuration (see Sec. 3.1.1) were shared with the biologists to assess survival rate of the cell cultures on the chip. As reported in Sec. 2.1.1, resins for DLP-printing usually consist of toxic monomers. For this reason, an intensive post-processing protocol was established as documented in Sec. 4.1.1.

3.2. Biodegradable Membrane for OoC-platform

3.2.1. Material Selection

The materials to construct the biodegradable membrane are selected based on the requirements of the membrane. These are determined to be biodegradability, functionalisation, and hydrophobicity. The membrane is sought to be biodegradable to ensure that the materials as well as their by-products from reactions with the cells and media do not harm the cell cultures. In addition, the barrier between the cell cultures must vanish to enable vascularisation of the organoid. The biodegradation of considered materials progresses autonomously and spans over a specific time. To extend the natural mechanism and provide a mean to control the opening by external activation, the matrix is filled with functionalising particles. Additionally, while intact, the membrane must not be permeable to water to maintain separation of media and minimise the probability of cell penetration. As described in Sec. 2.4, composites of

wax (referred to as matrix hereafter) enriched with particles are suitable to meet all three criteria.

Matrix

The matrix of the membrane consumes the main volume fraction of the membrane, and acts as the physical, hydrophobic barrier between the cell cultures. Candelilla wax, beeswax, bayberry wax and wool wax (lanolin) have been considered. All candidates are biodegradable and hydrophobic. The degradation process of these materials is described as surface erosion [81, 79]. The degradation proceeds layer-by-layer or from the edges towards the centre, while the substance beyond the degradation front is still intact.

The decisive factor for the matrix is its melting point in a physiologically not harmful range. This range was determined with the cumulative-equivalent-minutes (CEM43-) model, which gives an indication of the thermal load for tissue at a given temperature [97]. It provides a normalisation formula to convert time-temperature exposure to an equivalent exposure time at 43°C given in Eq. 3.1. To illustrate, this method computes the temperature dose the cells are exposed to in time t at temperature T in terms of how long it would take to cumulate the same dose at 43°C, which was set an arbitrary reference point.

$$CEM43 = \int_0^t R^{43-T}\, dt = tR^{43-T} \tag{3.1}$$

where R is a correction factor with $R = 0.5$ for $T \geq 43°C$, $R = 0.25$ for $T < 43°C$ [97].

Prior to experimentation, the material selection was narrowed down to bayberry wax (BBW) and lanolin due to their favourable melting point regions. BBW consists of the wax esters triacylglycerol, diacylglycerol, monoacylglycerol. The fatty acids of the ester are saturated and make the wax highly hydrophobic [98, 99]. As glycerolipids, the fatty acids condense on glycerol, a natural alcohol [100]. While the mechanism of biodegradation of BBW has not been studied in particular, the chemical composition of the wax indicates that it is decomposed by hydrolysis. This means that the wax esters of the material are split into the alcohol glycerol and the condensed fatty acid in the presence of water. This compares to the degradation reported for other natural waxes like candelilla wax [81]. Lanolin or wool wax is an animal wax secreted by sheep to build a water protection layer on skin and wool [101]. It consists of multiple alcohols and fatty acids condensed to wax esters [102] that mix well with molecular structures of the BBW. Concerning the biodegradability of lanolin, the material consists to 95 % of wax esters from fatty acids and fatty alcohols. Lanolin mixes with water but does not dissolve in water [103, 104]. The main degradation mechanism of lanolin is the cleavage of the wax esters through hydrolysis. The main ester in lanolin is cholesteryl palmitate which decomposes to cholesterol and palmitic acid via hydrolysis [105]. Cholesterol is insoluble in water. In the human body, it occurs as a component of the cell membrane in brain tissue, hence, is not harmful for the cell culture. Palmitic acid is a biocompatible substance exhibiting no cytotoxicity, as reported in [106].

The commercially available BBW of *Natural Heroes* is used as raw material. Depending on the brand and exact origin of the natural wax, the melting point of BBW varies. It is estimated to be in the range of 40 - 55°C [107, 81]. 100 % pure lanolin was purchased from Prounol. The manufacture claims a nominal melting point at 36°C. At room temperature, lanolin had a pasty consistency. Fig. 3.8 presents the matrix raw materials at room temperature.

Particles

The particles are added to the matrix as active agent to fulfil the second membrane requirement of functionalisation. Carbonyl iron powder (CIP) and iron(II,III) oxide (magnetite, Fe_3O_4) are well-established materials for biomedical applications featuring biocompatibility and biodegradability [108]. CIP (cat. no. 44890) and magnetite (cat. no. 310050) were purchased from Sigma-Aldrich. Both powders consist of particles in the size range of 1-10 µm.

The general degradation process of iron species is through oxidation of the metal [109]. The oxidation is an electrochemical reaction. The anodic and cathodic reaction as well as their reaction to the most common corrosion product are given in Eq. 3.2 [109]:

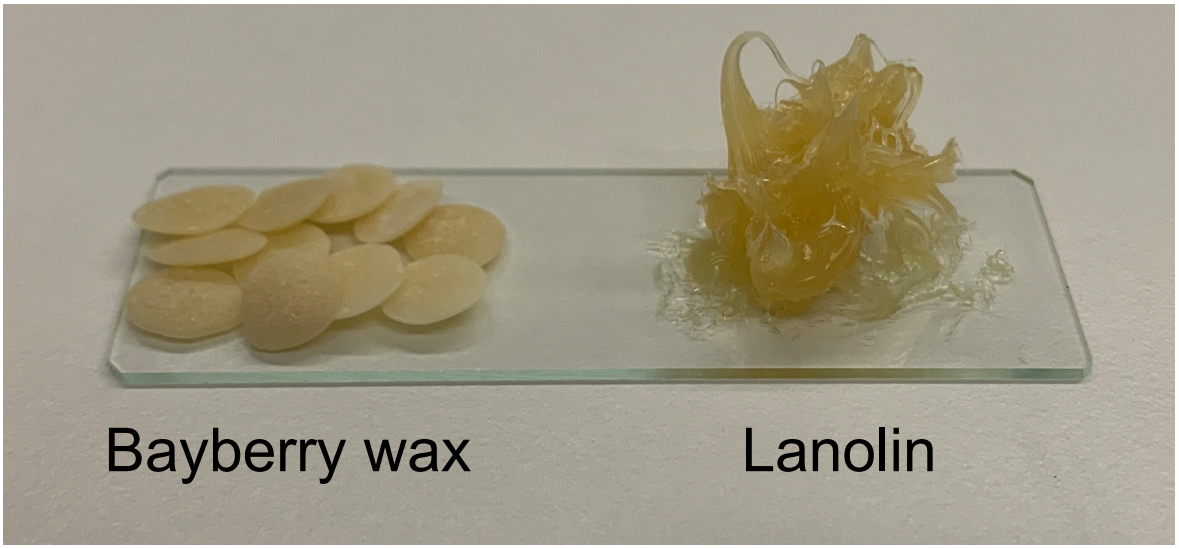

Figure 3.8: The two raw materials used to fabricate the matrix of the biodegradable membrane. Bayberry wax was completely solid and distributed in pellet form. Lanolin exhibited a pasty, sticky consistency.

$$\begin{aligned} Fe &\longrightarrow Fe^{2+} + 2e^- \\ O_2 + 2H_2O + 4e^- &\longrightarrow 4OH^- \\ Fe^{2+} + 2OH^- &\longrightarrow Fe(OH)_2 \end{aligned} \tag{3.2}$$

In the human body, other iron corrosion products can be detected from reactions with sodium, chloride, carbon, and phosphorus. These can either be absorbed by organs and further decomposed or excreted as metabolic waste [109]. CIP particles are highly pure iron and therefore exhibit the degradation mechanism elaborated above. They were proved to be biocompatible and to not leading to toxicity while featuring low hemolytic effects in [108]. In vivo, due to the low corrosion rate, the particles are often absorbed in the blood system and exuded via renal filtration [110]. The formation of an oxide layer has been observed as a result of CIP degradation creating iron oxides. This influences the magnetic behaviour of the particles since iron oxides show lower saturation magnetisation than CIP [111]. Potentially toxic corrosion products of iron are hydroxyl radicals (HO·) [112]. They result from reactions of Fe^{2+} with hydrogen peroxide. While the use of CIP has generally shown no adverse local or systematic disturbance of the biological system, HO· has been identified as one of ”the most potent oxidising agents highly reacting with all biological macromolecules and with significant pro-inflammatory properties” [112].

Due to the short culture period relative to the degradation time of iron on this thesis' OoC, the corrosion of the particles is expected to have low influence on the cell cultures. Nonetheless, the established biocompatibility is crucial for the intended application and supports the selection of iron-based particles.

3.2.2. Fabrication

Mixing

The membrane composite was fabricated in two consecutive steps. In the first step, the matrix was manufactured in a melt-mixing process. To design a matrix which melts at approximately 43°C, the two raw materials, BBW and lanolin were mixed in different volume fractions. For a total volume of V_M and a volume fraction X of one component, the volume (V_1, V_2) and mass (m_1, m_2) fractions of the two components were calculated in the following manner:

$$
\begin{aligned}
V_M &= V_1 + V_2 \\
V_1 &= \frac{m_1}{\rho_1} = XV_M \\
m_1 &= \rho_1 X V_M \\
V_2 &= \frac{m_2}{\rho_2} = (1-X)V_M \\
m_2 &= \rho_2 (1-X) V_M
\end{aligned}
\tag{3.3}
$$

with ρ_1 and ρ_2 as the densities of the two components of the mixing process.

The average density of the different matrix compositions ρ_M was calculated with Eq. 3.4:

$$
\rho_M = \frac{(m_1 + m_2)\rho_1 \rho_2}{m_1 \rho_2 + m_2 \rho_1} \tag{3.4}
$$

The materials were weighed and added together in a glass vial, before heating the mixture in an oven to approximately 60°C until all phases were liquid. The liquid samples were mixed with a vortex mixer (Fisherbrand ZX3) for at least 60 s at 2000 rpm to reach uniform mixing of the two components.

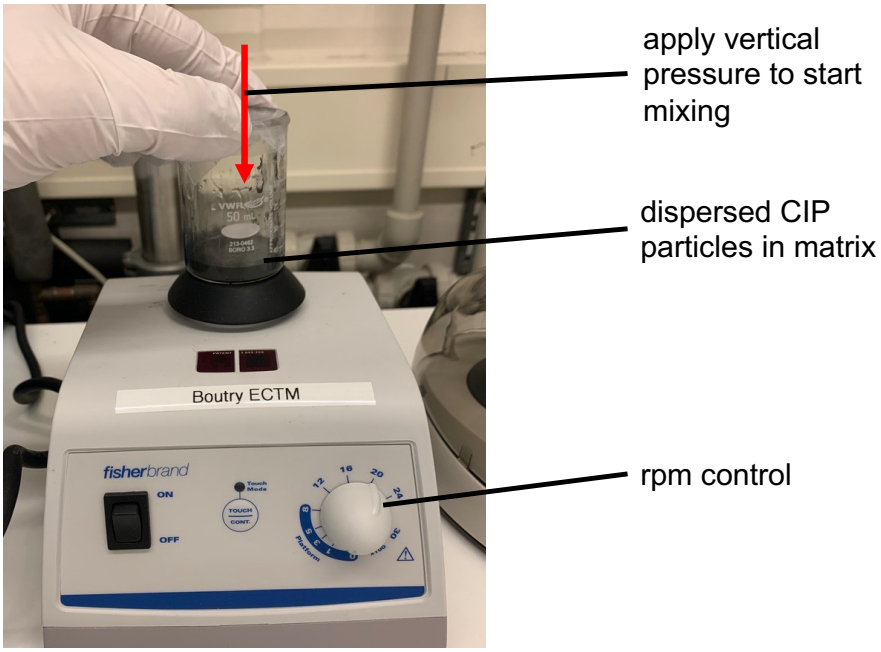

Figure 3.9: Experimental set-up for the melt-mixing of the membrane material. The matrix and particles were heated together until the matrix liquified. The glass vial was gently pressed against the vortex mixer to start the mixing and to keep the sample in place during the process.

In the second step, the composite was manufactured by mixing the matrix with magnetic particles as described in the literature study for other wax composites (see Sec. 2.4). The necessary compound masses to achieve the desired particle volume fractions were calculated in the same manner as the matrix described in Eq. 3.3, where X was then the particle volume fraction. The matrix and the particles were added to a glass vial and heated to approximately 60°C. Upon melting of the matrix, the samples were mixed with a vortex mixer for at least 120 s at 2000 rpm until homogeneous particle dispersion was observed. The mixing set-up is depicted in Fig. 3.9. The targeted quantities for the fabrication of 1 mL matrix with 40 vol.-% BBW as well as 1 mL composite with the same matrix with 10 vol.-% CIP are exemplary given in Tab. 3.3.

Table 3.3: Density of raw materials and of 40 vol.-% matrix. Mass values m for the fabrication of 1 mL matrix and 1 mL composite, respectively.

Process	Volume Fraction*	Component 1		Component 2	
		ρ [g/mL]	m [g]	ρ [g/mL]	m [g]
Matrix	0.4	BBW		Lanolin	
		0.985	0.394	0.940	0.564
Composite	0.1	CIP		Matrix	
		7.86	0.786	0.958	0.862

* of component 1.

3.2.3. Characterisation Methods

The fabrication and characterisation of the composite included several methods to access the behaviour and functionality of the membrane. In the following, the conducted measurements in the scope of this work are described in detail. The underlying physical principles or techniques are explained theoretically. Subsequently, the experimental design is elaborated. For this, the characterisation based on SQUID-, DSC-, and Inductive heating measurements are explained to assess the magnetisation of particles, thermal properties of the matrix, and composite behaviour in a magnetic field, respectively.

Magnetisation

A superconducting quantum interfering device (SQUID) magnetometer was used to determine the magnetisation of magnetic particles. Essentially, SQUIDs are flux-to-voltage transducers, by generating an output voltage which is proportional to a change in the magnetic flux [113]. The SQUID is used as a specific type of magnetometer. The goal of magnetometry is to measure the magnetisation M or magnetic moment m of a sample [114]. An overview of the physical principle behind SQUID measurements is provided in the following.

SQUIDs exploit the principle of superconductivity as well as the Meissner and Josephson effect [115]. In short, superconductivity describes a material behaviour at temperatures close to the absolute zero. Certain materials transition from a state of common electrical resistance to resistance less performance when cooled down below a critical transition temperature T_c. According to the Bardeen-Cooper-Schrieffer theory, below T_c electrons weakly pair up due to lattice vibrations into Cooper pairs. Cooper pairs are able to traverse the material without scattering, hence do not exhibit any resistance [116]. T_c is a material property influencing the superconductivity of a material jointly with kinetic and magnetic interactions of the electrons [115].

The Meissner effect describes the behaviour when a superconducting element is subjected to a magnetic field. In the transition to superconductivity, the magnetic flux is expelled from the material. In case the superconductor is utilised as a coil, a constant magnetic flux through the ring is the result. This is due to the induced current through the coil when the magnetic field is turned off. Since there is (almost) zero resistance in the superconducting state, the current is persistently generating a constant magnetic flux through the ring. Additionally, the trapped magnetic flux inside the loop can only take discrete values, i. e. multiples of the flux quantum [115].

In the loop configuration, Cooper pairs are able to tunnel short resistive regions without breaking off the superconducting current as long as the current remains below a threshold I_c, which is referred to as the Josephson effect [117]. In SQUID, these principles and effects build the foundation of the measurement. A superconducting loop containing at least one Josephson-junction is inductively coupled to an external magnetic flux. The junction(s) are biased with a current slightly above I_c such that there is a voltage drop across the junction. With variation of the external flux, the voltage changes periodically with the period of the magnetic flux quantum. The change of the voltage can be linked to the external magnetic flux [115]. The change of external flux results from mechanically moving the sample through a pick-up coil [114].

The MPMS 5XL SQUID manufactured by Quantum Design was used for measuring the hysteresis

curve of the samples. The sample weight for all measurements was around 2.3 mg. The sample was loaded into a plastic capsule with the lid tucked in reverse. Additionally, the edge of the larger part was sealed with tape to fix the package as depicted in Fig. 3.10. The capsule was mounted in a plastic straw which was attached to the rod of the machine. To avoid slipping of the capsule in the straw, it was punctured with a pin needle. The displaced material of the straw slightly protruded such that it fixated the capsule at its position. The positioning of the sample with respect to the pick-up coil of the SQUID was performed automatically by the machine prior to the measurement. The targeted sample position in the machine was 1.5 cm.

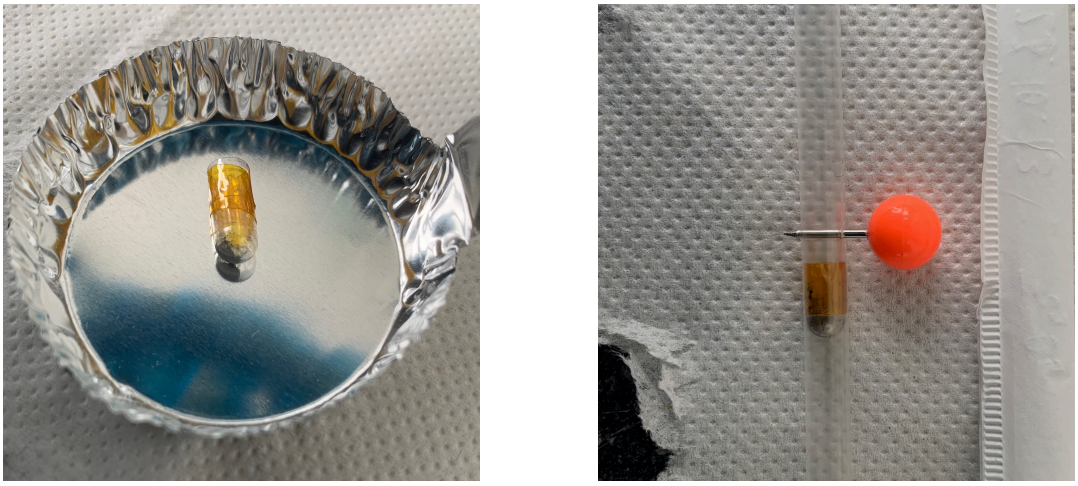

(a) (b)

Figure 3.10: Sample preparation for the SQUID measurement with the MPMS 5XL SQUID magnetometer. (**a**): Weighed sample prepared in capsule. The small lid is tucked in upside down and edge of the bigger lid is sealed with tape. (**b**): The straw is punctured above and below the capsule to trap it at the desired position and avoid slipping during the measurement process.

The measurement sequence was designed to collect the magnetisation of the sample over the sweep of a magnetic field at constant temperature. The temperature was set to 310 K (36.85°C) and the B-field ranged from -1 to 1 T. Around zero field, it was incremented in 0.01 T steps and from |0.1 T| to the edges in 0.1 T steps. Specifically, the input unit is Oersted (Oe), which in vacuum corresponds to $1\text{Oe} = 10^{-4}\text{T}$. The measurement was performed in the reciprocal sample option (RSO) mode.

Thermal Properties of the Matrix

The thermal properties of the matrix and composite were investigated using differential scanning calorimetry (DSC). The result of the measurement is the heat flow from the sample over temperature and time and the heat capacity of the sample over temperature and time. Changes in these parameters indicate thermal events in the sample such as glass transition, crystallisation, and melting. In this project, DSC was used to determine the melting point of different matrix compositions to render it applicable for cell cultures. All measurements were performed on the DSC Q2000 manufactured by TA Instruments. The sample was sealed in an aluminium pan and placed on a thermoelectric disc inside the furnace next to an empty reference pan of same the kind. As the furnace temperature changes, heat is transferred into the sample and the reference pan from the thermoelectric disc. The differential heat flow to the sample and the reference pan is measured by area thermocouples according to Eq. 3.5:

$$q = \frac{\Delta T}{R} \tag{3.5}$$

where q is the sample heat flow, ΔT the temperature difference between sample and reference pan, and R the resistance of thermocouple. For the analysis, the heat flow was normalised to the sample mass ($Q = q/m$).

The heat capacity was measured simultaneously with the heat flow using the Tzero™ technology developed by TA instruments. The furnace was purged with nitrogen at 50 mL min^{-1} flow rate. Approx-

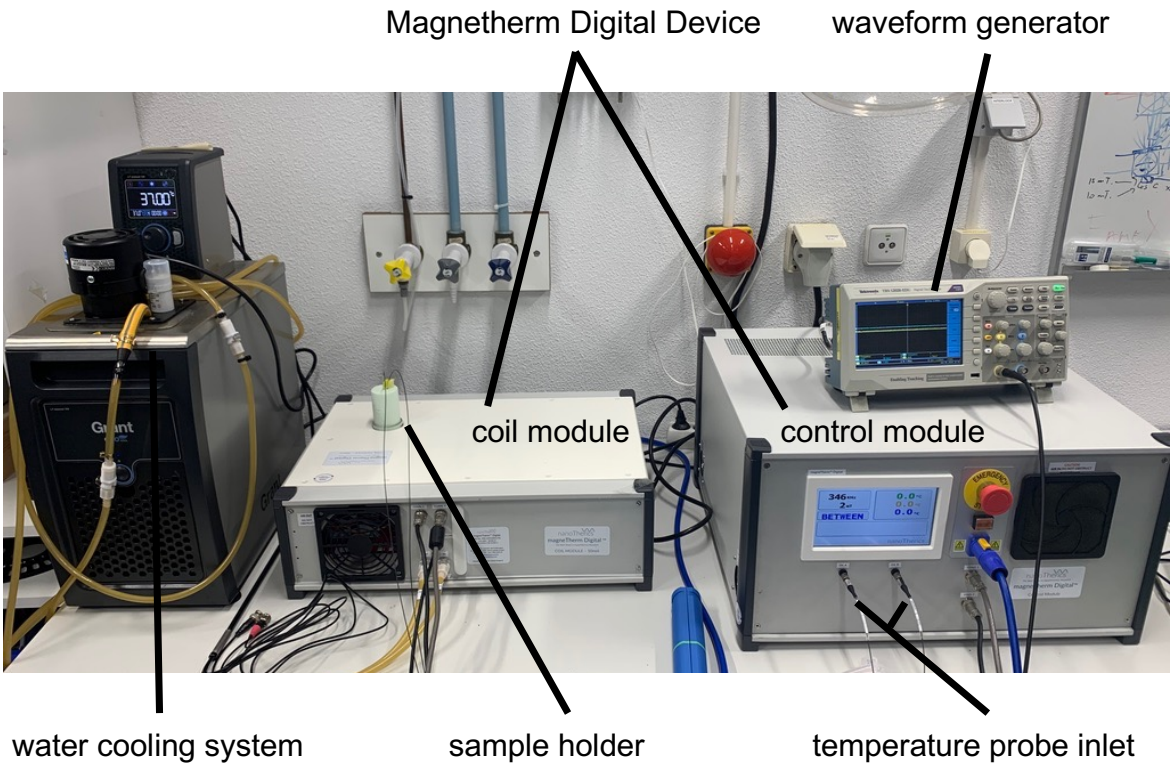

Figure 3.11: Experimental set-up for inductive heating testing. The alternating magnetic field is generated by the AC source connected to the coil in the left element of the Magnetherm device. The sample is inserted into the centre of the coil that is cooled down with a water cooling system. Two temperature probes inserted in the sample record the temperature over time.

imately 20 mg of the sample was encapsulated in a Tzero^{TM} aluminium pan and sealed in a dedicated press. The exact sample mass was recorded together with the mass of the empty sample pan. All measurements were non-isothermal, i. e., the heat flow through the sample with respect to the reference pan was measured over temperature. The temperature ranged from 0 to 70°C to include all relevant thermal events in the region of interest of the application. The temperature was increased/decreased with a rate of 10 K min^{-1} with a 2 min isothermal hold at the turning points of the cycle. One measurement included a double heating-cooling cycle. The first cycle was used to eliminate the thermal history of the sample by heating above the melting point and subsequently letting it cool down to the initial temperature. Additionally, this led to a more uniform and flat sample positioning in the sample pan which shall increase the reproducibility of the measurement.

The obtained DSC-curve (T-Q) was analysed using the software Universal Analysis from TA Instruments. The melting point, melting onset temperature, and melting enthalpy were graphically determined. The melting point for polymer(-like) materials is defined as the peak value of the melting range [118]. The melting enthalpy (or enthalpy of fusion) is the amount of energy required to melt 1 g of the solid sample to liquid phase [119]. It was determined as the total area between the melting peak and the base line in the DSC-curve by numerical integration.

Inductive Heating

The heating behaviour of the magnetic composite in the presence of an alternating magnetic field was experimentally investigated with the set-up shown in Fig. 3.11. The independent variables in this experiment were the particle volume fraction in the composite and the strength of the magnetic field. Twelve different experimental conditions were set-up to determine how the heating of the composite changed in dependence of the two independent variables (Tab. 3.4). The heating efficiency was expected to change more efficiently with varying the field strength compared to the frequency of the field [120]. Therefore, the composites were investigated at a fixed frequency $f_{AMF} = 346.5$ kHz. The measurements were performed with the Magnetherm Digital manufactured by Nanotherics. The

Table 3.4: Experimental conditions of inductive heating characterisation. The frequency of the alternating magnetic field is constant for all conditions at $f_{AMF} = 346.5$ kHz.

Independent Variables Inductive Heating Experiment				
		B-Field Strength in mT		
		2.5	5	10
Particle Fraction in vol.-%	0	$IH_{00\_2.5}$	IH_{00_5}	IH_{00_10}
	3	$IH_{03\_2.5}$	IH_{03_5}	IH_{03_10}
	10	$IH_{10\_2.5}$	IH_{10_5}	IH_{10_10}
	25	$IH_{25\_2.5}$	IH_{25_5}	IH_{25_10}

device contains a coil which generates an alternating magnetic field in its core upon application of an alternating current. The field strength B in T is directly proportional to the input current I as given in Eq. 3.6.

$$B = \mu_0 n I,\ n = \frac{N}{L} \tag{3.6}$$

where μ_0 is the magnetic permeability inside the coil ($4\pi 10^{-7}$ H m^{-1} in air), N the number of turns of the coil and L the length of the coil in m.

The coil in the system has 17 turns and a length of 50 mm. For each sample, approximately 1 mL of the composite was filled into an Eppendorf tube and the sample mass was recorded. The tube was mounted in the centre of the coil with use of sample holder. Two glass fibre optic thermometers were inserted in the sample to measure the core and bottom temperature of the sample. Both temperatures were recorded to assess the homogeneity of heating throughout the sample volume.

The measurement of one experimental condition yielded the temperature profile at both locations over time. The measurement parameters were programmed with a custom user interface. The interface enables the user to set the field parameters (strength, frequency), the duration of AMF exposure, the time recorded pre- and post-exposure and the number of repetitions of the same parameter set. The temperature was equilibrated until it varied less than 0.5°C s^{-1}. The water-cooling system was set to 37°C to create a thermal environment for the sample similar to the intended application. The recording of the temperature started 60s before the AMF was switched on to capture the starting conditions of each experiment. The sample was exposed to the AMF until either (1) one of the temperature values exceeded 45°C, or (2) no significant temperature change within 5 min of exposure was detected. For each field strength, an exposure profile was defined that was applied for all four particle fractions. The profile was based on the expected temperature rise for the 25 vol.-% sample to satisfy criterion (1). Repeated measurements were conducted consecutively, with a between-exposure-time adapted to the expected heating behaviour to reach similar starting conditions for each repetition. The data was recorded with a sample rate of 1/s.

The experimental data resulted in two temperature values. From the temperature measured at the core of the sample, the heating rate (HR) and the specific loss power (SLP) of the samples were calculated. To receive the heating rate, the starting and end temperature of an AMF exposure cycle was extracted manually from the data table. The heating rate was calculated with Eq. 3.7.

$$\text{HR} = \frac{T_{off} - T_{on}}{t_{off} - t_{on}} = \frac{\Delta T}{\Delta t} \tag{3.7}$$

with temperature T in °C and time relative to the start of recording t in s.

The SLP was calculated with

$$SLP = C\frac{\Delta T}{\Delta t}\frac{m_s}{m_p} \tag{3.8}$$

where C is the specific heat capacity of the sample, m_s is the mass of the sample, m_p is the magnetic microparticle mass in the composite, and ΔT/Δt is the heating rate of the sample after switching on the AC magnetic field [87].

Biodegradability

A biodegradability study was drafted to test the degrading behaviour of the membrane material. The degradation is monitored by reference to three parameters: change of dry mass, change of wet mass and water uptake, and change of dimensions. To mimic the application environment, the samples will be soaked in a glass vial filled with PBS (pH 7) in an incubator at 37°C. The initial sample parameters are recorded at study day 0 and subsequently every 7 days. To conduct the measurements, the samples are removed from the incubator and allowed to cool down to room temperature in the glass vial. The wet mass is weighed after flushing the sample with compressed air to remove surface water. Afterwards, the sample is dried in a vacuum desiccator for 2 h to remove excess liquid and the dry mass is recorded. A separate line of samples is dried and gauged with an optical microscope. The measurements are distributed on different samples to reduce the stress on the material to a minimum. For both the recording of the masses and the recording of the dimensions, 10 samples are prepared to have an average of 10 values for each data point.

The samples were prepared with casting the melted composite in PDMS molds. PDMS molds were fabricated by using 3D-printed master samples. 20 master samples were taped to the bottom of a glass petri dish to avoid underflow of PDMS. The molds were surface treated with saline. For this, the petri dish was placed inside a desiccator with a few drops of saline added to a separate petri dish. After 1 h of salinisation in vacuum at room temperature, the saline evaporated and deposited on the master surface. 10:1 PDMS (PDMS-prepolymer:curing agent) (Slygard 184 elastomer kit) was cast over the master molds. The PDMS was degassed in a second desiccator in vacuum for 1 h to release bubbles from the material and the PDMS was allowed to cure at room temperature for 48 h.

3.3. Integration of Biodegradable Membrane to OoC-platform

3.3.1. Injection of Membrane

The integration of the membrane in the chip added an additional processing step and was investigated experimentally and with numerical simulation. To establish an integration process that reliably filled the membrane channel while constraining the composite from flowing into cell chambers, several membrane channel border geometries were investigated (Fig. 3.12). The pillar geometry as well as the pillar gap G that were varied in this experiment. For this, a test structure was designed with Fusion 360 that included a replica of the membrane channel of the chip design presented in Sec. 3.1.1 reduced to the relevant components and dimensions of its direct environment.

Experimental Approach

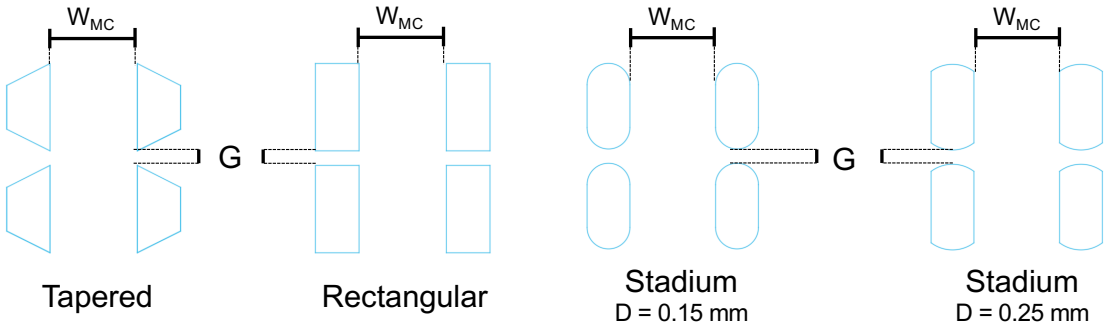

Figure 3.12: Design of micropillars for membrane channel confinement. The channel width w_{MC} is equal for all configurations. The gap G is defined equally for all configurations as the point of smallest distance between two pillars.

The design was 3D-printed with the same DLP printer and material as the chip and underwent the same post-processing steps to allow translation of the results from the test structure to the final design. In total, four different pillar geometries were investigated as shown in Fig. 3.12. For each, three different gap sizes G were tested (30 µm, 50 µm, 100 µm). 30 µm was selected as lower limit to comply with the resolution of the 3D-printer of 27 µm. This resulted in a total of twelve experimental conditions in the form "[pillar geometry, gap size]" which were combined in a single test structure with two channels of each configuration. The goal was to identify the geometry with the best material confinement while leaving the widest gaps possible for the vessels to penetrate the organoid chamber. The shapes were selected with an intuitive approach. In essence, triangular, rectangular, and circular pillar geometries are implemented when considering the opposing faces of two pillars across the gap G. The expected underlying principle for confining the material in the channel was that the surface tension of the fluid is large enough to be pinned in between two pillars laterally while the resistance inside the channel is kept to a minimum to progress through the channel. For all configurations, the maximum length of the pillars was the same. The material was loaded to the inlet storage described in Sec. 3.1.1 in solid state. The chip was heated to approximately 45°C to melt and fill the channel by gravity induced flow. The outcome was evaluated as successful when the material progressed into the membrane channel. Slight spillage to the adjacent channels was tolerated as long as they were not completely blocked by the material. The outcome was quantified as yield for each configuration by dividing the amount of successfully filled channels over the total sample size.

Numerical Simulation

Next to the experimental approach described above, the same channel configurations were analysed with a numerical approach. The 3D-models of the different [pillar geometry, gap width]-configurations were imported to COMSOL Multiphysics 6.1 with specified 3D coordinates. For fluid flow simulation, a non-compressible laminar flow model was chosen, a fitting selection given the small scale and low Reynolds number characteristics of microfluidic chips. The material of the fluid was defined by the density and the dynamic viscosity at the injection temperature. Their estimation is described below. Computational fluid dynamics (CFD) was integrated into COMSOL Multiphysics. Meshing was executed with a swept mesh incorporating 8 layers of distribution, resulting in a total of 7000-8000 mesh elements depending on the 3D-model. The simulation model was developed in close collaboration with a PhD student from the Biodegradable Technologies Group at ECTM, TU Delft.

Boundary conditions were established by defining a non-slip wall condition for the microfluidic channel. The inlet pressure was maintained at a constant 115 Pa, while the outlet pressure was set to 100 Pa. The inlet pressure resulted from the gravity induced sinking of the liquid membrane material. Therefore, the inlet pressure was determined as the weight force of the loaded material over the area of the membrane inlet A_{in}. It was estimated in the following manner:

$$\begin{aligned} V_{\mathrm{M}} &= 0.5\,\mathrm{mm}^3 \text{ (see membrane channel design, Sec. 3.1.1)} \\ m_{\mathrm{M}} &= 1.648\,\mathrm{g\,mL}^{-1} V_{\mathrm{M}} = 0.824\,\mathrm{mg} \\ A_{\mathrm{in}} &= 0.07\,\mathrm{mm}^2 \\ P_{\mathrm{in}} &= \frac{m_{\mathrm{M}} g}{A_{\mathrm{in}}} \approx 115\,\mathrm{Pa} \end{aligned} \tag{3.9}$$

The density of the composite was estimated in accordance with Eq. 3.4 as the average density of the components. The dynamic viscosity was roughly appraised from the experiment described with Fig. 3.13a. A planar surface (small petri dish) was suspended over a water bath on a hot plate. The evaporated steam was partially captured by the downwards facing side of the petri dish uniformly heating up its surface. On the heated surface, a 3D-printed test structure with one membrane channel was placed. A thermometer was taped to the same surface to measure the exact temperature at the place of the channel. A camera was positioned with an adjustable food to capture the gravity induced infill of the fluid into the channel.

From the video recordings of the material flowing in the membrane channel, the flow rate Q could be estimated. Q is defined as transported volume of the fluid through the channel per second. The flow

rate of the fluid is connected to the pressure difference at inlet and outlet over the hydraulic resistance R of the microfluidic channel.

$$\Delta P = RQ \tag{3.10}$$

In turn, R is dependent on the channel cross section geometry [121], which is rectangular in the present case:

$$R = \frac{12\eta L}{1-0.63(h/w)} \frac{1}{h^3 w} \tag{3.11}$$

with L, h, w the length, height, and width of the channel, respectively. Eq. 3.10 and Eq. 3.11 were combined to obtain the following expression for the dynamic viscosity η of the fluid:

$$\eta = \frac{\Delta P}{Q} \frac{1-0.63(h/w)}{12L} h^3 w \tag{3.12}$$

The simulation results were analysed to understand the effects of different micropillar geometries and gap widths on the confinement of a fluid through the channel. As a parameter for this, the fluid velocity and its distribution were examined. The degree of spillage was determined as the fluid velocity outside the pillar array. Fig. 3.13b indicates the definition of inlet and outlet of the membrane channel. Additionally, a line data set was defined in the adjacent channel just outside the pillar array. Alongside this line, the spillage velocity of the fluid was analysed at z $= 0.125$ mm.

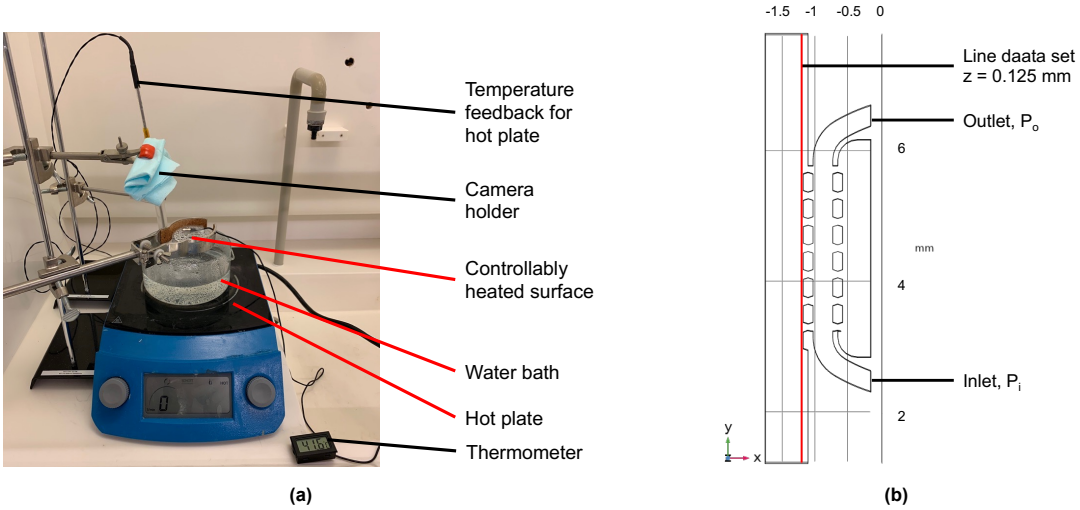

Figure 3.13: Experimental set-up for determination and dynamic viscosity and definition of simulation parameters. (**a**): Experimental set-up for a rough estimation of the dynamic viscosity of the membrane material. The petri dish surface was heated by the steam of the water bath. The onside temperature was recorded with a thermometer taped to the exact position of the material loaded channel structure. (**b**): Definition of the inlet and outlet of the 3D model. The red line indicates a line data set at half channel height. The spillage of the fluid was analysed alongside this line as the fluid velocity.

3.3.2. Evacuation of Membrane

Whereas the membrane was designed to withstand media penetration and cell culture cross talk, the aspired vascularisation of the membrane requires the removal of the barrier. The process of opening the membrane was expected to rely on two mechanisms. Firstly, the biodegradable property of the components leads to a successive reduction of membrane material. With progressing hydrolysis, the water uptake of the matrix potentially increases as described in Sec. 2.4. The water uptake increases the probability of cell penetration. Secondly, the functionalisation of the matrix with magnetic particles enabled to force membrane melting. As evacuation method, the application of a constant air flow was investigated to push the liquified membrane out of the channel. The experimental set-up described in Fig. 3.13a was used to establish a proof-of-concept. The membrane was injected into the channel of

the test structure. A syringe pump was connected via a flexible tube (inner diameter 0.5 mm) to the inlet of the test structure. The connector was custom made by cutting off the tip of a syringe with a 4 mm Luer connecter and taping the flexible tube to it. The connection was sealed with an additional layer of tape and laboratory grade parafilm. The pump rate was set to 0.2 mm s^{-1}. The connected test structure was placed on the heated petri dish and the syringe pump was switched on as soon as the membrane liquified. The whole process was recorded on video.

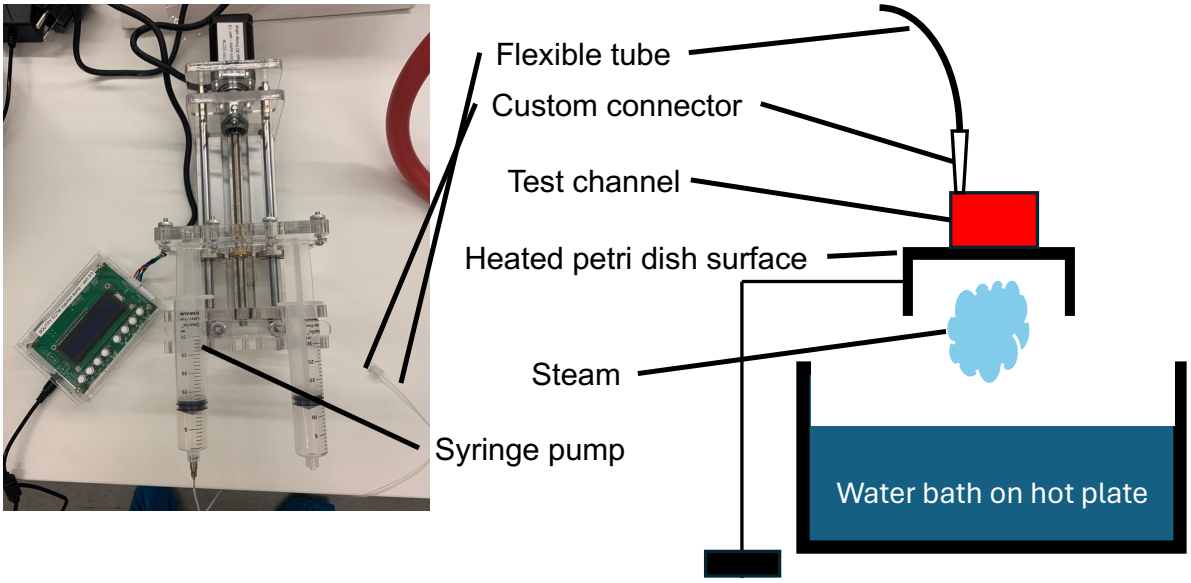

Figure 3.14: Experimental set-up for a proof-of-concept experiment for evacuating the membrane with air flow. The surface on which the test channel is placed is heated by the steam of the evaporating water on a hot plate. The air flow was generated with a syringe pump that was connected to the inlet of the membrane channel of the test structure.

4

Results

In this chapter, the results of the experiments described in Chap. 3 are presented. Following the same structure as the previous chapter, first the results concerning the OoC-platform and then detailed outcomes of the biodegradable membrane are presented. This chapter closes with the results from the experiments conducted to fuse these two lines of experiments, the integration and evacuation of the membrane.

4.1. OoC-platform for Co-culturing of Brain Organoid and Vascular Network

4.1.1. Fabrication

The chip was fabricated successfully with the DLP printer Asiga Max X27. A print was evaluated as successful when all design features were fabricated properly, and the resulting physical object matched the defined coordinates of 3D-model. Overall, the fabrication process repeatably exploited the benefits of additive manufacturing. Fig. 4.1 shows the chip as-printed and still attached to the build platform. The printer fabricated one chip consisting of three multi-cell culture platforms with seamless connection. The fabrication time without post-processing was less than 2 h.

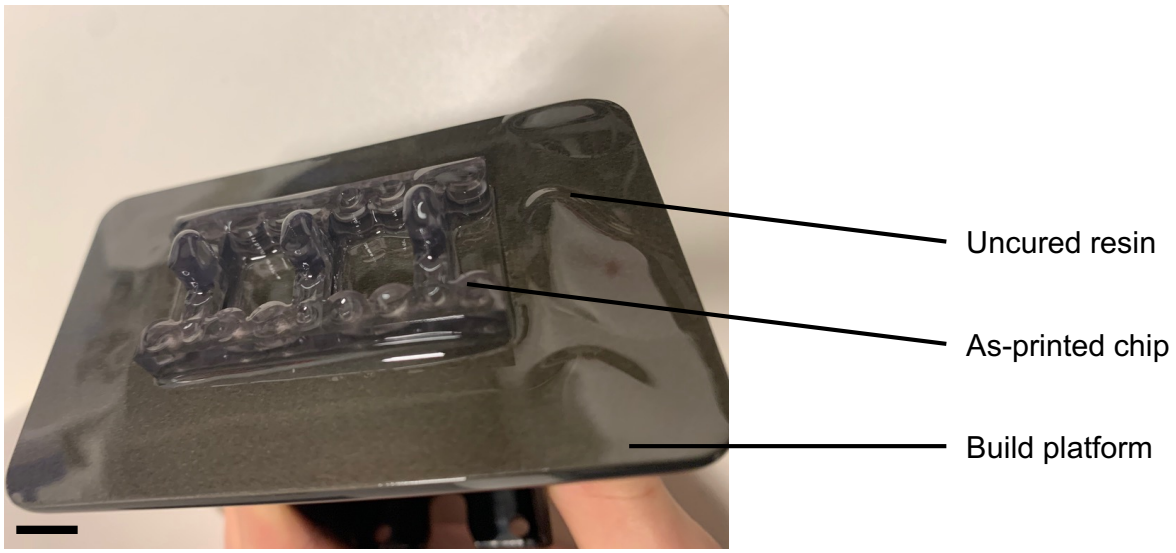

Figure 4.1: Resulting build from printing the chip with the Asiga Max X27. The device sticked to the build platform and was covered in uncured resin. Scale bar is 10 mm.

Table 4.1: Division of part in vertical direction in ranges with equal Z-resolution. The features in the ranges require different Z-resolution.

Range [mm]	**Part Features** [-]	**Demand*** [-]	**Layer Thickness** [µm]
0.000 - 0.030	Burn-in	high	10
0.030 - 0.050	Bottom plate	high	10
0.050 - 0.300	Microfluidic channel	high	10
0.300 - 5.020	In-/outlet	medium	50
5.020 - 11.830	Well	low	100

* Of spatial accuracy and smoothness, compared to other features.

The printing and material settings were mostly inherited from the default values of the specific material data file. A so-called burn-in range was added to the design prior to printing. This range comprised 3 layers of 0.010 mm thickness with maximum illumination intensity. This guaranteed that the part was well attached to the build platform throughout the whole print. Since this added a total 0.030 mm of height to the bottom, the 3D-model was adapted accordingly. To optimise the printing quality against printing time, the part was divided in different ranges along the vertical axes, allocating a dedicated layer thickness for each range. The layer thickness was matched with the required accuracy and smoothness in the different ranges. The ranges, corresponding features and selected layer height are presented in Tab. 4.1.

Post-processing

A dedicated post-processing workflow was developed to reliably remove all toxic monomers from the chip surface and guarantee the propriety of the microfluidic elements. The print head was dismounted from the machine and the part was carefully lifted off from the building platform with a metal scratch. To clean the part from the residual resin, it was cleaned in an ultrasonic IPA bath at room temperature for 10 min. Afterwards, it was immersed in IPA for 30 min to make sure the alcohol reached all channels as well as the surfaces of the pillars. After immersion, the part was flushed with DI-water to remove the IPA from the cavities. The channels were repeatedly flushed with compressed air to remove any residual components. The post-processing of the chip was concluded with UV-curing. In this process all uncured surface monomers were eliminated. To reach a biocompatible device, all polymer chains must be crosslinked. The device flashes the chamber with short pulses of UV light. The process was repeated three times for 2000 pulses in an N_2-rich environment. The inert environment enhanced the polymerisation on the surface. In addition, it reduced heat build-up. The workflow is summarised in the following list:

- Dismount part from print head with metal slider. Carefully lift one edge of the part and allow air to flow under and release the part.
- Clean part from residual resin in ultrasonic bath for 10 min in IPA at room temperature.
- Fully immerse part in IPA for 30 min to make sure all channels and hidden surfaces are reached.
- Flush channels with IPA, DI-water and compressed air until all structures are clear of liquid resin. Use microscope to access grade of cleanness, if necessary.
- UV-curing of part in UV-flash-device. Maximum 2000 (200 s) flashes in one step to avoid overheating of part. Add nitrogen gas to the chamber to enhance curing of surface molecules.

Fabrication Errors

While the proposed fabrication and post-processing method had a very high yield in terms of successfully printed OoC-platforms, some fabrication errors occurred that are described hereafter together with the methods put in place to avoid them.

The observed errors can be divided by their origin during the process into printing errors and post-processing errors. Printing errors caused the abortion of to the printing process. In few cases, the

machine could not detect the distance between the build platform and the bottom membrane of the resin vat. To avoid destruction of the machine, it automatically aborted the current print. In one fabrication run, the printed layers detached from the build plate and perished in the resin vat. The addition of the burn-in range avoided this error, as well as proper cleaning of the build platform.

Typical manifestations of errors are presented in Fig. 4.2. Insufficient cleaning of the channels prior to the UV-curing resulted in obstructed channels or avoided free standing pillars. The removal of the part from the build plate introduced a small defect where the metal scraper was introduced. The application of too strong pressure of compressed air created a hole in the bottom layer of the chip making that sample dysfunctional. Post-processing errors could be mitigated by following the workflow elaborated above.

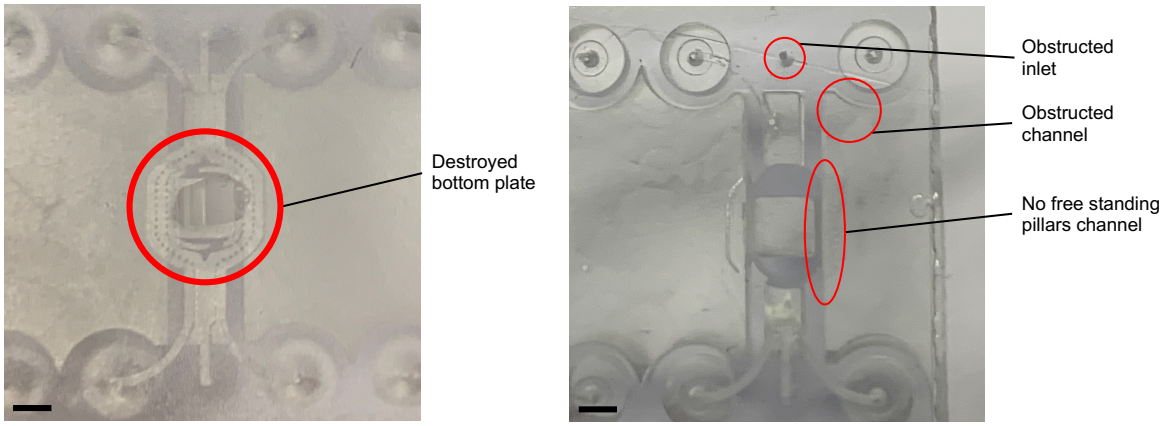

Figure 4.2: Different post-processing errors that nurtured the development of the post-processing workflow. Scale bar is 2 mm. (**a**:) Observed post-processing error resulting from too high pressure during cleaning with compressed air. (**b**): The ”invisible” channels and pillars were fabricated correctly. Residual resin in the channel consumed the structures impeding physical edges to be visible.

The occurrence of fabrication errors at the end of the master project was negligible, creating a nearly 100 % yield with the established vertical ranges for adapted layer thickness and the post-processing workflow.

4.1.2. Transparency of Bottom Plate

The transparency of the fabricated chips was investigated with optical inspection under the microscope. The visibility of micropillars and channels was qualitatively compared before and after the additional post-processing step described in Sec. 3.1.4. The transparency of the bottom plate was successfully increased. The edges of micropillars became clearly visible as well as the channels. Images taken from the same chip before and after the processing are shown in Fig. 4.3.

4.1.3. Dimensional Accuracy of 3D-printing Process

The accuracy of the printed chips was investigated with an optical microscope and the images were analysed with the DinoXcope software. The dimensions considered were the pillar size of the media channel in X- and Y-direction (long edge) and the inlet diameter for both media and gel channel. The outer dimensions of the chip were recorded as well. The large-scale dimensions of the printed chips matched the defined lengths in the 3D-model in all cases. The inlet diameter on channel height reached a good accuracy for both channels. The width of the micropillars satisfied the required dimensions with an average percentage error of 1.19 % (σ = 0.59 %) over 14 arbitrary selected elements distributed over 5 different chips.

The measurement results of the long edge of the pillars exhibited an average feature size of 284.78 µm (σ = 20.27 µm, target: 300 µm) over 18 arbitrary selected elements. The target values as well as the real average for the four different structures are summarised in Tab. 4.2.

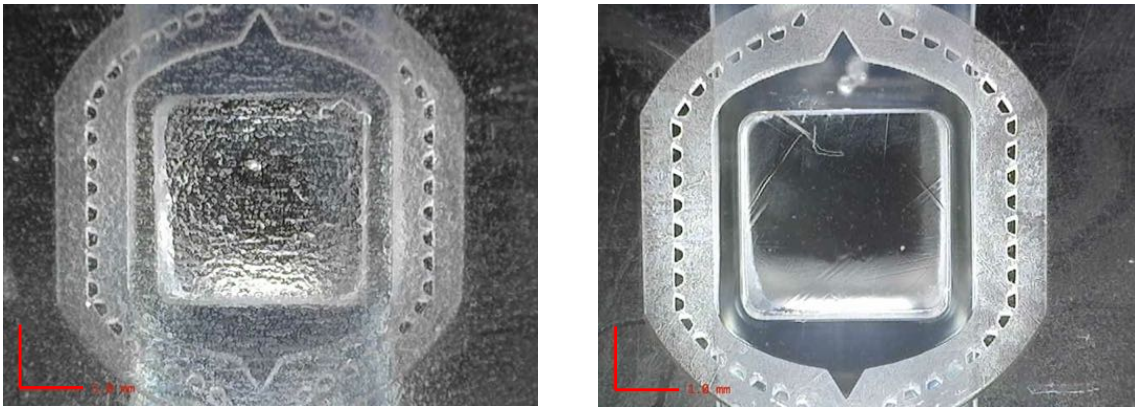

(a) (b)

Figure 4.3: Optical microscope images of the chip before and after transparency treatment. Scale bar is 1 mm. (**a**): Optical microscope image of bottom face of chip the before the transparency treatment. (**b**): Optical microscope image of bottom face of the chip after the transparency treatment.

Table 4.2: Obtained dimensional accuracy of microscale features in 3D-printed chip.

Structure	**Target Value** [µm]	**Real Value*** [µm]	**Percentage Error*** [%]	**Samples**
Pillar (X)	150	150.78 {1.88}	1.19 {0.59}	14
Pillar (Y)	300	284.78 {20.27}	5.15 {6.69}	18
Media Inlet	250	260.2 {13.44}	5.2 {3.9}	5
Gel Inlet	250	266 {15.52}	6.4 {6.2}	3

* Standard deviation in braces over the number of samples indicated in the table.

4.1.4. Biocompatibility of Selected Material

The biocompatibility of the chip was tested by direct application of the as-manufactured chip. The chip in the configuration ”single-culture” was sent to both collaborating groups. The chips were used to culture the cells as described in Sec. 2.3. In this way, not only the biocompatibility but also the level of integration of the design into the biologists’ workflows was tested.

The cell cultures were able to survive on the chip proving that the material manufactured in the here presented manner is biocompatible. In comparison to the established culture environments, the yield on the 3D-printed chip was lower. The handling of the chip was successfully integrated into the existing workflow. For the vasculature, the formation of network was monitored after 7 days culture period and captured with an optical microscope by the colleague. The result is presented in Fig. 4.4.

No absolute values for the cell density on the herein fabricated OoC compared to the established culture platforms of the cell protocols were obtained. However, the collaborators indicated a slightly less expressed cell density and complexity of cell structures on the 3D-printed chip for both cell cultures.

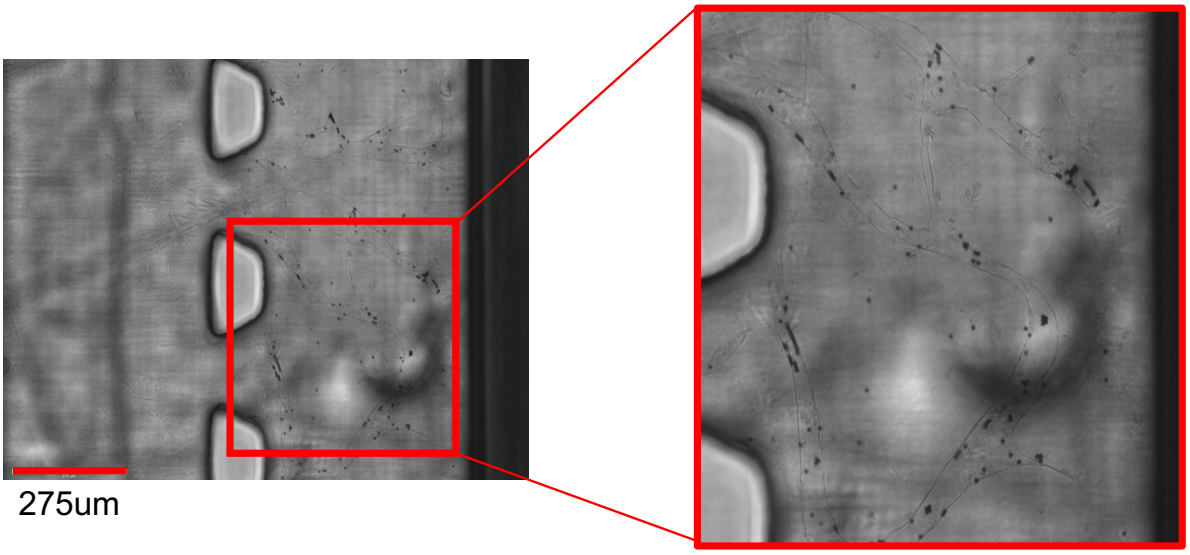

Figure 4.4: Formation of vascular network on herein developed 3D-printed OoC-platform. Optical microscopy image of sprouting vascular network. Start point of the growth from interface with the media channel through the pillar array. Scale bar is 275 µm.

4.2. Biodegradable Membrane for OoC-platform

The goal of the material characterisation was to determine the ideal membrane composition. The optimal composition is characterised by the melting point, the selected particle, and the particle volume fraction. The melting point was determined with the DSC analysis and the application of the CEM43 model. The particle choice was supported by the magnetisation measurements and the inductive heating experiments yielded the best particle concentration with respect to the integration of the membrane on-chip. The results of the different experiments are presented in this section.

4.2.1. Material Selection

Next to the requirements of the membrane in terms of biodegradability and functionality, the composite must exhibit a melting point in the physiological tolerable range to comply with the strict limits in contact with the cells. To obtain an informed target value for the maximum allowed temperature and time period, the CEM43 model was applied. According to [122], the blood-brain-barrier (BBB) features a value of CEM43 = 2 min. To explain, if the BBB is exposed to 43°C longer than 2 min, the tissue risks taking considerable damage. Fig. 4.5 shows the iso-value line for CEM43 = 2 min according to the model introduced in Eq. 3.1. Since no concrete value for brain organoids is reported in the literature, the value of the related BBB tissue type was used as reference.

4.2.2. Fabrication

The established mixing process of the membrane is a straightforward process that yielded samples in an effective and repeatable manner. The equipment used for this were readily available in the lab and simple to operate.

The first step was weighing the components of the composite. The wax matrix itself consisted of two different components, bayberry wax and lanolin. At room temperature, lanolin has a soft, creamy texture. This consistency made it difficult to extract it from the container which was amplified by its stickiness. As a consequence, weighing this component in a separate beaker and adding it in the right quantity to the mixing vial was not possible because fractions of the lanolin would stick to the surface and remain in the measurement cup. In order to extract the right amount of lanolin, two plastic spatulas were used by using one spatula to scrape off small quantities of lanolin from the other into the mixing container. The bayberry wax was provided in pellets which facilitated the measurement of the correct mass. The melt-mixing of the two waxes was straight forward and did not add struggles to the process. The two waxes were melted in the same vial until both phases completely liquefied. Mixing with the

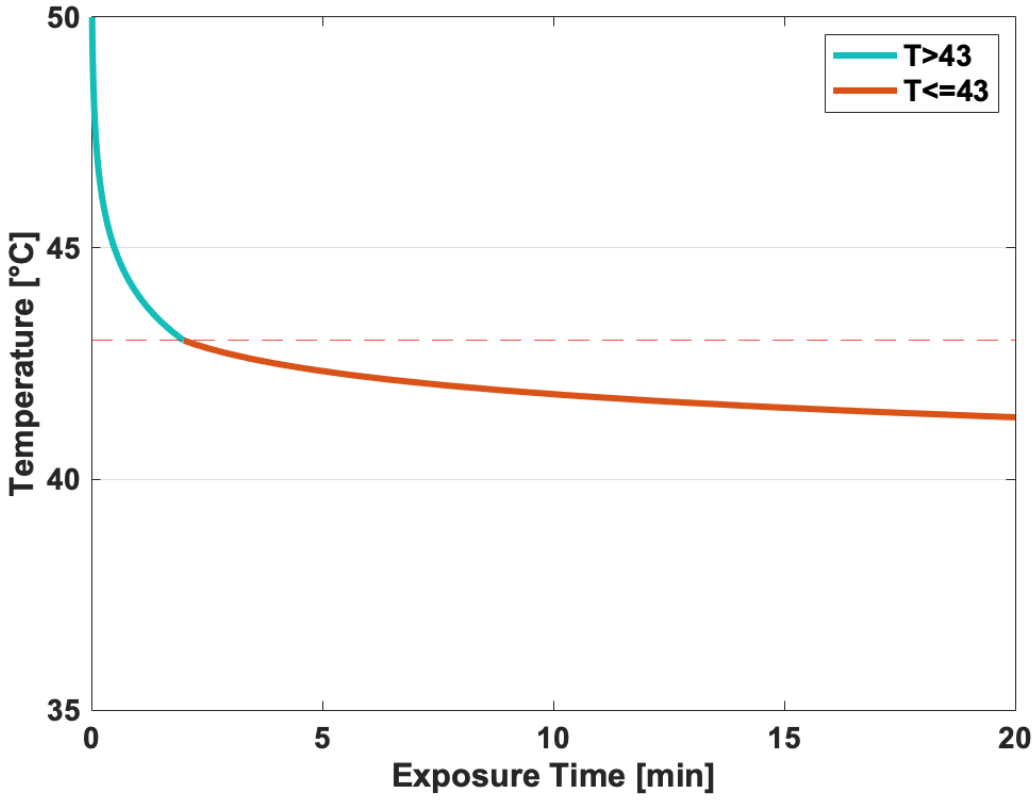

Figure 4.5: CEM43 values plotted for value of CEM43 = 2 min. All exposure time-temperature pairs that fall on that line cause the same thermal damage to the tissue, according to the model.

device described in Section 3.2.2 was straight forward and yielded homogeneous matrices, judged by the uniform colour of the mixed matrix.

In the second step, the composite was created from the matrix and the particles. Similar to the process described above, the components first were weighed with a scale. The retraction of the particles from the container with a spatula was uncomplicated but required caution to avoid spilling of the material. Melt-mixing of the matrix and particles presented challenges in terms of reaching homogeneous mixtures. Combining the particles with the matrix as solid phase caused particle sedimentation and clustering prior to mixing. Therefore, the matrix was first liquified and subsequently the particles were added. In that manner, the particles dispersed in the matrix with gravity in the liquid phase matrix. The mixing with the vortex mixer produced good dispersion of the particles and homogeneous composites with CIP particles in terms of no phase separation could be observed with visual inspection. For composites fabricated with magnetite, a clear separation of the black particles and the yellow matrix phase could be observed after intense mixing. This indicates a particle agglomeration leading to weaker particle dispersion. The results of weighing the components and composites in terms of the percentage error of targeted/real mass are presented in Tab. 4.3.

4.2.3. Thermal Behaviour of the Membrane

The thermal behaviour of the membrane was investigated with DSC-measurements. The main focus was to determine the melting point of the matrix in dependence of the matrix composition. The DSC-curve plots the normalised heat flow Q over the temperature and was analysed to determine important thermal parameters of the matrix. All samples had a similar mass around 20 mg. The first cycle was used to eliminate the thermal history of the material, the second cycle was used for analysis.

Table 4.3: Percentage error of weighing the different components before mixing. The values result from the comparison of the intended mass to the real mass. The compound fractions of bayberry wax and particles for matrix and composite, respectively, are calculated with the real mass values.

Component	**ϵ of mass^a in %**	**ϵ of volume fraction^b in %**
Lanolin	0.25 {0.18}†	0.304 {0.501}†
Bayberry Wax	0.31 {0.53}†	
CIP	0.74 {0.73}‡	2.070 {2.605}‡
Matrix	2.06 {3.20}‡	

^{a} of single components, ^{b} of BBW and CIP, respectively. † Average of 9 samples, ‡ average of 7 samples, standard deviation in braces.

Fig. 4.6 depicts the normalised heat flow of the second heating for all matrix samples. The general trend of increasing melting point, melting onset point, and enthalpy of fusion was observed for increasing BBW fraction. The highest melting point was determined for the pure BBW sample at 51.58°C. The lowest melting point was featured for the matrix with 10 vol.-% BBW at 29.65°C. With respect to the application of the matrix as membrane integrated on a OoC-platform, the matrix with 40 vol.-% yielded the most favourable properties with a melting point at 44.29 °C (hereafter referred to as M04). Multiple endothermic peaks were recorded for all samples. The determined thermal properties for the different samples are summarised in Tab. 4.4.

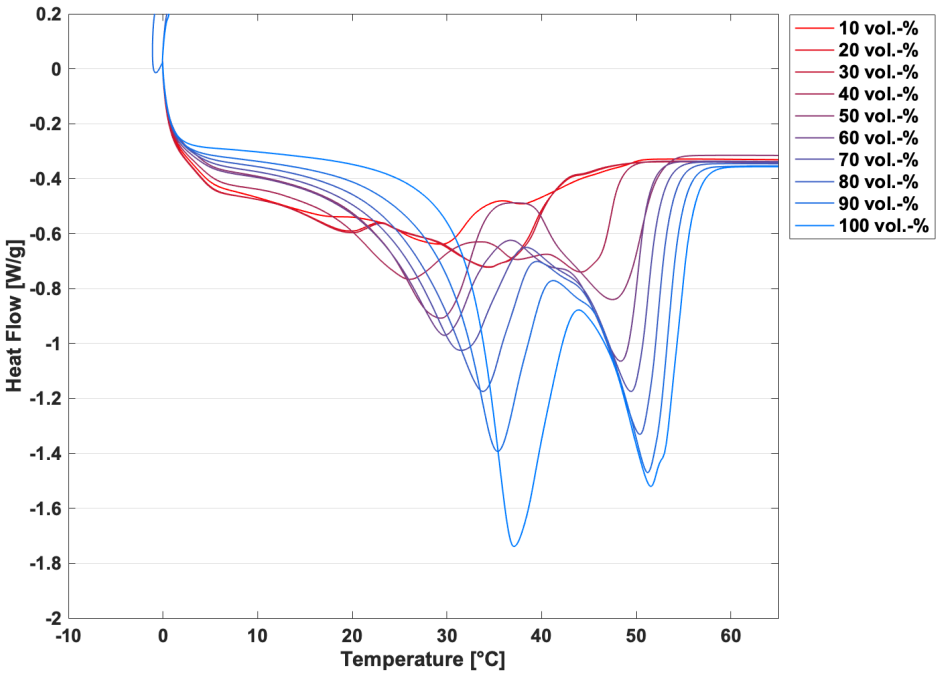

Figure 4.6: DSC-curve for all matrix compositions of the second heating cycle. The normalised heat flow was investigated over the temperature range in dependence of the BBW volume percentage in the composite. The fraction increases with the colour gradient from red to blue.

Fig. 4.7 depicts the graphical analysis using the example of the matrix M04 enriched with 10 vol.-% CIP particles. The integration limits to calculate the enthalpy of fusion were selected manually. Additionally, the heat capacity of the sample is depicted. The heat capacity increased in the melting range of the sample with an overlapping peak at 43.78°C. The addition of particles reduced the melting point of the material compared to the empty matrix by 0.18°C. The enthalpy of fusion was reduced to 32.11 $\mathrm{J\,g^{-1}}$. Due to the optimal melting point of this composite, the matrix M04 was chosen for the following

Table 4.4: Thermal parameters of the different matrix compositions obtained from the DSC analysis.

BBW Fraction [vol.-%]	**Melting Point** [°C]	**Onset Temperature** [°C]	**Fusion Enthalpy** [J/g]
10	29.65	15.28	32.9
20	34.57	19.11	38.33
30	34.63	20.18	38.33
40	44.29	15.14	57.45
50	47.54	19.33	71.14
60	48.33	20.69	79.13
70	49.42	22.37	97.81
80	50.38	24.65	109.3
90	51.19	28.27	124.2
100	51.58	31.75	132.6
M04 + CIP	44.11	15.33	32.11

investigations with the inductive heating experiment and membrane injection.

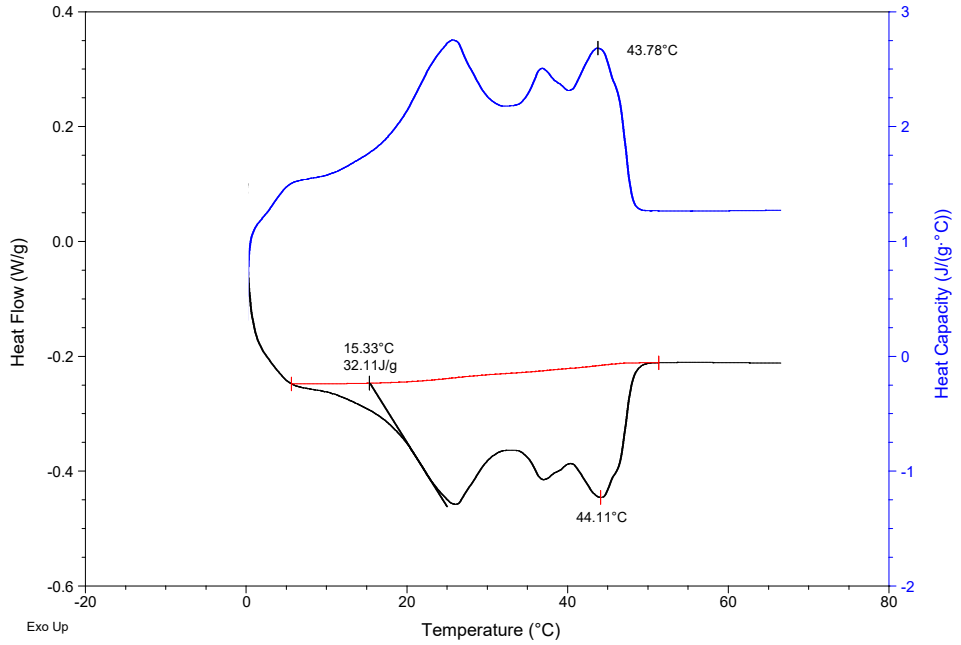

Figure 4.7: Graphical analysis of the DSC-curve for the sample M04_A10. The melting point was determined at the endothermic peak with the highest temperature value. The heat of fusion was calculated as the area of the peak to the base line. The blue line indicates the heat capacity over the temperature.

The heat capacity of the composite was extracted from experimental data for calculations with the inductive heating experiment. As can be seen in Fig. 4.7, the parameter was not constant but changed over temperature. Especially in the temperature range of the intended application around the melting point of the composite, a strong variation was detected. Therefore, the heat capacity of the sample in the region of interest was estimated as the average of the values in the range from 37°C to 45°C. Therefore, the estimated value for the heat capacity of the sample W04_A10 is c_p = 2.485 J/g/°C.

4.2.4. Magnetisation of Particles

SQUID measurements were conducted to assess the magnetisation and hysteresis loss of the two materials carbonyl iron powder and iron oxide. The results of the experiment are depicted in Fig. 4.8. CIP featured a larger hysteresis loop area of 5.43 compared to 1.93 for magnetite. CIP particles showed a higher saturation magnetisation M_s and a lower remnant magnetisation M_r than magnetite particles.

The values of the magnetic parameters are presented in Tab. 4.5. The coercive field is qualitatively shown in the inset of Fig. 4.8. The value was found to be significantly higher for magnetite than for CIP.

Table 4.5: Magnetic properties obtained from the SQUID measurements in the range of -1-1 T at 310 K.

	$\mathbf{M}_s$ [A m^2/kg]	$\mathbf{M}_r$ [A m^2/kg]	**Hysteresis Loop** [-]
CIP	192.7	0.34	5.43
Magnetite	88.3	9.79	1.93

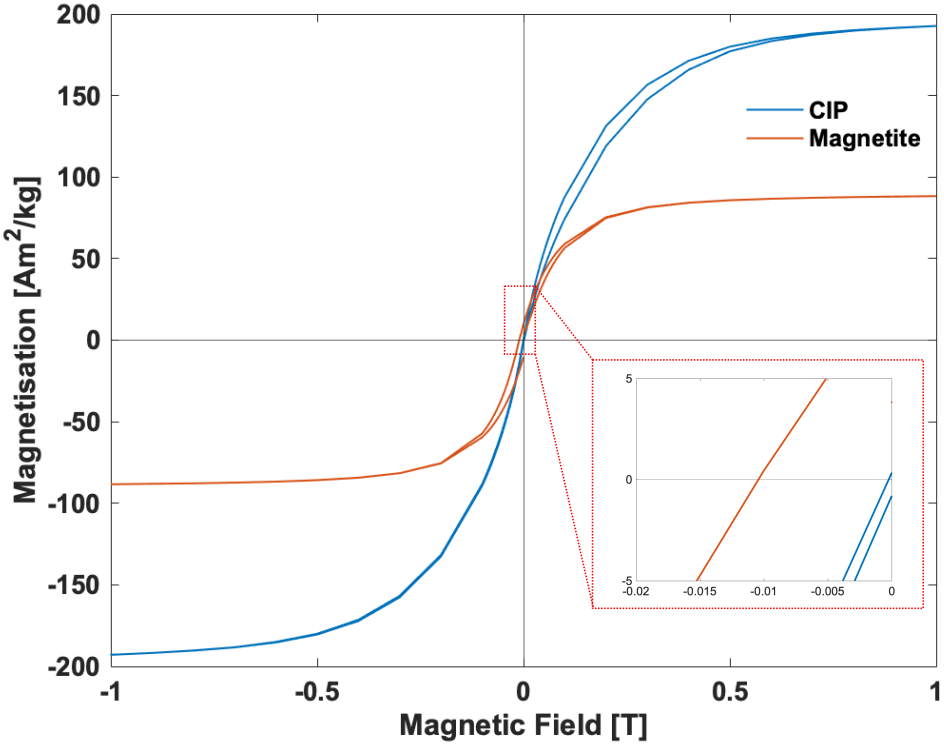

Figure 4.8: Magnetisation of CIP and magnetite particles from SQUID measurements. The inset shows the intersection of the curve with the x-axis, indicating the coercive field of the samples.

Based on the results obtained from the characterisation of the magnetic particles, CIP was selected as favourable active component for the membrane material. The larger hysteresis loop was expected to increase heating efficiency with the inductive heating, whereas the lower remnant magnetisation facilitates composite mixing. All composites fabricated for further experiments were enriched with CIP.

4.2.5. Inductive Heating Experiment

The inductive heating experiment was conducted to assess the heating behaviour of the composite in dependence of the particle fraction (4 values) and the applied field strength (3 values). In total, 12 different experimental conditions were investigated. All recordings included a temperature equilibration prior to the recording and an exposure time and between-exposure time depending on the field strength. Due to the large variety in heating rate of the samples on the one hand, and machine safety constrains on the other hand, no consistent exposure profile could be defined for all experimental conditions. Since a linear dependence of temperature and time was expected, the different exposure times do not influence the results.

The baseline of temperature drift was investigated through the inclusion of the control sample without particles. The time-temperature curve for the empty matrix for three different field strengths is plotted in Fig. 4.9. The red lines indicate activation and deactivation of the magnetic field, respectively. It becomes apparent that the application of the AMF did not have an influence on the temperature in

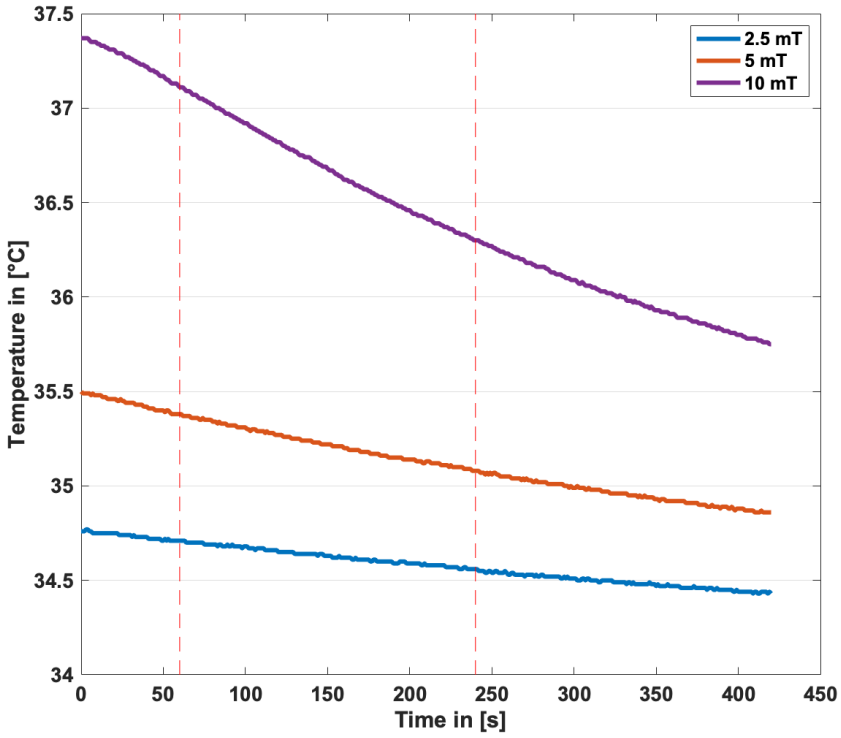

Figure 4.9: Temperature drift of the empty matrix at three different AMF values. The dotted red lines indicate the activation and deactivation of the magnetic field.

the sample. The temperature decreased independent of the presence of an AMF. The three trend lines suggest that the cooling rate was higher at higher temperatures. The resulting cooling rates are presented in Tab. 4.6.

Table 4.6: Base line cooling rates obtained from the AMF exposure of the empty matrix in different initial ranges.

Experimental Condition	**Cooling Rate** [°C/min]	**Temperature Range** [°C]	**Sample Size**
$IH_{00\_2.5}$	-0.047 {-}	34.3 - 34.7	1
IH_{00_5}	-0.091 {-}	34.8 - 35.5	1
IH_{00_10}	-0.231 {-}	35.7 - 37.3	1

The raw data obtained from the temperature measurements is plotted for the sample with 25 vol.-% at $B = 10$ mT in Fig. 4.10. The red lines indicate activation and deactivation of the magnetic field in alternation. The AMF exposure time was set to 18 s and the cool down phase in between exposures was 10 min. The peak temperature was 54.28 °C at the end of exposure phase 2. This is at the same time the highest temperature recorded in all measurements. While the cooling of the sample was non-linear, the temperature increase of all samples was linear. Therefore, the heating rate of all experimental conditions was calculated with Eq. 3.7. The strongest field in combination with the highest particle concentration yielded the steepest temperature increase. The results of all experimental conditions are given in Tab. 4.7.

The efficiency of heating of the particles in the different samples was assessed with the specific loss power (see Eq. 3.8). The highest HR was determined for the experimental condition IH_{25_10} with an average value of 41.73°C min^{-1} with a standard deviation of 0.49°Cmin^{-1} over three samples. This experimental condition also featured the highest SLP value with 141.491 {1.684} W g^{-1}. The largest

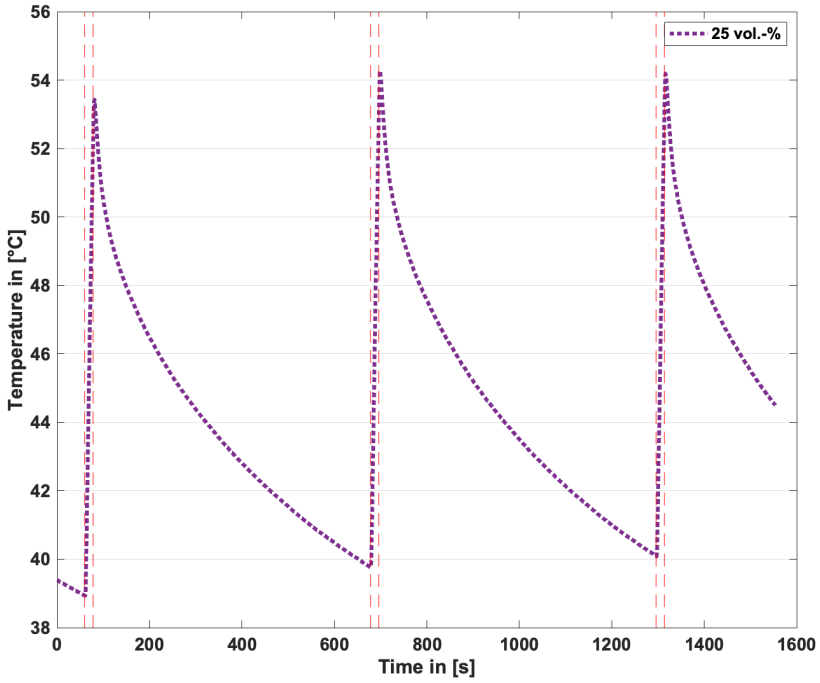

Figure 4.10: Raw data of the recording of sample IH_{25_10}. Measurement programmed to repeat three AMF exposure phases of 18 second with 10 min cooling time in between to re-establish the initial temperature.

variation of SLP was detected for the experimental condition IH_{10_10}. For both parameters, HR and SLP, the following trend was observed:

- the higher the particle fraction, the higher the parameter, and
- the stronger the magnetic field, the higher the parameter.

Table 4.7: Heating rate and specific loss power of composites subjected to different field strengths.

Experimental Condition	Heating Rate* [°C/min]	SLP* [W/g]	Sample Size
$IH_{03\_2.5}$	-0.19 {-}	-2.229 {-}	1
IH_{03_5}	-0.08 {-}	-0.985 {-}	1
IH_{03_10}	2.66 {0.05}	31.789 {0.638}	3
$IH_{10\_2.5}$	-0.05 {-}	-0.251 {-}	1
IH_{10_5}	1.70 {0.01}	8.881 {0.053}	3
IH_{10_10}	14.37 {4.71}	74.879 {24.51}	3
$IH_{25\_2.5}$	0.15 {0.003}	0.503 {0.012}	3
IH_{25_5}	4.81 {0.33}	16.314 {1.119}	3
IH_{25_10}	41.73 {0.49}	141.491 {1.684}	3

* Standard deviation in braces.

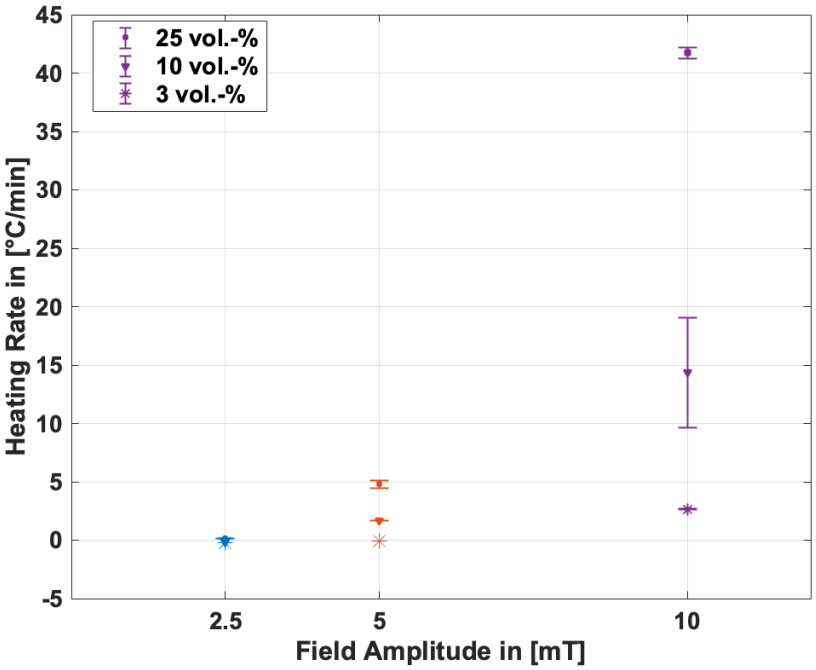

Figure 4.11: Heating rate of the different experimental conditions in dependence of field strength (colour) and particle concentration (marker shape). The marker indicates the average value over three measurements and the error bars depict the standard deviation.

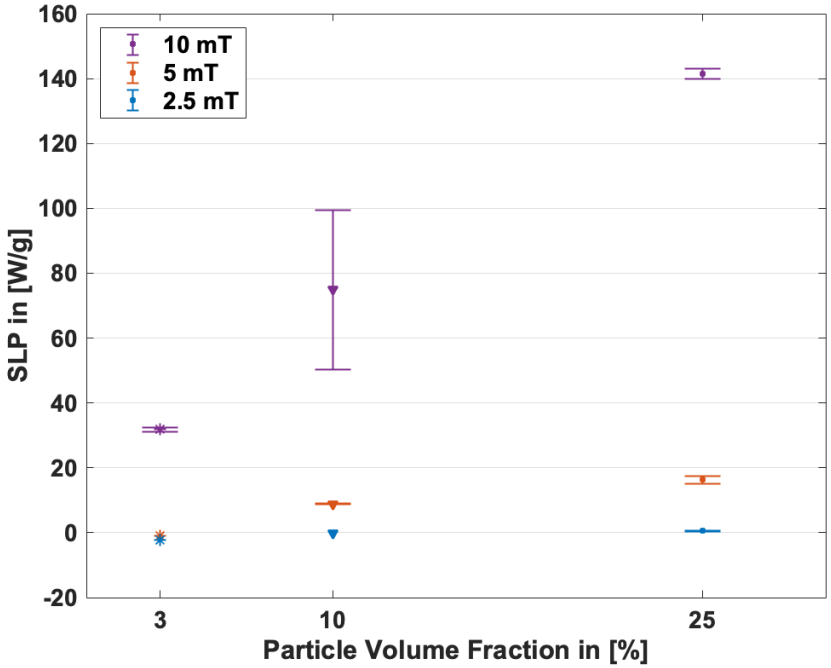

Figure 4.12: Obtained specific loss power values for the 9 different experimental conditions that included particles over the particle volume fraction. The marker represents the average value for repeated measurements, the error bar indicates the standard deviation. The marker colour indicates the field strength.

4.3. Integration of Biodegradable Membrane to OoC-platform

The membrane integration was realised with gravity induced flow of the material into the membrane channel. In a set of experiments and numerical simulations, the optimal pillar shape and pitch was determined. In a proof-of-concept experiment it could be shown that the membrane can be evacuated from the channel upon application of moderate pressure without leaking to the cell compartments.

4.3.1. Injection of Membrane

Experimental Results

In the experiments, the material was loaded to the inlet storage and liquified in the oven at 50°C. The composite melted in 6-10 min. Gravity of the inserted material was sufficient to overcome the hydraulic resistance of the microfluidic channel, hence the liquid composite filled the channel. The real temperature had a strong effect on the fluid behaviour of the composite. A variation of 2-3°C considerably influenced the viscosity and hence the surface tension. The temperature of the immediate chip placement was measured with an additional temperature probe. In this way, the exact conditions could be monitored to repeat the experiment under the same conditions.

The capability to confine the material in the membrane channel was assessed via optical inspection of the distribution of the black material. The 12 experimental conditions were repeated with 5 identical test structures resulting in a base sample size of 10 channels per configuration. The most promising [geometry, gap size] pairs were identified as [stadium (D25), 30 µm], [stadium (D25), 50 µm], and [tapered, 30 µm]. A second test structure was designed and printed yielding another 8 channels per configuration. One channel pair of [tapered, 30 µm] was destroyed during the post-processing of the 3D-printed object, reducing the sample size for this condition to 6. The yield for both tests is presented in Tab. 4.8. The yield of the second test structure isolated was 75 % percent for [stadium (D25), 30 µm]. Therefore, the experimental approach gave rise to the assumption that the optimal parameter combination was a stadium geometry (semicircle diameter 0.25 mm) with a pillar gap of 30 µm.

Table 4.8: Yield of successful confinement of composite in the membrane channel with gravity driven injection.

Shape	Sample Size			Yield [%]*		
	30 µm	50 µm	100 µm	30 µm	50 µm	100 µm
Tapered	10 (6)	10	10	20 (33)	40	0
Rectangular	10	10	10	70	20	10
Stadium (D15)	10	10	10	10	20	0
Stadium (D25)	10 (8)	10 (8)	10	30 (75)	30 (37.5)	0

* Yield of second test structure in brackets.

Numerical Results

The simulation conducted in COMSOL Multiphysics 6.1 was analysed with respect to the fluid velocity. The dynamic viscosity was estimated based on the experiment described in Sec. 3.3.1. From the video recording of the injection process, the time it took to fill the channel was 12 s (retrieval as in Fig. 4.15). With Eq. 3.12 an approximate value for the dynamic viscosity was obtained as $\eta = 59.2$ mPa at 43°C. Based on the previous results (Sec. 4.2.3, 4.2.4), the membrane material was composed of the matrix M04 and CIP particles with a volume fraction of 10 vol.-%. The average density of this composite was 1.648 g mL^{-1}.

The resulting fluid velocity of the simulations matched the flow rate obtained from the experimental investigations, indicating a sufficiently accurate estimation of the material properties and boundary conditions. The velocity profile of the experimental condition [tapered, 100 µm] is depicted in Fig. 4.13 by way of illustration. The distribution of the velocity indicated by the colour gradient showed a significant leakage of the fluid to the adjacent channel for that configuration.

The analysis of the fluid velocity alongside the line data set defined in Fig. 3.13b allowed the comparison of the different [geometry, gap size]-configurations with respect to confinement capability. Within the second variable, gap size, the leakage through the pillars increased with increasing gap size. The

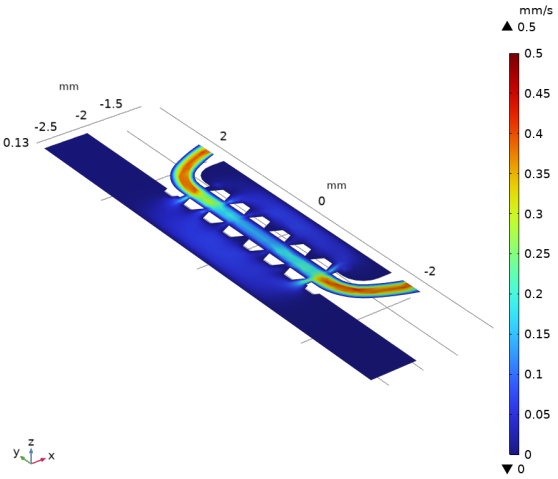

Figure 4.13: Fluid velocity profile as result of numerical analysis of injection process. The main velocity field remained within the confinement of the pillars. The light blue fields at the pillar gaps indicating leakage of the fluid through the pillar array.

largest velocity was simulated at the first pillar gap in the [rectangular, 100 µm]. The effect of the pillar geometry was strongest at low gap sizes. While for G = 100 µm all channels exhibited significant leakage in the same magnitude range, the fluid velocity featured higher variation for G = 30 µm depending on the geometry. The velocity profile alongside the line data set for the different gap sizes is presented in dependence of the pillar geometry in Fig. 4.14.

The velocity magnitudes graphed in Fig. 4.14 showcased peaks in periodical distance corresponding to the gap positions in the pillar array. For all configurations, the maximum peaks were observed at the first and last pillar gap. The lowest velocity values were simulated for [stadium (D25), 30 µm] and [rectangular, 30 µm] with a peak leakage below 0.02 mm s^{-1}.

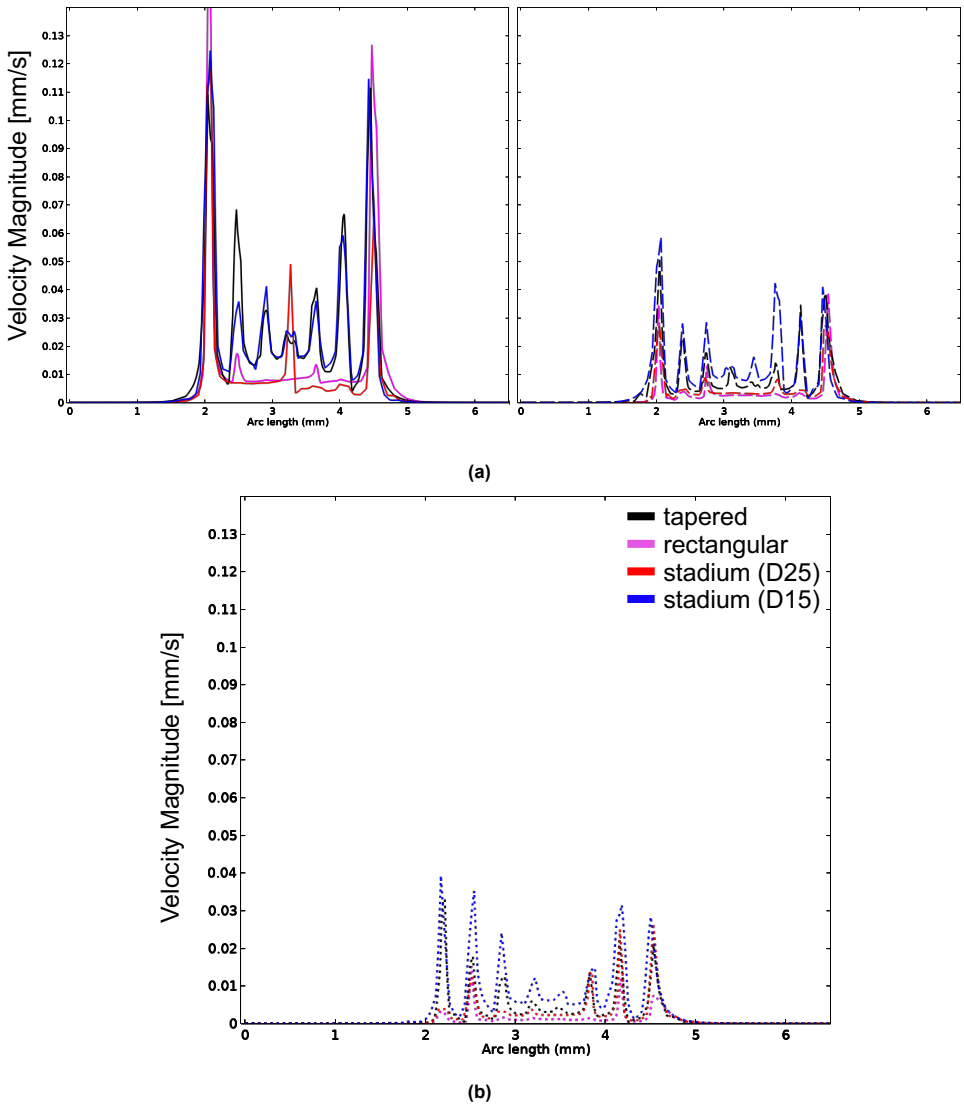

Figure 4.14: Simulations results of velocity leakage from membrane channel. (**a**): Simulation results for G = 100 µm (left) and G = 50 µm (right). (**b**): Simulation results for G = 30 µm.

4.3.2. Evacuation of Membrane

The membrane separates the cell culture compartments on the chip for a defined time period. In a two-step process, the matrix is first liquified via inductive heating and then pressured out with air. A proof-of-concept experiment for the second step was conducted and the results are presented hereafter. The analysis of the video recording indicated that the material was transported in the membrane channel upon pressure application with a syringe pump. No significant leakage to the adjacent channels was observed. In Fig. 4.15 the progress of the fluid front of the membrane at different time points of pump activation is depicted.

To evaluate whether the membrane in fact opened for cross talk between the two adjacent chambers, food dye dissolved in water was injected into the adjacent channels. Traces of the coloured liquid gave insights about the state of the membrane. The dye was injected in three different test structures with three different expected states: (1) open, no membrane injected, (2) closed, membrane injected, and (3) open, membrane injected and evacuated as depicted in Fig. 4.15. Condition (1) yielded immediate mixture of the two colours in the membrane channel and subsequently in the whole cavity. State (2) separated the two different liquids, and no mixing of the colours was observed. The division was stable for at least 5 days. In the time of this project, no systematic failure of the membrane in contact with

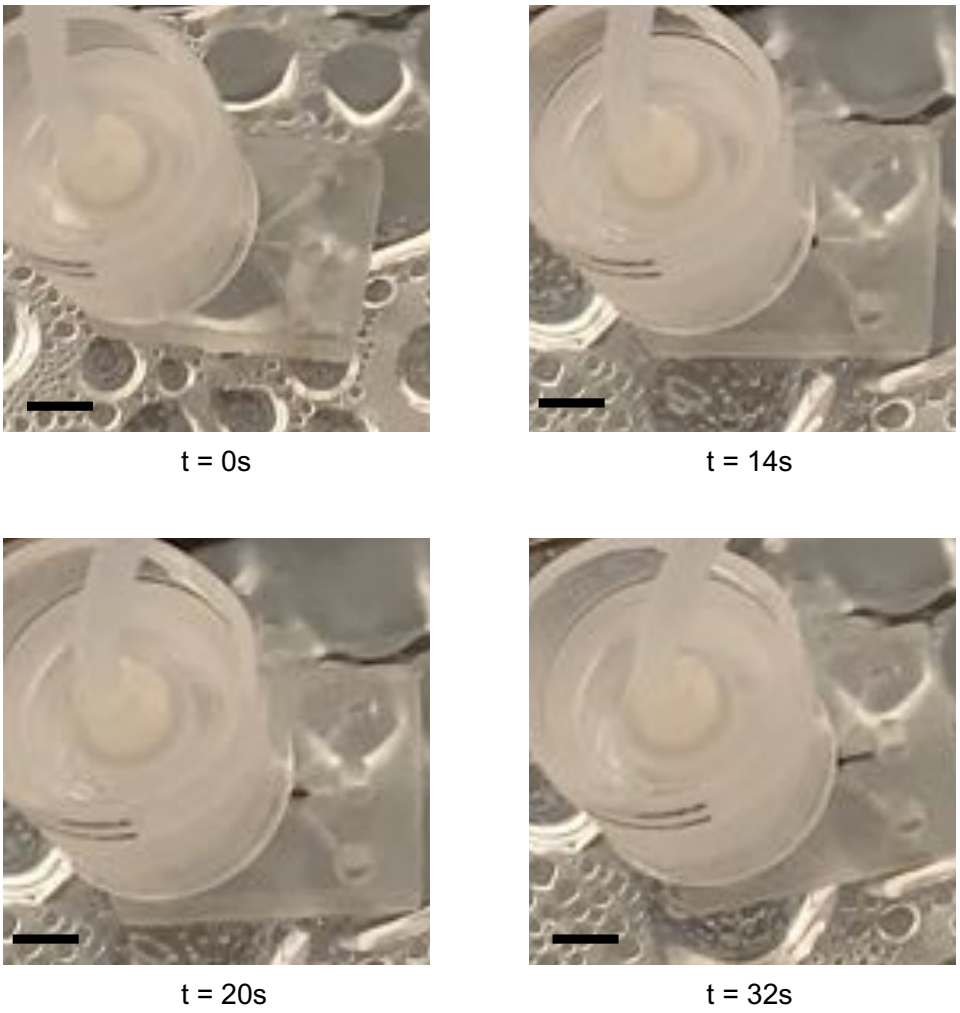

Figure 4.15: Video frames of the evacuation process at 0 s, 14 s, 20 s, and 32 s after pressure activation. Scale bar is 2 mm.

the water was observed. For the last case (3), no immediate cross chamber movement of the dye was apparent. The samples were allowed to rest at room temperature in horizontal position for 24 h. After that period, blue ink was spotted in the membrane channel. This gave rise to the expectation that the membrane state in fact switched to open and cross chamber transfer is possible. The test structures with injected dye of structure (2) and (3) are presented in Fig. 4.16.

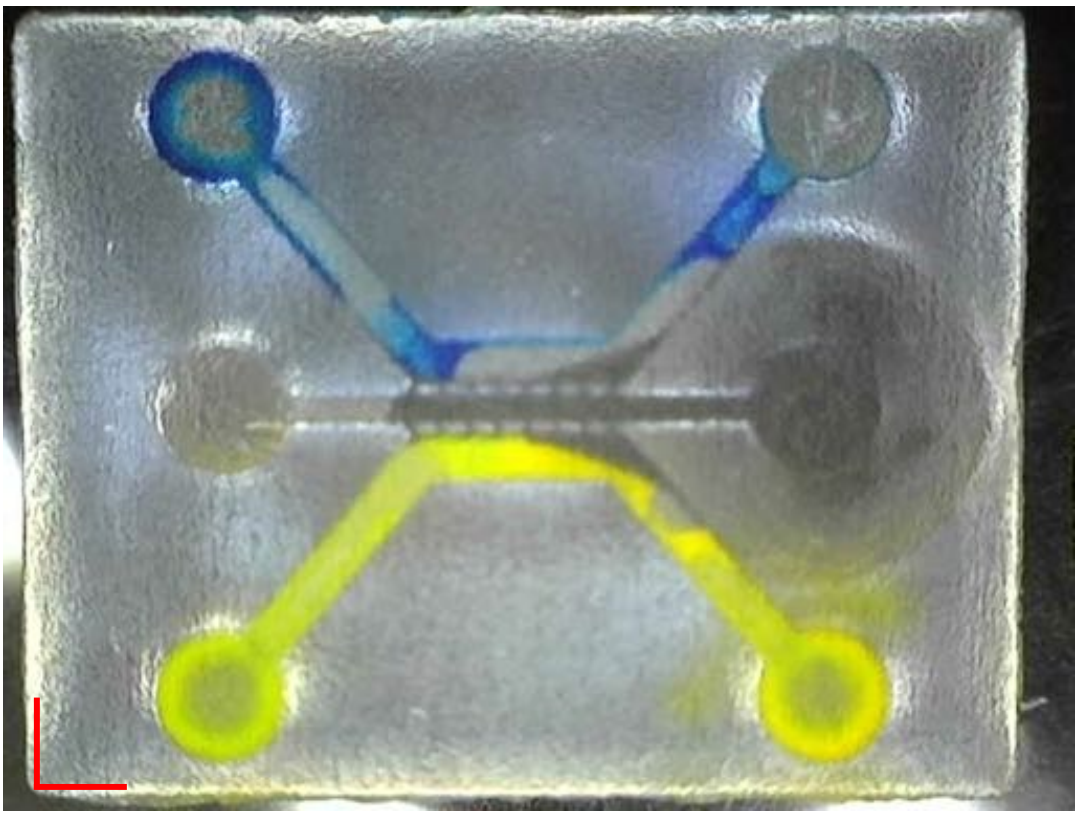

(a)

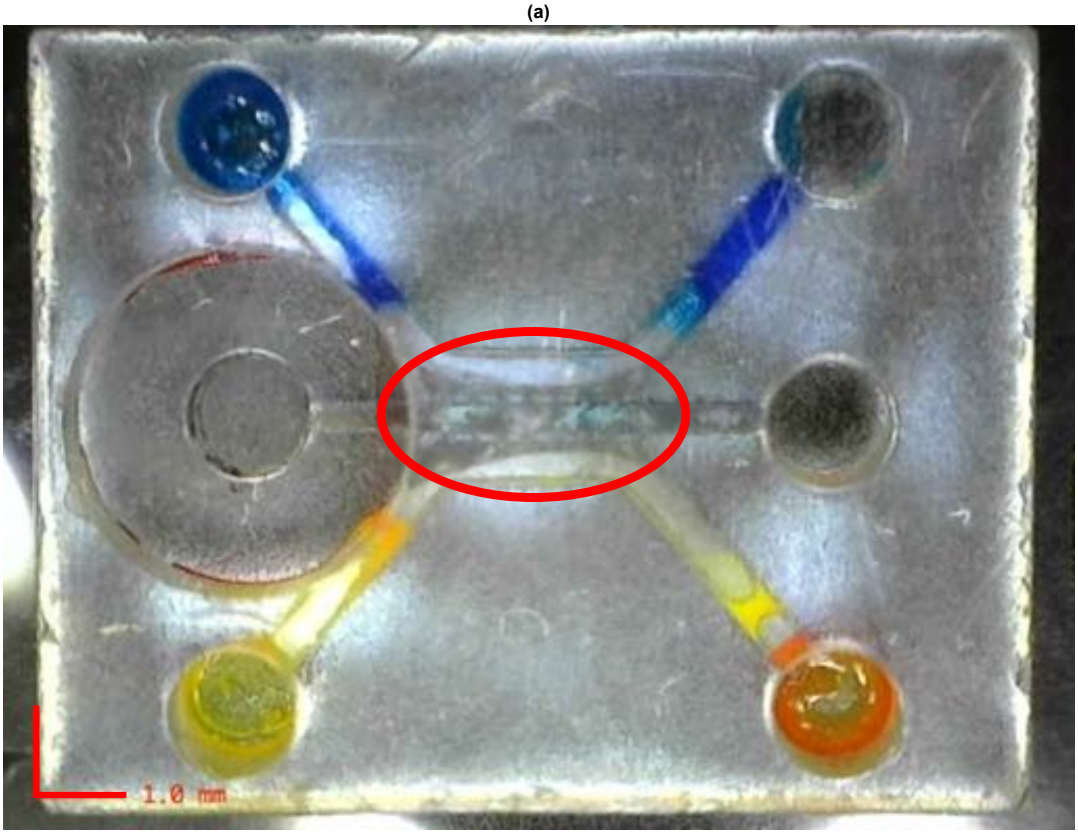

(b)

Figure 4.16: Comparison of the permeability of water through the membrane in (expected) closed and open stat. Scale bar is 1 mm and indicated as the red lines in the bottom left of each picture. (**a**): Coloured water injected into the flanking chambers with closed membrane. (**b**): Coloured water injected into the flanking chambers with opened membrane. Inside the red marker, light blue traces in the membrane channel.

5

Discussion and Future Recommendations

This section discusses the results presented in Sec. 4 in respect to the research goal to develop an Organ-on-Chip platform for the vascularisation of brain organoids. Recommendations for future efforts as well as possible follow-up research directions are given with the elaboration on the room of improvement for the presented results.

5.1. OoC-platform for Co-culturing of Brain Organoid and Vascular Network

The OoC-platform was fabricated using the additive manufacturing process digital light processing. This method benefited the design process of the chip. Since DLP proceeds layer-by-layer, the fabrication process imposes virtually no constraints on the design complexity. The intended microfluidic channels were printed with good resolution and in a time varying from 1.5 to 2 h. Another advantage was the single-step manufacturing from 3D-model to finished part. This allowed for an iterative prototyping approach, in which different structures and designs could be tested in a quick manner. The design freedom was exploited with the design of multiple micropillar arrays. These arrays were used as both: as fluid separating features between the media and gel channel and as confinement for the membrane channel. Since all structures were fabricated in a single manufacturing step, the critical components were directly bonded to each other eliminating the risk of cross compartment leakage.

Fabrication errors could be avoided by the development of a concise post-processing protocol. The percentage of failed prints due to machine errors was negligible. Overall, DLP was established as feasible and convenient method to fabricate the OoC-platform. Nonetheless, DLP introduced some limitations to the process. First of all, the transparency of the untreated part was deficient. Three major process-related sources for the reduction of transparency can be identified. First, the surface roughness of the print head was translated to the bottom surface of the chip. The irregularities on the surface scatter incoming light beams randomly which strongly effects the optical transparency. A counter measure was successfully established in this project by cross linking an additional layer of resin against the bottom surface while squeezed against a glass slide. This yielded optically smooth surfaces on the chip. This highly manual process was bearing the risk of introducing user variability and inconsistent part thicknesses. In future efforts, the build platform of the machine could be adapted. For example, a glass plate could be glued to the building platform to consistently create smooth bottom surfaces. Similar approaches have been discussed in Chap. 2 [28, 49].

A second possible source for reducing optical transparency is the resolution of the 3D-printer. The employed machine uses a digital micromirror device (DMD) with a resolution of 27 µm. While one layer is illuminated as a whole, the projected image of the layer is divided in pixels of that resolution. The

edges of the pixel potentially introduce small irregularities that aggravate imaging under the microscope. A possible solution is changing the orientation of the object on the build plate. In [123], Ortega et al. investigated the surface roughness of DLP-printed parts with 0°, 45°, and 90°orientation of the object and determined the third orientation as most favourable to reduce the surface roughness. The resolution in vertical direction can be controlled with the layer thickness. A Z-resolution of 10 µm is possible with the selected machine. However, in the presented design, this would introduce the need for support structures to the part because a horizontal orientation of the long organoid chamber would create large overhanging structures. The addition of support structures reduces the overall part quality as they penetrate the surface and would have to be removed mechanically after the printing process.

A third reason that can affect the transparency of the 3D-printed parts is smoothness of the membrane of the resin vat. The excessive use of the 3D-printer left scratches on the bottom of the tray that slightly shifts the amount of material trapped in between build platform and the membrane. In analogy to the roughness of the print head, these irregularities are translated to the part. This affects open surfaces, i. e. layers on which no further layer is printed immediately, such as the outer top layer and the bottom surfaces of the microchannels. Hence, in order to fabricate high quality microfluidic devices, the state of the resin vat should be monitored closely. Using a petri dish as resin tray as suggested in [28] circumvents this issue and could be considered as addition to the machine used in the scope of this project. Nonetheless, the herein fabricated chips exhibited sufficiently satisfactory transparency since it was possible to identify both vascular cells and organoid cells via optical microscopy as shown in Fig. 2.8.

Another limitation of the DLP process concerns the available materials. As established in this thesis, the selected material is biocompatible and supports the maturation of cell cultures. Hence, the material selection was successful in reaching the aim of this thesis project. In future efforts, the application of other materials could be investigated. As elaborated in Sec. 3.1.3, the in research often used PDMS exhibits high hydrophobicity and molecule absorption. To build on the advantages of DLP for OoCs demonstrated in this thesis, the investigation of further materials that are suitable with the Asiga MAX X27 printer, seems promising. This comprises the integration of alternative commercial resins, but also challenges the development of new biocompatible resins.

To further evaluate DLP as selected fabrication method, the obtained accuracy of the microstructures was investigated. Overall, DLP-printing satisfied the required accuracy of the elements. Especially the dimensions of channel width and pillar width were accurately matched with the 3D-model. The measured length of the pillar exhibited a larger variability. On the one hand, the relatively high standard deviation can be attributed to the analysing tool. The resolution of the images taken with the available microscope made it difficult to precisely define start and end point of the structure. On the other hand, the printer reached its resolution limits. The pillar design had sharp corners and the distance from corner to corner was defined as the reference length. Due to the maximum resolution of 27 µm, this exact shape cannot be realised. This deviation from the intended geometry raises attention to the microfluidic properties of the structure. The capability of pinning a fluid-fluid interface between two pillars was found to decrease drastically with increasing curvature of sharp corners [124]. Though there was no sign of unwanted mixing of gel and media, a future design iteration could investigate this dimensional inaccuracy to guarantee optimal device performance. The standard deviation of the dimension of the pillars was $\pm$20.27 µm. This falls within the resolution limits of the printer and therefore was tolerated as error.

5.2. Biodegradable Membrane for OoC-platform

The method studied in the literature for mixing a wax matrix with conductive particles was successfully translated to the selected materials. The characterisation of the matrix as well as the membrane composite gave insight into properties of the materials. The thermal properties were determined with DSC measurements. Running two heating-cooling cycles was necessary to remove the thermal history of the material. The DSC analysis revealed two endothermic peaks for BBW in the investigated region. As explained, the composition of BBW is highly complex containing a multitude of different chemical components in form of alcohols, fatty acids, and wax esters. The existence of more than one melting peak is likely due to the different melting points of these molecular structures inside the BBW sample.

The same is true for lanolin.

The matrix selected for further experiments was M04 (40:60 vol.-% bayberry wax:lanolin). The melting point was measured at 44.29°C. Since the application demands the melting of the material in contact with the cells, this high value strikes attention. While protein denaturation must be strictly inhibited, a closer analysis of the results reveals that the material features a broad melting range. For this reason, a single temperature does not describe the thermal behaviour in its entirety. The DSC graph of the matrix shows three endothermic peaks in the investigated area. An endothermic peak, expressed in a sudden decrease of the heat flow, indicates a phase change in which the sample absorbs energy. The existence of several peaks results from different matrix components melting at different temperatures. While the sample will only be fully liquified at temperatures above the melting point, the viscosity decreases already at slightly lower temperatures. This matches the experiences from the experiments conducted in the scope of this master thesis. As important note, the peak of the heat capacity was measured at slightly lower temperature at 43.78°C. In theory, the peak value should be located at the melting point. One potential explanation could be that the DSC measurements were conducted with a relatively large heating rate. A slower increase could increase the resolution of the results and yield more exact values for the melting point. A reliable assessment of this parameter is pivotal to avoid the thermal death of cells in the vicinity of the membrane during evacuation.

The influence of the particles in the matrix on the thermal properties was not explicitly studied. In a separate line of experiments, it would be interesting to investigate whether the slight drop of the melting point to 44.11°C can be allocated to the presence of particles. Particularly noticeable is the drop of fusion heat compared to the empty matrix. Less energy was required to melt the sample when including particles. This can possibly be explained with the effect that the particles hardly absorb any heat at the temperature range under investigation. Instead, the absorbed heat flow is directed towards melting the matrix. Since the matrix content is less with particles (same total sample mass), less heat is required to melt the sample. The steady shifting of the DSC curve towards higher temperatures with increasing BBW volume fraction as presented in Fig. 4.6 indicates that the selected materials generally showed a good miscibility. The higher the BBW content, the higher the observed fusion energy. Hence, bayberry wax stores a larger amount of energy in the phase transition. The heat capacity of the composite was investigated with DSC. Since the region of application is around the melting point of the matrix, the value is subjected to slight variations and not defined at the melting point itself. No value for the heat capacity of bayberry wax nor lanolin could be found in literature. However, the estimated value falls into the same order of magnitude as for the phase change material paraffin wax [125]. This gives rise to the assumption that the estimation of the heat capacity was satisfactory.

The results of the magnetisation measurements gave insights into magnetic properties of carbonyl iron powder and magnetite particles. The saturation magnetisation and the hysteresis loop were larger for CIP particles. As explained in Sec. 2.4, a larger hysteresis loop promotes the heating capability upon application of a magnetic field. Additionally, the magnetite particles exhibited a stronger particle agglomeration in the composite mixing process. This aligns well with higher remnant magnetisation of the magnetite particles compared to CIP. This parameter indicates the remaining magnetisation of particles even after removing the external field. Due to the remaining magnetisation, magnetite particles were attracted to each other leading to heterogeneous dispersion. For these reasons, the focus was put on CIP as active agent in the membrane composite providing higher hysteresis loss and enhanced handling in the fabrication process.

The inductive heating experiments proved that the intended mechanism to heat the composite with and AMF is feasible. The large differences in heating efficiency of the different samples made it impossible to set the same exposure parameters for each measurement in the given time. In a more extensive study, the experiment plan could be adapted such that the results are based on uniform conditions. In addition, the set up for the heating experiment was non-adiabatic, i. e., the composite heating worked against the heat loss to the environment. Though the cooling temperature was set to 37°C, it was insufficient to maintain a constant thermal environment. With respect to the intended application, the temperature decrease gives a rather realistic scenario. The OoC-platform containing the cell cultures is stored in an incubator at 37°C. However, for opening the membrane, the chip is placed in an AMF set up at room temperature. Therefore, the as-measured HR and SLP values are directly translatable

to the membrane on the chip.

The resulting SLP values are difficult to compare to other values due to high variability of inductive heating systems employed in different laboratories. However, the trend of linear increase of SLP with increasing particle concentration compares well to a study conducted in [126]. The authors investigated amongst others the SLP of CIP microparticles dispersed in an epoxy resin matrix and observed the same trend. In addition, a dependence on the particle size was observed. In distinction to [126], the particles investigated in this project were not characterised in terms of size. Determination of the particle size distribution would be a fruitful addition to the work presented here to substantiate the results. The relatively large variability of heating rate for the experimental condition IH_{10_10} resulted from particle sedimentation during the experiments. The sample after the measurements is depicted in Fig. 5.1. On the one hand, this confirms that the matrix melted during the first exposure period. On the other hand, the dislocation of the particles from the centre of the coil reduced the heating efficiency adding uncertainty to the results.

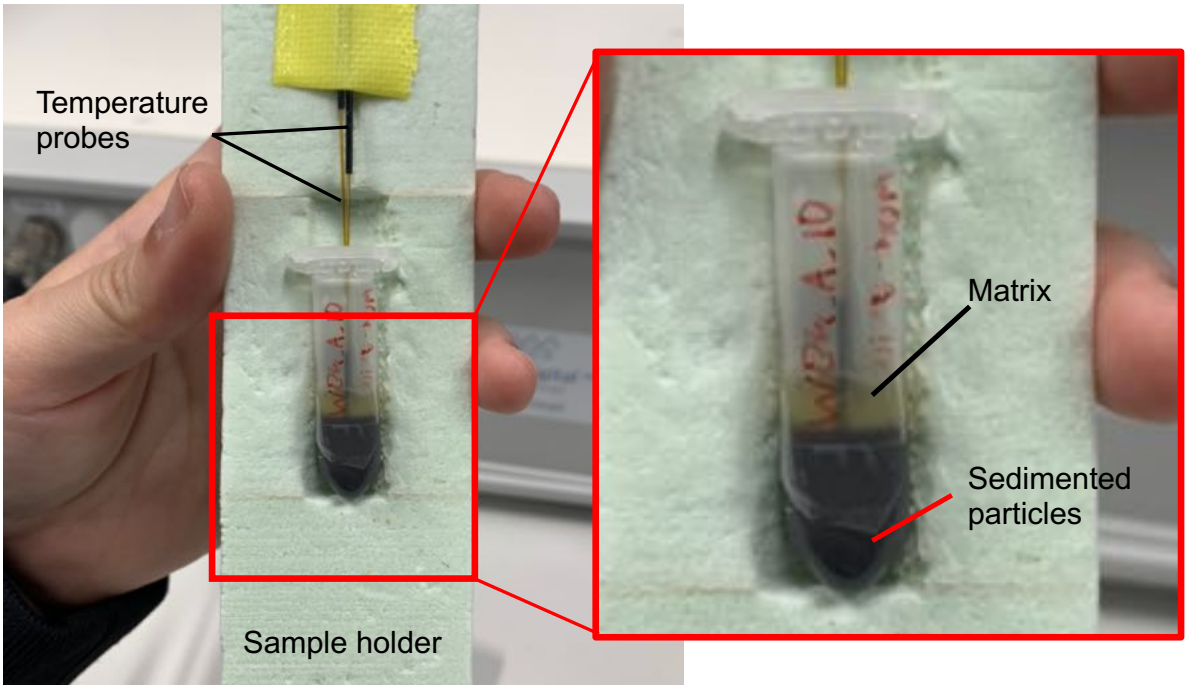

Figure 5.1: Particle sedimentation during inductive heating experiment observed in one sample.

Despite the variability of the SLP values for one field strength, the most favourable particle volume fraction is 10 vol.-%. The analysis of the heating of the particles in the inductive heating experiment justifies this conclusion. The highest heating rate recorded for the 3 vol.-% composite was 2.66 {0.05}°C/min at the highest investigated field strength. The low heating efficiency is unfavourable for melting the membrane since the opening process of the membrane should happen as quick as possible to minimise the burden on the cell cultures. Therefore, this composite is disqualified. The composite with 25 vol.-% particles would be able to generate the required heat in a matter of seconds with an average heating rate HR = 41.73 {0.49}°C/min at the strongest B-field. However, this high rate introduces the risk of overheating the membrane. Deviating from the intended exposure time by 2.5 s would already overshoot the target temperature by 1°C, which could lead to severe damage of the cell cultures. Lower field strength, however, are on the verge of being not efficient enough. Therefore, the sample with 10 vol.-% is preferred as it exhibited a useful middle ground between the two extremes.

Taking the results of the experiments together, the optimal membrane composition was determined as a bayberry wax-lanolin matrix in the ratio 40:60 vol.-% enriched with 10 vol.-% CIP particles. The inclusion of the CEM43 model allows for a proposal of an AMF exposure profile to open the membrane on chip in a contact-free, non-harmful manner:

- In order to open the membrane, the melting point of the composite material must be reached, setting a ΔT as target for the profile:
-

$$\Delta T = T_{\text{m}} - T_{\text{incubator}} = 7^{\circ}\,\text{C} \tag{5.1}$$

- with $T_{\text{incubator}}$ = 37 °and T_{m} = 44 °.
- The CEM43 value for the BBB model [122] allows an exposure time to that temperature for $CEM43 = 1$ min.
- With a heating rate of 14.37 °C/min at B = 10 mT, f = 346.5 kHz,
- the sample is heated to 44 °C in 29 s,
- leaving 31 s to apply pressure to evacuate the matrix.

To avoid immediate solidification of the membrane after removing the AMF exposure, the field strength can be set to B = 2.5 mT. For this composite, that field strength yielded a heating rate of -0.05 °C/min. Considering the baseline temperature drift recorded with the empty matrix, this configuration generates almost just enough heat to keep the sample temperature constant despite the heat flux to the environment. Applying this field to the membrane, therefore stabilises the liquid phase sufficiently long to evacuate the channel and open the membrane for cross communication of vasculature and brain organoid.

Moreover, the results of the inductive heating experiment point out that the particle fraction can be optimised for a broader application to an arbitrary required temperature increase respecting the allowed thermal exposure time as given by the CEM43 model. The herein presented exposure profile is valuable in that aspect that the values have been confirmed experimentally and thereby award a reasonable level of confidence to it. However, it is important to consider that the heating rate and efficiency depend on the experimental and systematic set-up.

The drafted biodegradability study could not be realised in the scope of this master thesis due to the lack of time. The discussed experiment will give further insights into the transient behaviour of the membrane. The sample material as well as the PDMS molds were generated as final effort of this thesis and will be continued. The expected degradation mechanism is hydrolysis. The mass loss and water uptake rate will give valuable information on the membranes capability to separate the different cell media on-chip.

5.3. Integration of Biodegradable Membrane to OoC-platform

The geometry of the pillars confining the membrane channel were optimised with the combined results of the experimental approach and the numerical simulation. The aim was to reach the best material confinement while leaving a maximum gap for the cells to penetrate through the pillars to the organoid chamber. While it is important to remark that the simulation parameters were based on rough calculations, the compliance of the experiments and simulation results support the significance of the outcome. Both approaches indicated that the parameter pairs [rectangular, 30 µm] and [stadium (D25), 30 µm] showed the strongest performance in confining the membrane material in the channel. The comparison of the air gap between two pillars of each geometry leads to a single optimal solution for the pillar array design. To illustrate this, in Fig. 5.2 the top views of the 3D-models of the two configurations are compared. While the minimal distance G is the same for both geometries, the curvature of the stadium geometry leads to a maximum gap width w_o = 80 µm at the interface to the channels leading to a 2.67-times increase of the area for vascular cells to enter the channel compared to the rectangular geometry. Therefore, the [stadium (D25), 30 µm] pillar design is implemented in the design to feature the ”two-culture” configuration of the final version of the herein developed OoC-platform.

Concerning the evacuation of the matrix, a proof-of-concept experiment showed that the application of air flow opens the membrane and that fluids are able to penetrate the membrane channel. The coloured traces of the food dye were detected in the membrane channel not before 24 h after the

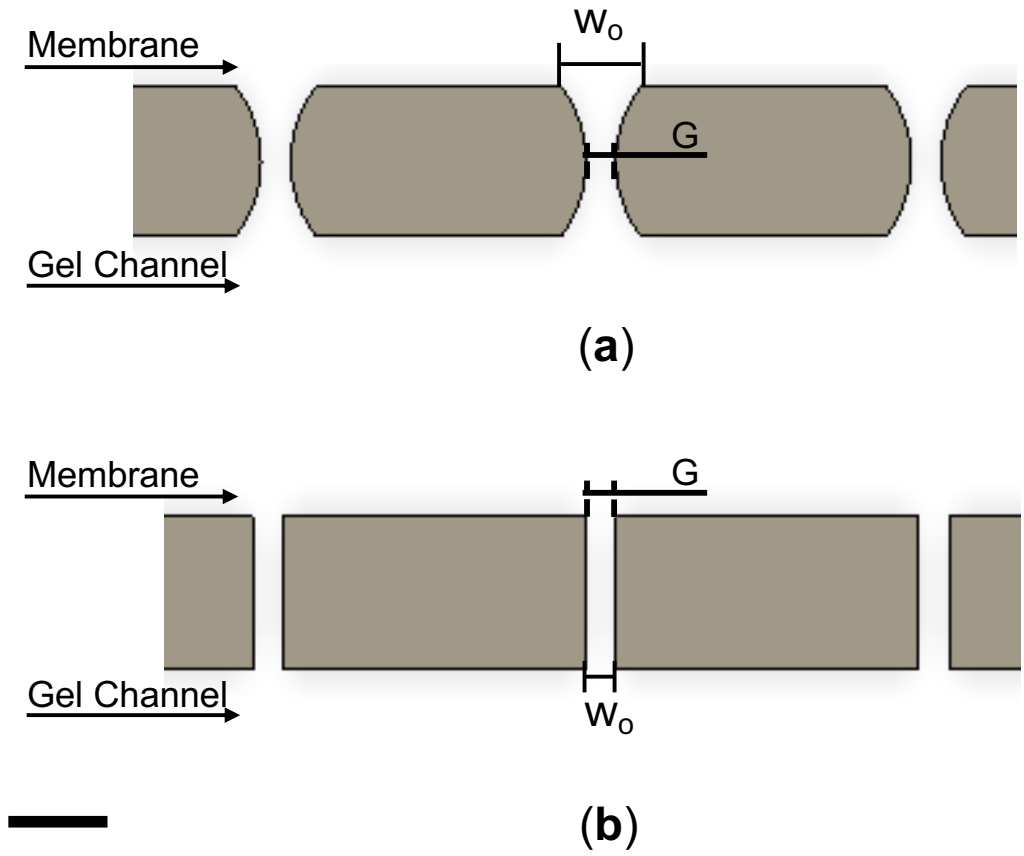

Figure 5.2: Channel-side gap w_o for sprouts to penetrate the membrane channel through confining pillar array. Scale bar is 0.1 mm. (**a**): [stadium (D25), 30 µm] configuration. (**b**): [rectangular, 30 µm].

injection. This could have three reasons. Firstly, the injected fluid volume was too small, and the channel was not refilled. The lack of pressure likely prevented a considerable movement or diffusion of the fluid. Secondly, the membrane was only partially opened which impeded a swift distribution of the coloured water and only after some time the free pillar gaps were ”found”. There is no evidence to support neither to refute this claim. A repetition of the experiment under same conditions could evaluate this scenario. Thirdly, due to the intense black of the membrane material the dye became visible only after a sufficient amount agglomerated in one place to overcome the contrast. The three hypotheses can be checked by repeating the experiment. The volume of injected fluid can be increased as well as the pressure value to increase the probability of clearly displacing the material from the channel.

The black residual material in the channel, however, raises a new research direction for the follow-up work of this master project. Assuming the membrane is in fact open but the ink cannot be detected due to the black colour of the material, foreshadows complications with the imaging of cells growing across that channel. Whereas in case of successful penetration the sprouts could be captured entering and leaving the membrane channel, the state inside the membrane channel would remain hidden. One opportunity to tackle this could be the replacement of the gas used to flush the channel with a fluid. With sufficient pressure, the fluid could dislocate the remaining membrane material and subsequently fill the created void. This has potential since the fluid could contain growth factors for the vascular cells increasing the probability of cells migrating towards the brain organoid. The second suggestion for a new research direction is the employment of a transparent membrane material. Injecting a transparent membrane instead of black particles is an elegant way to prevent membrane induced issues with the imaging. One path of research leads to the use of pluronics. In [127], this hydrogel is used as fugitive ink to engineer 3D vascular structures through bioprinting. This proves the biocompatibility of the material. Pluronics conduct reversible gelation at low temperatures (down to 4 °C). While highly viscous or solid

at physiological temperature, it becomes liquid when cooled below the gelation point. This mechanism could be exploited for membrane evacuation. Whether the hydrogel is capable of successfully repelling the cell cultures as well as the brain organoid's compatibility with these low temperatures remain key questions to be answered in future research.

6

Conclusion

This master project aimed to develop the groundwork for a novel multi-cell Organ-on-Chip platform for the vascularisation of organoids. This was successfully achieved with the efforts undertaken presented in this report. Starting with the establishment of an original OoC design, digital light processing was selected as the most favourable fabrication method. 3D-printing the chip benefited the design freedom and was applied to reliably generate chips in a time- and cost-effective manner. The design constraints and requirements were independently clustered from two proven cell protocols for the formation of a Vessel-on-Chip and brain organoid, respectively.

The biocompatibility of the design and the material was confirmed by the survival of neuronal cells and the formation of a vascular network in initial seeding tests. In order to enable the co-culturing of the inherently different cell types while maintaining the distinct microfluidic features for both cultures, a biodegradable membrane was integrated into the chip. The membrane was designed from a wax matrix enriched with magnetic carbonyl iron particles. The matrix composition was tuned to feature a melting point around 43°C, by mixing lanolin and bayberry wax in a distinct ratio. The addition of CIP particles functionalised the matrix such that the membrane can be heated upon the application of an alternating magnetic field. This contact-free activation method facilitates the melting of the composite material on chip. As liquid phase, the membrane can be flushed from the membrane channel, opening the space for the vessels to penetrate the organoid.

Based on inductive heating experiments with the composite material, an AMF exposure profile was suggested that locally melts the membrane and maintains the temperature until the material is evacuated from the barrier. The integration of the membrane as composite on chip was demonstrated to be successful on test structures. This included the injection and the evacuation of the material with the introduction of pressure.

In conclusion, the work of this master project initiated the collaboration of three research groups working towards the vascularisation of brain organoids. The achieved results pave the way towards the co-culturing of well-established cell protocols. The fabrication of a biocompatible microfluidic device was accomplished enforcing the applicability of additive manufacturing techniques for OoC-technology. The biodegradable composite with a melting point in the physiological relevant range that can be activated wirelessly in a non-harmful manner, is suitable as membrane in the target application and for a multitude of further applications. Together, the achieved results add tools for biomedical research exceeding the scope of this project.

References

[1] Chak Ming Leung et al. “A guide to the organ-on-a-chip”. In: *Nature Reviews Methods Primers* 2.1 (2022), p. 33.

[2] Magali P. Ferro, Sarah C. Heilshorn, and Roisin M. Owens. “Materials for blood brain barrier modeling in vitro”. In: *Materials Science and Engineering R: Reports* 140 (Apr. 2020). good quote for introduction of ooc. ISSN: 0927796X. DOI: 10.1016/J.MSER.2019.100522.

[3] Chao Ma et al. “Organ-on-a-Chip: A new paradigm for drug development Microfluidic Organ-on-a-Chip: A paradigm shift in drug development HHS Public Access”. In: *Trends Pharmacol Sci* 42 (2 2021), pp. 119–133. DOI: 10.1016/j.tips.2020.11.009.

[4] Benedetta Artegiani and Hans Clevers. “Use and application of 3D-organoid technology”. In: *Human Molecular Genetics* 27 (2018). DOI: 10.1093/hmg/ddy187.

[5] Erin LaMontagne, Alysson R Muotri, and Adam J Engler. “Recent advancements and future requirements in vascularization of cortical organoids”. In: *Frontiers in Bioengineering and Biotechnology* (2022), p. 2059.

[6] Chak Ming Leung et al. “A guide to the organ-on-a-chip”. In: *Nature Reviews Methods Primers* 2 (1 Dec. 2022). ISSN: 26628449. DOI: 10.1038/s43586-022-00118-6.

[7] Jiu Deng et al. “Engineered Liver-On-A-Chip Platform to Mimic Liver Functions and Its Biomedical Applications: A Review”. In: *Micromachines (Basel)* 10 (10 2019). DOI: 10.3390/mi10100676.

[8] Pauline Zamprogno et al. “Second-generation lung-on-a-chip with an array of stretchable alveoli made with a biological membrane”. In: *Communications Biology* 4 (2021). DOI: 10.1038/s42003-021-01695-0.

[9] Anna Marsano et al. “Beating heart on a chip: a novel microfluidic platform to generate functional 3D cardiac microtissues.” In: *Lab on a chip* 16 3 (2016), pp. 599–610.

[10] Qirui Wu et al. “Organ-on-a-chip: Recent breakthroughs and future prospects”. In: *BioMedical Engineering Online* 19 (1 Feb. 2020). ISSN: 1475925X. DOI: 10.1186/s12938-020-0752-0.

[11] Inês Miranda et al. “Properties and applications of PDMS for biomedical engineering: A review”. In: *Journal of functional biomaterials* 13.1 (2021), p. 2.

[12] Scott B Campbell et al. “Beyond polydimethylsiloxane: alternative materials for fabrication of organ-on-a-chip devices and microphysiological systems”. In: *ACS biomaterials science & engineering* 7.7 (2020), pp. 2880–2899.

[13] Bishal Kumar Nahak et al. “Advances in organ-on-a-chip materials and devices”. In: *ACS applied bio materials* 5.8 (2022), pp. 3576–3607.

[14] Michael W Toepke and David J Beebe. “PDMS absorption of small molecules and consequences in microfluidic applications”. In: *Lab on a Chip* 6.12 (2006), pp. 1484–1486.

[15] Uyen MN Cao et al. “Microfluidic organ-on-A-chip: A guide to biomaterial choice and fabrication”. In: *International Journal of Molecular Sciences* 24.4 (2023), p. 3232.

[16] Xingyuan Yang et al. “Nanofiber membrane supported lung-on-a-chip microdevice for anti-cancer drug testing”. In: *Lab on a Chip* 18.3 (2018), pp. 486–495.

[17] Richard T Tran et al. “Synthesis and characterization of a biodegradable elastomer featuring a dual crosslinking mechanism”. In: *Soft matter* 6.11 (2010), pp. 2449–2461.

[18] Adel A Abdel-Wahab, Sabbah Ataya, and Vadim V Silberschmidt. “Temperature-dependent mechanical behaviour of PMMA: Experimental analysis and modelling”. In: *Polymer Testing* 58 (2017), pp. 86–95.

[19] Alwin MD Wan, Deepika Devadas, and Edmond WK Young. “Recycled polymethylmethacrylate (PMMA) microfluidic devices”. In: *Sensors and Actuators B: Chemical* 253 (2017), pp. 738–744.

[20] Xiaopeng Wen et al. “In vitro nonalcoholic fatty liver disease model with cyclo-olefin-polymer-based microphysiological systems”. In: *Organs-on-a-Chip* 3 (2021), p. 100010.

[21] Chi-Shuo Chen et al. “Shrinky-Dink microfluidics: 3D polystyrene chips”. In: *Lab on a Chip* 8.4 (2008), pp. 622–624.

[22] Yi Wang et al. “In-channel modification of biosensor electrodes integrated on a polycarbonate microfluidic chip for micro flow-injection amperometric determination of glucose”. In: *Sensors and Actuators B: Chemical* 145.1 (2010), pp. 553–560.

[23] Andres W Martinez et al. “Patterned paper as a platform for inexpensive, low-volume, portable bioassays”. In: *Angewandte Chemie* 119.8 (2007), pp. 1340–1342.

[24] Ciprian Iliescu et al. “A practical guide for the fabrication of microfluidic devices using glass and silicon”. In: *Biomicrofluidics* 6.1 (2012).

[25] Hirotada Hirama et al. “Glass-based organ-on-a-chip device for restricting small molecular absorption”. In: *Journal of bioscience and bioengineering* 127.5 (2019), pp. 641–646.

[26] Bart Kramer et al. “Interstitial flow recapitulates gemcitabine chemoresistance in a 3D microfluidic pancreatic ductal adenocarcinoma model by induction of multidrug resistance proteins”. In: *International Journal of Molecular Sciences* 20.18 (2019), p. 4647.

[27] Ronaldo Martins da Ponte et al. “Monolithic integration of a smart temperature sensor on a modular silicon-based organ-on-a-chip device”. In: *Sensors and Actuators A: Physical* 317 (2021), p. 112439.

[28] Anna Fritschen et al. “Investigation and comparison of resin materials in transparent DLP-printing for application in cell culture and organs-on-a-chip”. In: *Biomaterials science* 10.8 (2022), pp. 1981–1994.

[29] Shirin Mesbah Oskui et al. “Assessing and reducing the toxicity of 3D-printed parts”. In: *Environmental Science & Technology Letters* 3.1 (2016), pp. 1–6.

[30] Sidra Waheed et al. “3D printed microfluidic devices: enablers and barriers”. In: *Lab on a Chip* 16.11 (2016), pp. 1993–2013.

[31] Dong Qin, Younan Xia, and George M Whitesides. “Soft lithography for micro-and nanoscale patterning”. In: *Nature protocols* 5.3 (2010), p. 491.

[32] Alireza Tajeddin and Nur Mustafaoglu. “Design and fabrication of organ-on-chips: Promises and challenges”. In: *Micromachines* 12.12 (2021), p. 1443.

[33] Younan Xia et al. “Replica molding using polymeric materials: A practical step toward nanomanufacturing”. In: *Advanced Materials* 9.2 (1997), pp. 147–149.

[34] Onur Kilic et al. “Brain-on-a-chip model enables analysis of human neuronal differentiation and chemotaxis”. In: *Lab on a Chip* 16.21 (2016), pp. 4152–4162.

[35] Aerim Choe et al. “Microfluidic Gut-liver chip for reproducing the first pass metabolism”. In: *Biomedical microdevices* 19 (2017), pp. 1–11.

[36] Jesus Shrestha et al. “A rapidly prototyped lung-on-a-chip model using 3D-printed molds”. In: *Organs-on-a-Chip* 1 (2019), p. 100001.

[37] Joseph R Puryear III, Jeong-Kee Yoon, and YongTae Kim. “Advanced fabrication techniques of microengineered physiological systems”. In: *Micromachines* 11.8 (2020), p. 730.

[38] Makoto Yamanaka et al. “Cyclo olefin polymer-based solvent-free mass-productive microphysiological systems”. In: *Biomedical Materials* 16.3 (2021), p. 035009.

[39] Kimberly A Homan et al. “Bioprinting of 3D convoluted renal proximal tubules on perfusable chips”. In: *Scientific reports* 6.1 (2016), p. 34845.

[40] Chee Meng Benjamin Ho et al. “3D printed microfluidics for biological applications”. In: *Lab on a Chip* 15.18 (2015), pp. 3627–3637.

[41] Madhusudan Singh et al. “Inkjet printing—process and its applications”. In: *Advanced materials* 22.6 (2010), pp. 673–685.

[42] Zahra Faraji Rad, Philip D Prewett, and Graham J Davies. “High-resolution two-photon polymerization: The most versatile technique for the fabrication of microneedle arrays”. In: *Microsystems & nanoengineering* 7.1 (2021), p. 71.

[43] K Satish Prakash, T Nancharaih, and VV Subba Rao. “Additive manufacturing techniques in manufacturing-an overview”. In: *Materials Today: Proceedings* 5.2 (2018), pp. 3873–3882.

[44] Gregory W Bishop et al. “3D-printed fluidic devices for nanoparticle preparation and flow-injection amperometry using integrated prussian blue nanoparticle-modified electrodes”. In: *Analytical chemistry* 87.10 (2015), pp. 5437–5443.

[45] Anthony K Au et al. “3D-printed microfluidics”. In: *Angewandte Chemie International Edition* 55.12 (2016), pp. 3862–3881.

[46] Jiumeng Zhang et al. “Digital light processing based three-dimensional printing for medical applications”. In: *International journal of bioprinting* 6.1 (2020).

[47] Andrea Luongo et al. “Microstructure control in 3D printing with digital light processing”. In: *Computer Graphics Forum*. Vol. 39. 1. Wiley Online Library. 2020, pp. 347–359.

[48] Kubra Sekmen et al. “Thermal analysis and shrinkage characterization of the photopolymers for DLP additive manufacturing processes”. In: *Continuum Mechanics and Thermodynamics* (2022), pp. 1–18.

[49] Arturo Urrios et al. “3D-printing of transparent bio-microfluidic devices in PEG-DA”. In: *Lab on a Chip* 16.12 (2016), pp. 2287–2294.

[50] Samuel Clark Ligon et al. “Strategies to reduce oxygen inhibition in photoinduced polymerization”. In: *Chemical reviews* 114.1 (2014), pp. 557–589.

[51] Hee-Gyeong Yi, Hyungseok Lee, and Dong-Woo Cho. “3D printing of organs-on-chips”. In: *Bioengineering* 4.1 (2017), p. 10.

[52] Louis Jun Ye Ong et al. “A 3D printed microfluidic perfusion device for multicellular spheroid cultures”. In: *Biofabrication* 9.4 (2017), p. 045005.

[53] Heather A McCauley and James M Wells. “Pluripotent stem cell-derived organoids: using principles of developmental biology to grow human tissues in a dish”. In: *Development* 144.6 (2017), pp. 958–962.

[54] Yohei Isshiki et al. “Co-Culture of a Brain Organoid Derived from Human iPSCs and Vasculature on a Chip; Co-Culture of a Brain Organoid Derived from Human iPSCs and Vasculature on a Chip”. In: (2020).

[55] Hao Nguyen Tran and Vini Gautam. “Micro/nano devices for integration with human brain organoids”. In: *Biosensors and Bioelectronics* 218 (Dec. 2022). ISSN: 18734235. DOI: 10.1016/j.bios.2022.114750.

[56] Nandan Shettigar et al. “Design, microfabrication and testing of brain-on-A-chip (boc) platform using neural organoids (spheroids)”. In: *American Society of Mechanical Engineers, Fluids Engineering Division (Publication) FEDSM* 3 (2021). ISSN: 08888116. DOI: 10.1115/FEDSM2021-65894.

[57] Jiyoung Song et al. “Brain organoid-on-a-chip: A next-generation human brain avatar for recapitulating human brain physiology and pathology”. In: *Biomicrofluidics* 16 (6 Dec. 2022). ISSN: 19321058. DOI: 10.1063/5.0121476.

[58] Idris Salmon et al. “Engineering neurovascular organoids with 3D printed microfluidic chips”. In: *Lab on a Chip* 22 (8 Mar. 2022). cerebral = brain organoids, pp. 1615–1629. ISSN: 14730189. DOI: 10.1039/D1LC00535A.

[59] Minghui Li et al. “Toward the next generation of vascularized human neural organoids”. In: *Medicinal Research Reviews* 43.1 (2023), pp. 31–54.

[60] Peter Carmeliet. “Angiogenesis in life, disease and medicine”. In: *Nature* 438.7070 (2005), pp. 932–936.

[61] Chang-Yang Xing et al. “Distribution of cardiac output to the brain across the adult lifespan”. In: *Journal of Cerebral Blood Flow & Metabolism* 37.8 (2017), pp. 2848–2856.

[62] Philipp Wörsdörfer et al. “Generation of complex human organoid models including vascular networks by incorporation of mesodermal progenitor cells”. In: *Scientific reports* 9.1 (2019), p. 15663.

[63] Yingchao Shi et al. “Vascularized human cortical organoids (vOrganoids) model cortical development in vivo”. In: *PLoS biology* 18.5 (2020), e3000705.

[64] Abed AlFatah Mansour et al. “An in vivo model of functional and vascularized human brain organoids”. In: *Nature biotechnology* 36.5 (2018), pp. 432–441.

[65] Bruce Alberts et al. “Blood vessels and endothelial cells”. In: *Molecular Biology of the Cell. 4th edition*. Garland Science, 2002.

[66] Joseph W Wragg et al. “Shear stress regulated gene expression and angiogenesis in vascular endothelium”. In: *Microcirculation* 21.4 (2014), pp. 290–300.

[67] Joji Ando and Kimiko Yamamoto. “Hemodynamic forces, endothelial mechanotransduction, and vascular diseases”. In: *Magnetic Resonance in Medical Sciences* 21.2 (2022), pp. 258–266.

[68] Jungwook Paek et al. “Microphysiological engineering of self-assembled and perfusable microvascular beds for the production of vascularized three-dimensional human microtissues”. In: *ACS nano* 13.7 (2019), pp. 7627–7643.

[69] Sreenivasulu Gunti et al. “Organoid and spheroid tumor models: Techniques and applications”. In: *Cancers* 13.4 (2021), p. 874.

[70] Angela Di Baldassarre et al. “Human-induced pluripotent stem cell technology and cardiomyocyte generation: progress and clinical applications”. In: *Cells* 7.6 (2018), p. 48.

[71] Lei Ye, Cory Swingen, and Jianyi Zhang. “Induced pluripotent stem cells and their potential for basic and clinical sciences”. In: *Current cardiology reviews* 9.1 (2013), pp. 63–72.

[72] Marc Vila Cuenca et al. “Engineered 3D vessel-on-chip using hiPSC-derived endothelial-and vascular smooth muscle cells”. In: *Stem Cell Reports* 16.9 (2021), pp. 2159–2168.

[73] Rekha Samuel et al. “Vascular diseases await translation of blood vessels engineered from stem cells”. In: *Science translational medicine* 7.309 (2015), 309rv6–309rv6.

[74] Nilhan Gunhanlar et al. “A simplified protocol for differentiation of electrophysiologically mature neuronal networks from human induced pluripotent stem cells”. In: *Molecular psychiatry* 23.5 (2018), pp. 1336–1344.

[75] PE Resmi et al. “Paper based micro/nanofluidics devices for biomedical applications”. In: *Progress in Molecular Biology and Translational Science* 186.1 (2022), pp. 159–190.

[76] Atul Sharma et al. “Review on thermal energy storage with phase change materials and applications”. In: *Renewable and Sustainable energy reviews* 13.2 (2009), pp. 318–345.

[77] John A. Noël et al. “Chapter 13 - Phase Change Materials”. In: *Storing Energy*. Ed. by Trevor M. Letcher. Oxford: Elsevier, 2016, pp. 249–272. ISBN: 978-0-12-803440-8. DOI: https://doi.org/10.1016/B978-0-12-803440-8.00013-0.

[78] Navin Kumar and Debjyoti Banerjee. “Phase Change Materials”. In: *Handbook of Thermal Science and Engineering*. Cham: Springer International Publishing, 2018, pp. 2213–2275. ISBN: 978-3-319-26695-4. DOI: 10.1007/978-3-319-26695-4_53.

[79] K. S. Kim et al. “Isotropic conductive paste for bioresorbable electronics”. In: *Materials Today Bio* 18 (2023).

[80] Z. H. Wei et al. “Accelerable Self-Sintering of Solvent-Free Molybdenum/Wax Biodegradable Composites for Multimodally Transient Electronics”. In: *Acs Applied Materials & Interfaces* 14.29 (2022), pp. 33472–33481. ISSN: 1944-8244. DOI: 10.1021/acsami.2c04647.

[81] Sang Min Won et al. “Natural wax for transient electronics”. In: *Advanced Functional Materials* 28.32 (2018), p. 1801819.

[82] K. S. Kim et al. “Biodegradable Molybdenum/Polybutylene Adipate Terephthalate Conductive Paste for Flexible and Stretchable Transient Electronics”. In: *Advanced Materials Technologies* 7.2 (2022). ISSN: 2365-709X. DOI: 10.1002/admt.202001297.

[83] P. Cataldi et al. “An Electrically Conductive Oleogel Paste for Edible Electronics”. In: *Advanced Functional Materials* 32.23 (2022). DOI: 10.1002/adfm.202113417.

[84] P. R. de Oliveira et al. “Use of beeswax as an alternative binder in the development of composite electrodes: an approach for determination of hydrogen peroxide in honey samples”. In: *Electrochimica Acta* 390 (2021). ISSN: 0013-4686. DOI: 10.1016/j.electacta.2021.138876.

[85] Seungae Lee et al. “Metal microparticle–Polymer composites as printable, bio/ecoresorbable conductive inks”. In: *Materials Today* 21.3 (2018), pp. 207–215.

[86] Hira Fatima, Tawatchai Charinpanitkul, and Kyo-Seon Kim. “Fundamentals to Apply Magnetic Nanoparticles for Hyperthermia Therapy”. In: *Nanomaterials* 11.5 (2021). ISSN: 2079-4991. DOI: 10.3390/nano11051203.

[87] Eirini Myrovali et al. “Toward the Separation of Different Heating Mechanisms in Magnetic Particle Hyperthermia”. In: *ACS omega* 8.14 (2023), pp. 12955–12967.

[88] Punit Kaur et al. “Hyperthermia using nanoparticles–promises and pitfalls”. In: *International Journal of Hyperthermia* 32.1 (2016), pp. 76–88.

[89] Elizabeth Adjoa Kumah et al. “Human and environmental impacts of nanoparticles: a scoping review of the current literature”. In: *BMC Public Health* 23.1 (2023), pp. 1–28.

[90] Andreas Jordan et al. “Inductive heating of ferrimagnetic particles and magnetic fluids: physical evaluation of their potential for hyperthermia”. In: *International journal of hyperthermia* 25.7 (2009), pp. 499–511.

[91] Silvio Dutz and Rudolf Hergt. “Magnetic nanoparticle heating and heat transfer on a microscale: Basic principles, realities and physical limitations of hyperthermia for tumour therapy”. In: *International Journal of Hyperthermia* 29.8 (2013), pp. 790–800.

[92] Marcel Suter. “Photopatternable superparamagnetic nanocomposite for the fabrication of microstructures”. PhD thesis. ETH Zurich, 2012.

[93] Mayukh Nath et al. “Understanding the role of magnetic and magneto-quasistatic fields in human body communication”. In: *IEEE Transactions on Biomedical Engineering* 69.12 (2022), pp. 3635–3644.

[94] Tae Hyeon Kim et al. “Development of the microfluidic device to regulate shear stress gradients”. In: *BioChip Journal* 12 (2018), pp. 294–303.

[95] Federico Bella and Roberta Bongiovanni. “Photoinduced polymerization: an innovative, powerful and environmentally friendly technique for the preparation of polymer electrolytes for dye-sensitized solar cells”. In: *Journal of photochemistry and photobiology C: photochemistry reviews* 16 (2013), pp. 1–21.

[96] Louis Ong and Yi-Chin Toh. “A case study of MOIIN resins: 3D printed microfluidic devices for cell-based applications”. In: (). URL: https://www.moiin-resins.com/wp-content/uploads/2023/04/A-case-study-of-MOIIN-resins-for-cell-culture-device-fabrication-final.pdf.

[97] Gerard C van Rhoon. “Is CEM43 still a relevant thermal dose parameter for hyperthermia treatment monitoring?” In: *International Journal of Hyperthermia* 32.1 (2016), pp. 50–62.

[98] Jeffrey P Simpson, Nicholas Thrower, and John B Ohlrogge. “How did nature engineer the highest surface lipid accumulation among plants? Exceptional expression of acyl-lipid-associated genes for the assembly of extracellular triacylglycerol by Bayberry (Myrica pensylvanica) fruits”. In: *Biochimica et Biophysica Acta (BBA)-Molecular and Cell Biology of Lipids* 1861.9 (2016), pp. 1243–1252.

[99] Jeffrey P Simpson and John B Ohlrogge. “A novel pathway for triacylglycerol biosynthesis is responsible for the accumulation of massive quantities of glycerolipids in the surface wax of bayberry (Myrica pensylvanica) fruit”. In: *The Plant Cell* 28.1 (2016), pp. 248–264.

[100] Jacques Fantini and Nouara Yahi. “Chapter 1-Chemical Basis of Lipid Biochemistry”. In: *Brain Lipids in Synaptic Function and Neurological Disease; Fantini, J., Yahi, N., Eds* (2015), pp. 1–28.

[101] WF Tinto, TO Elufioye, and J Roach. “Waxes”. In: *Pharmacognosy*. Elsevier, 2017, pp. 443–455.

[102] William Charles Evans and Daphne Evans. “Chapter 19 - Hydrocarbons and derivatives”. In: *Trease and Evans’ Pharmacognosy (Sixteenth Edition)*. Ed. by William Charles Evans and Daphne Evans. Sixteenth Edition. W.B. Saunders, 2009, pp. 173–193. ISBN: 978-0-7020-2933-2.

[103] Amit Sengupta and Jagadananda Behera. “Comprehensive view on chemistry, manufacturing & applications of lanolin extracted from wool pretreatment”. In: *Am. J. Eng. Res* 3.7 (2014), pp. 33–43.

[104] Mitchell L Schlossman and Justin P Mccarthy. “Lanolin and its derivatives”. In: *Journal of the American Oil Chemists’ Society* 55.4 (1978), pp. 447–450.

[105] S Gutiérrez and M Viñas. “Anaerobic degradation kinetics of a cholesteryl ester”. In: *Water Science and Technology* 48.6 (2003), pp. 141–147.

[106] Yvonne Tze Qzian Ling et al. “Physiochemical and In-Vitro Cytotoxicity Properties of Biocompatible Palm Fatty Acid-Based Polyesters”. In: *Sains Malays* 50 (2021), pp. 395–407.

[107] Jong Whan Rhim and Thomas H Shellhammer. “Lipid-based edible films and coatings”. In: *Innovations in food packaging*. Elsevier, 2005, pp. 362–383.

[108] Jasvinder Singh et al. “Biological and mechanical characterization of biodegradable carbonyl iron powder/polycaprolactone composite material fabricated using three-dimensional printing for cardiovascular stent application”. In: *Proceedings of the Institution of Mechanical Engineers, Part H: Journal of Engineering in Medicine* 234.9 (2020), pp. 975–987.

[109] Gabriela Gąsior, Jonasz Szczepański, and Aleksandra Radtke. “Biodegradable iron-based materials—what was done and what more can be done?” In: *Materials* 14.12 (2021), p. 3381.

[110] JL Arias et al. “Preparation and characterization of carbonyl iron/poly (butylcyanoacrylate) core/shell nanoparticles”. In: *Journal of colloid and interface science* 299.2 (2006), pp. 599–607.

[111] Tomas Plachy et al. “Impact of corrosion process of carbonyl iron particles on magnetorheological behavior of their suspensions”. In: *Journal of Industrial and Engineering Chemistry* 66 (2018), pp. 362–369.

[112] Eleonora Scarcello et al. “Endothelial dysfunction induced by hydroxyl radicals–the hidden face of biodegradable Fe-based materials for coronary stents”. In: *Materials Science and Engineering: C* 112 (2020), p. 110938.

[113] John Clarke. “Principles and applications of SQUIDs”. In: *Proceedings of the IEEE* 77.8 (1989), pp. 1208–1223.

[114] M Buchner et al. “Tutorial: Basic principles, limits of detection, and pitfalls of highly sensitive SQUID magnetometry for nanomagnetism and spintronics”. In: *Journal of Applied Physics* 124.16 (2018).

[115] RL Fagaly. “Superconducting quantum interference device instruments and applications”. In: *Review of scientific instruments* 77.10 (2006).

[116] John Bardeen, Leon N Cooper, and John Robert Schrieffer. “Theory of superconductivity”. In: *Physical review* 108.5 (1957), p. 1175.

[117] P Seidel. “High-Tc Josephson junctions”. In: *High-Temperature Superconductors*. Elsevier, 2011, pp. 317–369.

[118] J Schawe et al. *Interpreting DSC curves Part 1: Dynamic measurements*. 2000.

[119] Paul Davidovits. “Chapter 9 - Heat and Kinetic Theory”. In: *Physics in Biology and Medicine (Fourth Edition)*. Ed. by Paul Davidovits. Fourth Edition. Complementary Science. Boston: Academic Press, 2013, pp. 109–125. ISBN: 978-0-12-386513-7.

[120] Costica Caizer. “Optimization study on specific loss power in superparamagnetic hyperthermia with magnetite nanoparticles for high efficiency in alternative cancer therapy”. In: *Nanomaterials* 11.1 (2020), p. 40.

[121] Henrik Bruus. *Theoretical microfluidics*. Vol. 18. Oxford university press, 2007.

[122] Manuel Murbach et al. “Thermal tissue damage model analyzed for different whole-body SAR and scan durations for standard MR body coils”. In: *Magnetic resonance in medicine* 71.1 (2014), pp. 421–431.

[123] Nuria Martín Ortega et al. “Comparison of surface roughness of additively manufactured implant-supported interim crowns fabricated with different print orientations”. In: *Journal of Prosthodontics* (2023).

[124] J Berthier et al. “On the pinning of interfaces on micropillar edges”. In: *Journal of colloid and interface science* 338.1 (2009), pp. 296–303.

[125] Abdelwaheb Trigui et al. “Development and characterization of composite phase change material: thermal conductivity and latent heat thermal energy storage”. In: *Composites Part B: Engineering* 49 (2013), pp. 22–35.

[126] Roman V Krekhno, Alexander P Safronov, and Igor V Beketov. “Effect of particle diameter and packing density on heating of metallic iron particles in alternating magnetic field”. In: *Journal of Physics: Conference Series*. Vol. 1389. 1. IOP Publishing. 2019.

[127] David B Kolesky et al. “3D bioprinting of vascularized, heterogeneous cell-laden tissue constructs”. In: *Advanced materials* 26.19 (2014), pp. 3124–3130.